

EFFECT OF DISORDER IN CUPRATES AND MANGANITES

By

SUNG HEE YUN

A DISSERTATION PRESENTED TO THE GRADUATE SCHOOL
OF THE UNIVERSITY OF FLORIDA IN PARTIAL FULFILLMENT
OF THE REQUIREMENTS FOR THE DEGREE OF
DOCTOR OF PHILOSOPHY

UNIVERSITY OF FLORIDA

2008

© 2008 Sung Hee Yun

To my Old Family and the Coming one and her fathers in earth and heaven

ACKNOWLEDGMENTS

There are countless people who throughout my life have given me support and encouragement and who in some way have played a role in helping me write this dissertation. Due to length and time limitations however I will only be able to list a few of them below.

First and foremost, I would like to thank my parents who supported my pursuit to become a physicist, not just because I am a talented person, but because I enjoy the subject and they trusted my decision and have stood by me with strength until today. I am sure that I will come to appreciate more and more their love and wisdom in my life.

I always feel I am extremely lucky to meet the people who have been a part of my life. When I started my PhD work here I didn't know anyone in Gainesville. However, right now, my cell phone address book is full of incredibly important people in my personal history.

I was fortunate to meet some of the best faculty members at this University. Since I started my first semester at this school, I truly felt that it was a great pleasure to study physics with them. Most of all, I would like to thank my advisor Amlan Biswas who guided me and provided resources for my research and was always willing to discuss any problem with knowledge, enthusiasm and especially with extreme patience. Without him I could not have completed my research and dissertation. He also cared for his students not only academically but also with a humanitarian concern. Through good times and hard times with him, I believe I could grow as a more independent and optimistic physicist.

I would like to give special thanks to the members of my dissertation committee Professor Stephen Hill, Professor Peter Hirschfeld, Professor David Norton and Professor David Tanner. They have always been gracious with their time, always finding room for me in their busy schedules. Through their challenging questions they have encouraged me to think more deeply about my project and through their suggestions they have given me valuable guidance.

Several collaborating scientists have contributed to this work invaluablely. Tara Dhakal, who is more like my elder brother now, as a senior lab member, helped me to learn the ins and outs of the lab and always made time to give me any guidance I needed. I wish him good luck on his new work and many more. The former undergraduate student in our group, Jacob Tosado (even though he was tough for me to get along with sometimes), he helped with important parts of the experimental setup for the strain measurement and eagerly tried to improve my communication skills. My good buddy Rajiv Misra carried out procedures to apply disorder, using SHIVA and gave valuable assistance during several attempts at etching and other things. The passionate physicist, Tongay Sefaatin, carried out the capacitance measurement experiment on the multi-layer manganite structure. Ritesh Das helped me carry out squid measurements. Guneeta Singh collaborated with me conducting positive magnetoresistance measurements. These four students are studying under the guidance of Professor Art Hebard. The experiments concerning the clarification of the low temperature upturn in manganites were performed by the warm hearted Pradeep Bhupathi at ultra low temperatures under the guidance of Professor Yoonseok Lee.

Many of the experiments on cuprates were conducted at the National High Magnetic Field Lab (NHMFL) in Tallahassee. I would therefore like to thank the NHMFL for allowing me to use their facility, especially the scientists in the DC field control room who diligently stayed up late into the night to operate the power consuming resistive magnet for us.

This list of acknowledgements would not be complete if I didn't thank the members of the physics department machine shop and electronics shop. Without their craftsmanship, hard work and technical assistance much of the equipment used to carry out this project would not exist. I always thought whatever kind of job I do, if I can do as good as them, I will be happy.

The members of cryogenic services facility should be thanked for keeping the helium cold at all times.

I deeply want to thank Dr. DeSerio and Mr. Parks to their consideration and help for my teaching. Their encouragement really helped me out of those “could be” stressful times. Also, their passion for physics and teaching gave me a moment to think about enjoying physics with students.

I want to thank Jay Horton. He is as handsome as George Clooney and he has a really great heart to help people with his workmanship. I also want to thank Dr. Ivan Kravchenko for teaching me and allowing me to use the Nanofab facility for my experiment. I would like to say thanks to Sandra, I enjoyed her singing while she worked and the rest of the janitorial staff who through their diligent efforts keep our environment clean. I would like to thank FPF for showing me that not only men can be successful in physics and caring for me as a woman scientist. I would also like to say thanks to my friends, Sinan, Naveen, Meeseon, Byunghee, Chi-Deuk for helping me not to burn out in the Physics Department. My parents-in-law, Sue and George Gray, need to be mentioned as an important part of my life ever since I met them. They always showed great interest and supported me in my work and their love made me feel at home in the USA.

I feel it is also important to thank the University of Florida for giving me this opportunity to learn and progress in my academic pursuits. I especially thank my professors and colleagues in the Physics Department who have provided a wonderful environment in which to grow as a physicist, providing stimulating conversation and invaluable advice.

Finally, I would like to thank my husband Aaron Gray who has helped me countless times and supported me in all aspects of my life with love. Without his sacrifice and love, I could not come to this point. Needless to say, he is the most precious present I have ever received from

God. I would also like to thank my baby girl Sharon who has been so good for me as I've prepared my PhD. Most of all, I thank GOD. I really love my family and friends and wish them good luck in their life.

TABLE OF CONTENTS

	<u>page</u>
ACKNOWLEDGMENTS	4
LIST OF FIGURES	10
LIST OF ABBREVIATIONS.....	14
ABSTRACT.....	17
CHAPTER	
1 INTRODUCTION	19
1.1 Characteristics of High T_c Superconductors.....	19
1.1.1 Origin of Pseudogap	20
1.1.2 Experimental Evidence for the Pseudogap.....	23
1.1.3 Point Contact Spectroscopy.....	26
1.2 Characteristics of Manganite.....	28
1.2.1 Crystal Structure of Manganites: Crystal Field Stabilizing Energy and Jahn Teller Distortion.....	29
1.2.2 Double Exchange Mechanism.....	30
1.2.3 A Mechanism in Addition to Double Exchange I: Electron –Phonon Coupling ...	31
1.2.4 A Mechanism in Addition to Double Exchange II: Disorder and Strain	32
2 EXPERIMENTAL SETUP.....	45
2.1 Temperature Control System and Magnet.....	45
2.1.1 Janis Superveritmp Insert with Dewar Description	45
2.1.2 Cooling Procedure	46
2.1.3 AMI Superconducting Magnet.....	46
2.1.4 Thermometry	47
2.2 Point Contact Spectroscopy (PCS) and PCCO Overview	47
2.3 Low Field Magnetoresistance of Manganite Thin Film	49
2.3.1 Thin Film Growth.....	49
2.3.2 Experimental Setup for Transport Measurements.....	51
2.4 Microfabricated Double Layer Structure.....	51
2.4.1 Fabrication of Structure.....	51
2.4.2 Experimental Setup for Capacitance Measurement	52
2.5 Strain and Disorder Effect on Manganite Thin Films	52
3 POINT CONTACT SPECTROSCOPY ON ELECTRON DOPED CUPRATES	63
3.1 Pseudogap Research on Electron Doped Cuprate PCCO Overview	63
3.2 Field Dependent Normal State Gap from PCS	64
3.3 Analysis of Normal State Gap.....	65

3.4 Disorder Effect and Normal State Gap	66
3.5 Summary	68
4 POSITIVE MAGNETORESISTANCE OF MANGANITE THIN FILMS (PMR).....	79
4.1 LPCMO Thin Films (RvsT and Magnetization).....	80
4.2 Metamagnetic Transition and Positive Magnetoresistance	80
4.3 Directional and Strength Dependence of Bias Voltage and Field on PMR.....	81
4.4 Discussions	82
5 MICROFABRICATED DOUBLE LAYER STRUCTURE	90
5.1 Perpendicular Direction of Transport Properties (RvsT).....	90
5.2 Capacitance Effect (From Structure and Intrinsic Phase Separation)	94
5.4 Summary	98
6 STRAIN AND DISORDER EFFECT ON MANGANITE	105
6.1 Overview about Strain and Disorder Effect on Manganite	105
6.2 Disorder and Strain Measurement on LPCMO Thin Films with Three Different Concentration of Pr	107
6.3 Discussion.....	113
7 SUMMARY	127
LIST OF REFERENCES	131
BIOGRAPHICAL SKETCH	138

LIST OF FIGURES

<u>Figure</u>	<u>page</u>
1-1 Phase diagram of a High T_c super conductor.....	36
1-2 Schematic graph of conductance for a metal like junction and a tunnel like junction are plotted [35].....	36
1-3 Model for the perovskite manganite. Re indicates a rare earth material, Mn indicates manganese and O indicates oxygen.	37
1-4 MnO_6 octahedral structure. O indicates oxygen and at the center of the octahedron is Mn.....	38
1-5 Manganese ionization for Mn^{3+} and its outer most orbital (d -orbital) map suggested by density functional methods	39
1-6 Model describing a Jahn-Teller distorted $LaMnO_3$ structure	40
1-7 Hole-doped mixed valence manganite $La_{1-x}Ca_xMnO_3$	40
1-8 Drawing for the double exchange process	41
1-9 Magnetization and resistivity of the LCMO film	41
1-10 Phase diagram for $La_{1-x}Ca_xMnO_3$	42
1-11 CE type charge ordering with orbital ordering, which appears in LPCMO	42
1-12 The phase diagram for $Pr_{1-x}Ca_xMnO_3$	43
1-13 Schematic drawing for the Jahn Teller distorted PCMO due to the small size of the Pr ion.....	44
2-1 Drawings of the Blueman	54
2-2 Superconducting magnet.....	55
2-3 PCS design using bevel gears as a mechanical approaching system.....	55
2-4 Probe for PCS and strain measurements for manganite and details of mechanical approaching system.....	56
2-5 Circuit diagram for point contact spectroscopy	57
2-6 Point contact spectra of a junction between PCCO and a Pt-Rh tip taken at 1.5 K in a field	58

2-7	Electron doped cuprates PCCO	59
2-8	Pulsed laser deposition chamber	59
2-9	Circuit for the measurement of a Sample with High Resistance	60
2-10	Process by which the structure, used to measure transport properties in the direction perpendicular to the manganite LPCMO thin film, was formed.	60
2-11	RIE/ICP (Reactive Ion Etcher with Inductively Coupled Plasma Module)	61
2-12	Two Lock-In Amplifier Methods for the Impedance measurement of the sample.....	61
2-13	Sample holder in which strain is applied using a 3 point beam balance technique.	62
3-1	Differential conductance (dI/dV) vs. Bias voltage curves from the point contact spectroscopy result for junction A	69
3-2	Point Contact spectroscopy result for junction B with magnetic fields from 0 T to 22 T.	69
3-3	Point Contact spectroscopy result for junction C from 0 T to 28 T.....	70
3-4	Point Contact Spectroscopy result of high magnetic fields using junction D.....	70
3-5	For the Junction B case, field dependent conductances across the junction only, after subtracting corresponding sample resistances at each field.....	71
3-6	Detailed view of the conductance across the junction after subtracting the corresponding sample resistances at each field in the negative bias voltage regime.....	72
3-7	Normalized Conductance for the junction B case after getting rid of the linear background conductance from the result of figure 3-6(a).	73
3-8	Normalized conductance for the junction A case after getting rid of the linear background conductance from the result of figure 3-6(b)	73
3-9	Normalized conductance for the junction C case after getting rid of the linear background conductance from the result of figure 3-6(c)	74
3-10	A 2D plot of the normalized conductance, which described as color brightness with the y-axis of the sample bias (mV) and x-axis of the applied field (T) for each junction	75
3-11	Normalized zero bias conductance for the each junctions.....	76
3-12	One example of the correlation gap fitting (junction A with 5 T).....	77

3-13	Slope vs. Field obtained by fitting the correlation gap for the normalized conductance for each junctions.....	78
4-1	Resistance vs. Temperature curves for different magnetic fields.....	85
4-2	Metamagnetic transition and its mechanism.....	86
4-3	Low field magnetoresistance for each direction of applied field.....	87
4-4	Bias voltage dependence of LFMR.....	88
4-5	Phase diagram of $(\text{Tb}_x\text{La}_{1-x})_{0.67}\text{Ca}_{0.33}\text{MnO}_3$	89
5-1	Double layer structure with LPCMO on top of LCMO.....	99
5-2	Current (or electric field) effect for the partially etched double compound layer of LPCMO on top of LCMO.....	100
5-3	Actual measurement of the current dependence of the voltage drop for a different set temperatures while cooling.....	101
5-4	Measurement of the current dependence of the voltage drop for a different set of fields at 115 K while cooling.....	101
5-5	The modulus of the complex sample impedance as a function of temperature.....	102
5-6	Frequency dependent phases of the complex sample impedance as a function of temperature.	102
5-7	Conceptual diagram of the model of our sample structure in the LPCMO phase transition temperature range	103
5-8	Changing the position of a capacitor from figure 5-7 to an equivalent circuit to allow the combination of the two capacitors C_A and C_B into one modified complex capacitor.....	103
5-9	Complex capacitor model for our etched double layer structure, which has a leaky and a lossy part in it due to the phase separated nature (which indicates it is not a perfect insulator) of LPCMO.....	103
5-10	Plot of C_1 Vs. C_2 obtained from suggested modeling in figure 5-9. Warming run values for each temperature were considered in here.....	104
6-1	Comparison of the resistance for the cases in which the measurement is taken right after applying strain (RAAS), after the strain has settled (SS), right after releasing the strain (RARS) and after the strain releasing has settled (RSS) for disordered $(\text{La}_{0.5}\text{Pr}_{0.5})_{0.67}\text{Ca}_{0.33}\text{MnO}_3$ thin films on NGO.....	116

6-2	Resistance obtained from a current source measurement (100nA) for the $(\text{La}_{0.5}\text{Pr}_{0.5})_{0.67}\text{Ca}_{0.33}\text{MnO}_3$ thin films on NGO.....	117
6-3	Resistance obtained by a voltage source measurement for $(\text{La}_{0.5}\text{Pr}_{0.5})_{0.67}\text{Ca}_{0.33}\text{MnO}_3$ thin films on NGO.	118
6-4	Comparison of R vs. T right after applying strain (RAAS), after the strain has settled (SS), right after releasing the strain (RARS) and after releasing the strain and settling (RSS) for the disordered $(\text{La}_{0.6}\text{Pr}_{0.4})_{0.67}\text{Ca}_{0.33}\text{MnO}_3$ thin films on NGO.....	119
6-5	Resistance obtained by a voltage source measurement for the $(\text{La}_{0.6}\text{Pr}_{0.4})_{0.67}\text{Ca}_{0.33}\text{MnO}_3$ 30nm films on NGO	120
6-6	Resistance as a function of temperature obtained by voltage source measurement for the 30 nm $(\text{La}_{0.4}\text{Pr}_{0.6})_{0.67}\text{Ca}_{0.33}\text{MnO}_3$ film on NGO.....	121
6-7	Resistance obtained by voltage source measurement for the $(\text{La}_{0.4}\text{Pr}_{0.6})_{0.67}\text{Ca}_{0.33}\text{MnO}_3$ thin films on NGO	122
6-8	Resistance obtained by voltage source measurement for $(\text{La}_{0.4}\text{Pr}_{0.6})_{0.67}\text{Ca}_{0.33}\text{MnO}_3$ thin films on NGO	123
6-9	Resistance obtained by voltage source measurement for $(\text{La}_{0.4}\text{Pr}_{0.6})_{0.67}\text{Ca}_{0.33}\text{MnO}_3$ thin films on NGO	124
6-10	R vs. time graph while applying strain to the $(\text{La}_{0.5}\text{Pr}_{0.5})_{0.67}\text{Ca}_{0.33}\text{MnO}_3$ thin films on NGO.....	125
6-11	R vs. time graph while applying strain to the $(\text{La}_{0.6}\text{Pr}_{0.4})_{0.67}\text{Ca}_{0.33}\text{MnO}_3$ thin films on NGO.....	125
6-12	R vs. time graph while applying strain to the $(\text{La}_{0.4}\text{Pr}_{0.6})_{0.67}\text{Ca}_{0.33}\text{MnO}_3$ thin films on NGO.....	126

LIST OF ABBREVIATIONS

BCS:	Bardeen-Cooper-Schrieffer
HTSC:	High T_c superconductor
DOS:	Density of states
STM:	Scanning tunneling microscopy
PCS:	Point contact spectroscopy
NHMFL:	National High Magnetic Field lab
BTK:	Blonder, Tinkham and Klapwijk
Re:	Rare earth
AF:	Antiferromagnetic
FM:	Ferromagnetic
COI:	Charge ordered insulating
PCMO:	$\text{Pr}_{1-x}\text{Ca}_x\text{MnO}_3$
LPCMO:	$(\text{L}_y\text{Pr}_{1-y})_{0.67}\text{Ca}_{0.33}\text{MnO}_3$
PMI:	Paramagnetic insulating
FMM:	Ferromagnetic metallic
NGO:	NdGaO_3
CMR:	Colossal Magneto Resistive
CAF:	Canted antiferromagnetic
LCMO:	$\text{La}_{1-x}\text{Ca}_x\text{MnO}_3$
AMI:	American Magnet Institute
LN_2 :	Liquid nitrogen
LHe:	Liquid He
PLD:	Pulsed laser deposition
RIE:	Reactive Ion Etcher

ICP:	Inductively Coupled Plasma
RIE/ICP:	Reactive Ion Etcher with Inductively Coupled Plasma Module
DI:	Deionized
SHIVA:	Sample handling in vacuum
PCCO:	$\text{Pr}_{2-x}\text{Ce}_x\text{CuO}_4$
O:	On the order of
T_c :	Critical temperature
H_c :	Critical field
H_{pg} :	Pseudogap closing field
T^* :	Pseudogap closing temperature
ZBA:	Zero bias anomaly
NSG:	Normal state gap
LFMR:	Low field magnetoresistance
TMR:	Tunneling magnetoresistance
T_{IM} :	Insulator transition temperature
MMT:	Metamagnetic transition
FMM:	Ferromagnetic metallic
PMR:	Positive magnetoresistance
AMR:	Anisotropic magnetoresistive
AFM:	Atomic Force Microscopy
RAAS:	Right after applying strain
SS:	Strain settled
RARS:	Right after releasing the strain
RSS:	After the strain releasing has settled
NDNS:	Nondisordered and Nonstrained

NDS:	Nondisordered and strained
DNS:	Disordered and Nonstrained
NDNSR:	Nondisordered and nonstrained obtained after releasing the strain
DNSR:	Disordered and Nonstrained case after releasing the strain
H_{c2} :	Upper critical field
MR:	Magnetoresistance

Abstract of Dissertation Presented to the Graduate School
of the University of Florida in Partial Fulfillment of the
Requirements for the Degree of Doctor of Philosophy

EFFECT OF DISORDER IN CUPRATES AND MANGANITES

By

Sung Hee Yun

August 2008

Chair: Amlan Biswas

Major: Physics

This dissertation is an inquiry into the characteristics of two representative transition metal oxides, cuprates and manganites.

The pairing mechanism of cuprates is not yet fully understood. The origin of the normal state gap (a unique feature of high T_c superconductors) needs to be ruminated in various ways to understand its relation to the superconducting gap. We have performed point contact spectroscopy experiments using junctions between a normal metal (Pt-Rh) and electron-doped $\text{Pr}_{2-x}\text{Ce}_x\text{CuO}_4$ (PCCO) films and single crystals. To probe the normal state at low temperatures ($T = 1.5$ K), the superconductivity was suppressed by applying high magnetic fields (up to 31 T). From this experiment, we could infer that the normal state gap may not be the “pseudogap,” instead it originates from the presence of disorder in the complex transition metal oxide.

Due to the comparable energies of co-existing phases, manganites exhibit unique dependencies on a variety of external parameters such as light, x-rays, mechanical strain, magnetic field and electric field. These properties not only demonstrate its importance in physics as a strongly correlated system but also mark the potential of this material for practical applications. We studied properties of phase separated hole-doped manganite thin films of $(\text{La}_{1-y}\text{Pr}_y)_{0.67}\text{Ca}_{0.33}\text{MnO}_3$ grown on (110) NdGaO_3 substrates using pulsed laser deposition (PLD).

First, we found a giant positive magnetoresistance of about 30 % at magnetic fields less than 1 T in ultra-thin films (7.5 nm) of $(\text{La}_{0.5}\text{Pr}_{0.5})_{0.67}\text{Ca}_{0.33}\text{MnO}_3$. Second, we were able to control the magnetic phase with an electric field in the out-of-plane direction using a specially designed nano-fabricated double layered structure with two different compositions of manganite, $(\text{La}_{0.4}\text{Pr}_{0.6})_{0.67}\text{Ca}_{0.33}\text{MnO}_3$ and $\text{La}_{0.67}\text{Ca}_{0.33}\text{MnO}_3$. Last, we have studied the effect of strain and disorder on the phase-separated state in thin films of $(\text{La}_{1-y}\text{Pr}_y)_{0.67}\text{Ca}_{0.33}\text{MnO}_3$ (LPCMO, $y = 0.4, 0.5, 0.6$). Our observations show that a small amount of strain ($\sim 10^{-4}$) can move the phase boundaries in the fluid phase separated (FPS) state. A reduction of the piezoresistance in the ion-bombarded samples suggests that such extrinsic disorder can pin the phase boundaries and reduce the fluidity of the FPS state.

CHAPTER 1 INTRODUCTION

1.1 Characteristics of High T_c Superconductors

By 1986, scientists believed the Bardeen-Cooper-Schrieffer (BCS) theory could explain almost all phenomena in superconductivity. The electron-electron attractive potential, which is responsible for the resistanceless motion of electrons in superconducting materials below the critical temperature, could be explained by the electron-phonon interaction. However, as soon as high T_c superconductors were discovered in copper-oxide based materials, known as cuprates, scientist faced new problems. Cuprates are made by doping certain kinds of Mott insulators. They have a common structure, which is composed of a plane of Cu and O separated by charge reservoir planes such as Pr, Y, Ba, La or Sr. Doping creates holes (or electrons) in the copper oxide plane. This destroys Anti-ferromagnetism in the Mott insulator and induces a change of ground state from the insulator to the superconductor.

The reason, their critical temperature is so high and their pairing mechanism is not well understood is the fact that the d-wave symmetry appearing in high T_c superconductor (HTSC) can not have originated from the electron phonon coupling which requires zero angular momentum i.e. s-wave. Most importantly their strange normal state behavior (known as pseudo gap) could not be explained by the BCS theory [1, 2]. Figure 1-1[3] shows the phase diagram for hole doped and electron doped HTSCs. There are parts of the phase diagram, which are not very well understood due to the normal state gap, a unique feature of HTSCs. Optimistically hoping that this normal state gap in the superconducting dome will guide us to a clarification of the pairing mechanism of HTSCs, this feature will be focus of this dissertation.

1.1.1 Origin of Pseudogap

There are as many theoretical models for the pseudogap in cuprates as there are bamboo sprouts after rain. An attempt to categorize them into groups therefore seems to produce more confusion than clarification. There appears to be no clear-cut way to classify the different models. They are entangled like holes in a sea sponge. However, for convenience, I have sorted the models into the following six categories, which are resonance valence bond (RVB), magnetic order, strong coupling, phase fluctuation, semiconductor-superconductor model and interlayer coupling model.

Resonance valence bond

The insulating state with magnetic singlet pairs found in oxide superconductors was considered to be a resonating valence bond (RVB) state by Anderson[4]. These pairs induce a spin gap and this gap is the pseudogap in this model. If the doping is high enough, then the spinons can become holons, which Bose-Einstein condense (BEC) and form the superconducting state at T_c . Since these quasiparticle excitations are based on spin-charge separation, the transition temperatures for the spinon pairing state (RVB state) and holon pairing state (BEC state) can be different [5]. The pseudogap transport properties were predicted according to this model using Ginzburg–Landau theory [6]. This gauge theory suggests the possibility of a strong coupling of the spinons and holons in the superconducting state due to the gauge field fluctuations.

Magnetic scenario

The dominant magnetic interaction between quasiparticles in cuprate superconductors is antiferromagnetic spin fluctuation or spin density wave. The possibility that a pseudogap could exist in the electronic density of states for the cuprate superconductor due to antiferromagnetic spin fluctuations has been suggested [7]. The renormalized spin susceptibility with quasiparticle excitations shows strong fluctuations in the spin-density wave (SDW) state. The self-energy

between quasiparticles and the unstable SDW induces long range order which is called mode-mode coupling at finite temperature. Quasiparticle excitations show marginal Fermi-liquid behavior near this SDW instability, and this can be considered to be a pseudogap state [8]. Due to the strong antiferromagnetic correlations between quasiparticles in the nearly antiferromagnetic Fermi liquids model in two dimensions, the normal state of cuprates can show distinct magnetic phases including a pseudogap in the quasiparticle density of states below a certain temperature. This feature is a precursor of the spin-density-wave (SDW) state. The peak of the dynamical spin susceptibility observed at $Q = (\pi, \pi)$ arises due to the presence of two kinds of quasiparticles [9] viz. quasiparticles at the Fermi surface near the antiferromagnetic Brillouin zone (or in short hot quasiparticles) and cold quasiparticles. Hot quasiparticles are strongly correlated to the antiferromagnetic spin fluctuation, which means it will be strongly scattered by fluctuations and induces the gap (pseudogap) at the hot spot in contrast to the cold quasiparticle [9]. In this model, superconductivity is achieved with the opening of a gap in the cold quasiparticle spectrum and only these cold quasiparticles contribute to the superfluid density. Therefore the magnitude of the pseudogap and pseudogap opening temperature has no relation with critical temperature for the superconducting gap. This means that magnetic order and superconductivity are not connected [10]. The theory that the pseudogap is due to microscopic phase separation between metallic stripes and insulating antiferromagnetic stripes will also be in this category [11]. In this scenario, a build up of the antiferromagnetic correlation induced spin gap is suggested to be the pseudogap.

Strong coupling scenario (preformed pairs)

In the strong coupling model, the pseudogap is formed in the ground state of a crossover from the BCS to Bose Einstein condensation (BEC) at finite temperature, which happens when $k_B T_c$ is

much smaller than the pairing energy [12]. Cooper pairs without long range phase coherence due to a strong attractive interaction can be formed before the pairs condense and the material becomes superconducting. These pairs are called preformed pairs and this pairing correlation is the origin of the pseudogap in this model [13]. A finite temperature effect of this model suggests that in this crossover region from BCS to BEC, the order parameter and energy gap have different energy scales which allows the superconducting gap and the pseudogap to have the same energy scale as the temperature increases above T_c . On the contrary, in the ground state, the order parameter and the energy gap are the same [14]. The strong electron correlation effect induced pseudogap has the characteristics of excitations with an electron like nature [15].

Phase fluctuation scenarios

This phase fluctuation model is also based on the strong coupling scenario for superconductivity. However, in this model, the pseudogap is induced by a strong superconducting fluctuation, which is accompanied by strong coupling superconductivity [16]. Cuprates have less phase stiffness than conventional superconductors and this induces classical and quantum phase fluctuations [17]. The low temperature properties of cuprates will be affected by this fluctuation. For a strong coupling superconducting case, it has been suggested that superconducting fluctuations induce pre-formed pairs and the pseudogap appears as a result of thermal excitation in these pre-formed pairs [16]. Long-range order will be disturbed by these phase fluctuations [18]. In a strongly correlated electron system, small fluctuations near the quantum critical point can result in a huge effect on the ground state of the system. This can induce the complex order parameter in one side (under doped side in the hole-doped cuprates case) of the quantum critical point. This imaginary part of the order parameter may be related to the pseudogap [19].

Semiconductor and superconductor model

That the pseudogap is a semiconducting gap with the possible existence of competing order parameters, for example a charge-density wave (CDW), was suggested by Pistoiesi and Nozières [20]. The existence of a quantum critical point at optimal doping supports the competing order parameter theory due to the formation of a CDW [21]. The effect of strong anisotropy (d-wave) in the order parameter for this semiconductor superconductor model with CDW, was investigated [22]. It predicts that the pseudogap will be dominated only in the antinode region and will be diminished around the node. However, the absence of a thermodynamic phase transition needs to be explained for this competing order parameter theory.

Interlayer coupling scenario

Another peculiar candidate for the origin of the pseudogap is the coupling between interlayers which form holons inducing a spin gap in bilayer cuprates [23, 24] This model predicts that the difference between the pseudogap opening temperature and the superconducting critical temperature will increase due to the interlayer coupling.

1.1.2 Experimental Evidence for the Pseudogap

The first experimental observation of the pseudogap in hole-doped cuprates was obtained from a nuclear magnetic resonance (NMR) experiment [25]. The magnetic field effect on the spin gap was studied on optimally doped $\text{YBa}_2\text{Cu}_3\text{O}_{7-\delta}$ using NMR when the temperature T is near and above T_c [25]. It showed no magnetic field dependence. This result was interpreted as evidence for the independence of the pseudogap and superconducting fluctuations when this spin gap is considered to be the pseudogap. Later experiments related to charge channels (e.g. Tunneling, angle resolved photoemission spectroscopy (ARPES), optical conductivity etc.) also showed a pseudogap and demonstrated that the gap size was temperature independent [26]. The pseudogaps of Bi2212 and Hg Br₂-Bi2212 were studied using intrinsic tunneling spectroscopy [27]. In this experiment, the pseudogap found along the c-axis, did not change with H or T ,

contrary to the superconducting gap. This result was also interpreted as independence of the pseudogap and superconducting gap i.e. the two gaps had different origins. However, there have also been many attempts to understand those results assuming the pseudogap and superconducting gap are related. In the limit of strong coupling, it is possible that the characteristic magnetic field is too large near the pseudogap opening temperature to observe a magnetic field dependence of the pseudogap [28]. A more detailed model [29] explains the field dependence of the pseudogap in various doping ranges when the pseudogap phase is due to d-density wave order. This model also is in the category of preformed pairing. In this model, as doping increases, sensitivity to the field increases until the pseudogap itself vanishes in the overdoped regime. The relation between the pseudogap closing field and the pseudogap closing temperature and the low field insensitivity in the underdoped regime was explained using the anisotropic lattice model with the pseudogap as a precursor to superconductivity [30]. Recently, the existence of vortex excitations above T_c was observed by Nernst effect experiments in hole-doped cuprates. This supports the pseudogap as a phase disordered pairing due to the creation of thermal vortices. Pseudogap studies on electron-doped cuprates are not yet comparable to the wide body of research on the pseudogap in hole-doped cuprates but they are catching up rapidly. The pseudogap found in high-resolution ARPES experiments on electron-doped cuprates $\text{Nd}_{1.85}\text{Ce}_{0.15}\text{CuO}_4$, cast doubt on the universal explanations of the pseudogap found in hole-doped and electron-doped cuprates [31]. In this experiment the origin of pseudogap was interpreted to be antiferromagnetic spin fluctuations in two dimensions [32]. However, the pseudogap was also observed as a negative magneto resistance in the electron-doped cuprate $\text{Sm}_{2-x}\text{Ce}_x\text{CuO}_{4-\delta}$ along the c-axis using a specially designed mesa structure suggesting a similarity of the pseudogap in hole-doped and electron-doped cuprates by interpreting a spin correlation as the origin of the

pseudogap found in both doped cases [33]. A unique feature of the n-doped cuprates is that it is possible to probe the normal state inside the superconducting dome for the entire doping range by driving the superconductor into the normal state with a field H greater than the upper critical field H_{c2} , due to the relatively low values of H_{c2} (~ 10 T at low temperatures for the optimally doped compounds). Tunneling across grain boundary junctions and point-contact spectroscopy in magnetic fields $H > H_{c2}$ have clearly shown the presence of a normal state gap (NSG) in the density of states, which is comparable in energy scale to the superconducting gap and which increases in energy scale as the doping is decreased [34, 35, 36]. Alff et al. have mapped the region in the phase diagram where this NSG is observed [3]. The NSG observed in n-doped cuprates shows a similar behavior with doping as the pseudogap in p-doped cuprates [35, 3, 37]. If the NSG in n-doped cuprates is indeed analogous to the pseudogap in p-doped cuprates, then Alff et al. result suggests that the pseudogap in n-doped cuprates is present inside the superconducting dome and vanishes at a doping level close to the optimum value ($x \sim 0.16$), which supports the competing order parameter scenario [3]. However, Dagan et al. have performed tunneling spectroscopy measurements on thin films of $\text{Pr}_{2-x}\text{Ce}_x\text{CuO}_4$ for the doping range $0.11 < x < 0.19$ and have shown that the NSG is observed well into the overdoped region [38]. In fact, in the overdoped region ($x > 0.17$) the temperature T above which the NSG vanishes is approximately equal to T_c . This result provides strong evidence that the NSG is related to the superconductivity in PCCO and if the NSG is the pseudogap, supports the pre-formed pairing scenario.

With this background, in the next section I will describe the technique of point contact spectroscopy and in chapter 3, I will describe our point contact spectroscopy results on the electron-doped cuprate $\text{Pr}_{2-x}\text{Ce}_x\text{CuO}_4$.

1.1.3 Point Contact Spectroscopy

Tunneling spectroscopy has proven to be a powerful technique for studying the electronic density of states (DOS) near the Fermi level in conventional BCS superconductors. However, the short coherence length in high- T_c cuprate superconductors (HTSC) means that tunneling spectroscopy, which probes the surface density of states, can provide information for only a few atomic layers beneath the surface. This imposes strict requirements for the quality of the sample surface. The best results are obtained on samples that have been cleaved in-situ before forming the tunnel junction. Hence, the most significant tunneling data have been obtained on $\text{Bi}_2\text{Sr}_2\text{Ca}_1\text{Cu}_2\text{O}_8$, which has a very convenient cleavage plane. This leaves out the large set of other cuprates, which do not share this particular property. For such materials, it is useful to construct tunnel junctions using the native insulating layer formed on the cuprate as the insulating tunnel barrier. This can be done either by forming planar tunnel junctions or by performing point contact spectroscopy. Both scanning tunneling microscopy (STM) and point contact spectroscopy (PCS) might be used to study the electron excitation spectrum in metallic solids. Unlike STM, PCS is based on the formation of micro-channels, which means mechanical contact in between two materials. Therefore the conductance of a ballistic metallic PCS junction is 10^5 times larger than the conductance of a typical STM tunneling junction. For materials, such as the electron-doped superconductor $\text{Pr}_{2-x}\text{Ce}_x\text{CuO}_4$ (PCCO), which are easily oxidized, making an insulating barrier on the surface of the film, STM is extremely difficult. But the fact that either the tip or the film go through the insulating barrier to make a micro-channel in PCS, makes this technique very useful to study high T_c cuprates. In addition to this, PCS is not significantly affected by external vibration, which is an important factor to consider when choosing a measurement method for the water-cooled magnets in the DC High Field Facility at the Magnet Lab. Contact size is very critical for PCS. First, for PCS or tunneling spectroscopy, the contact

size should satisfy the ballistic limit criterion (known as the Sharvin limit) since in that limit the energy resolution can be trusted. The main difference between tunneling spectroscopy and PCS can be explained by contact size. If the contact size ' a ' satisfies $l_e > a > 0.1\xi$, where ξ is the coherence length and l_e is the elastic mean free path of the film, then the junction is in the Sharvin limit and suitable for PCS [39]. Since Andreev reflection starts to disappear gradually when $a < 0.1\xi$, there the junction is in the tunneling limit. The main difference between the conductance features in the two different limits, are shown in Fig 2[35].

Significant progress has been made in the fabrication of planar and point contact junctions and these experiments have given invaluable information about the DOS of HTSCs and other new superconductors.

Why do we need to perform PCS at high magnetic fields? A theory for the phenomenon of high- T_c superconductivity has to explain the underlying pairing mechanism and why it happens at such high temperatures. Hence, one needs to understand the original state that was destabilized to give rise to superconductivity. We will call this non-superconducting state, the “normal state”. Hence, it is essential to understand the normal state of HTSC in order to explain the mechanism behind the high critical temperatures. The T_c (about 25 K) and upper critical fields (about 10 T at 2 K) of n-doped cuprates are significantly lower than p-doped cuprates. Hence, it is possible to study the normal state of these materials at low temperatures at the National High Magnetic Field lab in Tallahassee (NHMFL) [40, 41].

The usefulness of PCS for studying superconductors is greatly enhanced by a theory developed by Blonder, Tinkham and Klapwijk (BTK), in which they discuss the dependence of the I-V (current-voltage) characteristics of a junction between a superconductor and normal metal on the strength of the barrier between the electrodes (denoted by a dimensionless number

Z) [29]. This theory enables us to extract information from PCS data. It also suggests that for large barrier strengths ($Z \gg 1$), a point contact junction behaves similarly to a tunnel junction.

The field dependence of the pseudogap was predicted by S.Chakravarty *et. al* [29], as the doping increases, the sensitivity increases which is in contrast to the fact that the gap itself vanishes as the doping increases towards the overdoped regime. Here, the pseudogap was due to the d-density wave order, which also indicates that the pseudogap has the same orbital symmetry as the superconducting gap and its field effect was considered as the broken symmetry of the d-density wave order. The fact that the phase transition to the pseudogap will be suppressed by the presence of disorder was predicted [42].

1.2 Characteristics of Manganite

Manganite, a strongly correlated electron system, shows a variety of interesting features. It is sensitive to many external parameters like light [43], x-ray [44], magnetic field [45-49], electric field (or current)[50, 51] and structural strain [52] etc. due to the complex entangled relationship between electron density, orbital ordering, spin and lattice structure. Several attempts have been made to explain these phenomena including the double exchange mechanism [53-55], Jahn Teller distortion and polaron theory. They could explain the low temperature and high temperature behavior separately and could be linked somewhat by consideration of the magnetic or structural effects on the electric transport properties. However it is necessary to study the microscopic features of this material for a complete understanding of the unsolved problems surrounding these materials especially those related to the competing ground states. The ground state of these phase-separated manganites is composed of a glass like nanoscale or grain like micron scale mixture of static or fluid phases with temperature dependent phase fluctuations in the presence of quenched disorder [56-59]. Therefore this dissertation is focused

on the static and dynamic phase separation of mixed valance manganite thin films and various possible methods for controlling this phase separated state.

1.2.1 Crystal Structure of Manganites: Crystal Field Stabilizing Energy and Jahn Teller Distortion

Figure 1-3 shows the basic structure of manganites which are composed of rare earth (Re) materials (La, Ce, Pr, Nd, Y, Eu ,etc), manganese (Mn) and oxygen (O). For the chemical stoichiometry of the compound ReMnO_3 , Mn can have only Mn^{3+} ionization, which means the outermost orbital has 4 electrons. Since, most transport properties are decided by the characteristics of the Mn-O plane, we need to focus on the Mn-O structure. This octahedral structure of MnO_6 is shown in figure 1-4. The Crystal field is induced by the Coulomb interaction between different electron orbitals. This octahedron consists of six oxygen ligands around a Mn ion and is one of the most common types of complex for this crystal field. Therefore this crystal field breaks the degeneracy of the energy of the d orbital and splits it into 2 types of energy levels, which are $e_g (d_z^2, d_{x^2-y^2})$ and $t_{2g} (d_{xy}, d_{xz} \text{ and } d_{yz})$. For the octahedron structure, the repulsion between the ligands and electron density states ($d_z^2, d_{x^2-y^2}$) of e_g are stronger than that between the ligands and states ($d_{xy}, d_{xz} \text{ and } d_{yz}$) of t_{2g} . This results in the e_g state having a higher energy than the t_{2g} state (it will be the opposite for the tetragonal structure). At the same time, we need to consider two types of energies, which are the repulsive energy between electrons in the same orbital and the crystal field splitting energy (E_{cf} in figure 1-5) of the degenerate states. In the MnO_6 complex, the former energy is stronger than the later; therefore the system will prefer a high spin state i.e. instead of following the Aufbau principle, it will satisfy Hund's rule as shown in figure 1-5 [60]. Another important type of crystal field effect for this octahedral complex with degenerate eigenstates is the Jahn-Teller distortion. Since either t_{2g} or e_g themselves are still degenerate and the e_g orbital has an unoccupied state, a

geometrical distortion of the structure will result in a net gain of the total energy as shown in figure 1-5. Therefore, the relative energy of each state will depend on the direction of distortion in the structure. For example, if it was stretched along the z-axis, the d_z^2 state will have a lower energy than the $d_{x^2-y^2}$ state in e_g . Figure 1-6 shows the resultant structure of this Jahn-Teller distortion for LaMnO_3 .

1.2.2 Double Exchange Mechanism

Figure 1-7 shows one example of a hole-doped mixed valence manganite $\text{La}_{1-x}\text{Ca}_x\text{MnO}_3$ (LCMO). This mixed valence electron configuration in the manganese ions gives a degeneracy of two spatially different manganite states by transferring electrons from one manganese ion site to the other manganese ion site through oxygen as described in figure 1-8. During this process, the electron hopping probability depends on the core spin of each Mn ion due to the strong Hund's coupling. First it was suggested by Zener that this exchange-induced hopping is possible only when these nearest two manganese core spins are ferromagnetically aligned. By estimating the splitting energy of this degenerate state to be $k_B T_C$, where T_C is the Curie temperature, the conductivity can be inferred to be $\sigma \sim \chi e^2 / ah T_C / T$ [53], where χ is Mn^{4+} fraction and a is the Mn-Mn distance 1-1. However, later Anderson and Hasegawa calculated this hopping probability for a more general alignment of the core spins by introducing a quantum mechanical view and it was shown that the conductivity and angle between core spins are related by $\cos(\theta/2)$ when θ indicates the relative angle between two manganese core spins. This double exchange mechanism gives an explanation of the relationship between magnetism and electron conductivity and it is proven by the experiment as shown in figure 1-9. It is clearly shown for the mixed-valent manganese oxide $\text{La}_{1-x}\text{Ca}_x\text{MnO}_3$ that the ferromagnetic state is directly related to the conducting state of this material. The relationship, as explained by the double exchange

mechanism, between the conductivity and Mn-Mn distance in the ferromagnetic metallic region is not sufficient to deal with systems with different A-site cations. The relationship in these systems could be partially explained by introducing the tolerance factor $f=(r_{Mn}+r_O)/(r_{A\ site}+r_O)$, where r_{Mn} , r_O , and $r_{A\ site}$ indicate the averaged ionic size of Mn, oxygen, and the A site cation respectively. This was shown by the experiment concerning manganites with a different A site cation radii with a fixed doping ratio [61]. This correction is necessary because of the Mn-O-Mn bond angle dependent T_c due to the effect of Jahn-Teller distortion. This mechanism will be discussed in greater detail in the next section.

1.2.3 A Mechanism in Addition to Double Exchange I: Electron –Phonon Coupling

Phenomena such as the existence of the ferromagnetic insulating state, different types of orderings which are related to the different phases, the phase transition between different states or the coexistence of those phases states etc. are difficult to explain only by the double exchange mechanism. Therefore, a further explanation of the orderings and related phases and their dynamics for this mixed valent perovskite manganite is needed.

Figure 1-10 [62] shows one possible origin of the new mechanism. This phase diagram strongly suggests that the effect of the electron-lattice coupling by showing distinctive characteristic features in phases with a doping ratio, x , that is a multiple of 1/8 other than $x=0.25$ and 0.75. The electron-lattice coupling is directly related to the polaron formation, which is induced by the trapping of charge carriers due to Jahn Teller distortion of the MnO_6 octahedron [63] and this is confirmed by the observation of the local Jahn Teller distortion (so called on site small polaron) in the metallic phase of $La_{1-x}Sr_xMnO_3$ ($0<x<0.4$) using pulsed neutron scattering [64]. The competition between this electron-phonon coupling and double exchange is considered to be the source of intrinsic phase separation in perovskite manganites. This electron-lattice coupling induces the charge ordered phase and orbital ordered phase, which can also be the

dominant phases in manganites. Figure 1-11 shows CE type antiferromagnetic (AFM) charge and orbital ordered phases. The charge ordering, which can be described by antiferromagnetic superexchange in this case, often appears as stripes of Jahn-Teller distorted Mn^{3+} when they are accommodated within the antiferromagnetic insulating phase [65]. This can be found in both $La_{1-x}Ca_xMnO_3$ and $Pr_{1-x}Sr_xMnO_3$ with certain doping ranges as shown in figure 1-10 and 1-12[66]. Orbital ordering plays an important role in the FM (ferromagnetic) phase to AFM phase transition for $La_{0.5}Ca_{0.5}MnO_3$ [67]. The former FM phase is a phase-separated state consisting of orbital disordered AFM charge ordered insulating (COI) domains and charge disordered FM domains. And the later AFM phase is purely orbital disordered AFM COI. Therefore for this compound, the FM phase to AFM phase transition is primarily related to the orbital ordering rather than charge ordering.

The size of the cation affects the phase diagram by introducing charge ordering or orbital ordering due to Jahn Teller distortion in the MnO_6 octahedron as shown in figure 1-13 of $Pr_{1-x}Ca_xMnO_3$ (PCMO). If we compare figures 1-10 and 1-12, it could be observed that with the same doping ratio we can get different phases for different A site cations (La vs. Pr). Therefore, it is expected that if we include two rare earth materials with a fixed doping ratio ($0.3 < x < 0.5$), we can study the effect of the electron-lattice coupling for the mixed phase state of manganite. For this reason, the manganite composition selected for this dissertation is $(L_yPr_{1-y})_{0.67}Ca_{0.33}MnO_3$ (LPCMO), which can have paramagnetic insulating (PMI), ferromagnetic metallic (FMM) and charge (orbital)-ordered insulating (COI) phases corresponding to pseudocubic, cubic and orthorhombic structures for the MnO_6 bonding respectively.

1.2.4 A Mechanism in Addition to Double Exchange II: Disorder and Strain

Manganites are not a perfect crystal. Therefore, considering the effect of disorder in this material, especially, for mixed valence manganites is very appropriate. In addition to this, as a

strongly correlated electron system, structural strain can affect other properties of manganites as well. Disorder in this material is expected to suppress the mobility of the electrons and as a result it is expected to decrease the T_c and/or increase the residual resistivity [68] or suppress the magnetoresistance [69]. It is necessary to pay attention to the methods used to introduce disorder into the system to understand its mechanism. One possible way is by changing the doping ratio from the canonical double exchange system, $\text{La}_{0.7}\text{Sr}_{0.3}\text{MnO}_3$, i.e. modifying the A-site ionic valences to control the electron density. The second way to control disorder is by using a different growth mode including oxygen annealing and using different substrates. This can induce different structural symmetry and/or different structural strain [70]. The third way is by changing the chemical pressure by substituting a doping component Sr to Ca or Ba with a fixed doping ratio $x=0.3$. This results in a modification of the length and angle of the Mn-O-Mn bonds and in this case the disorder can be quantified as the variation of the radius of the A-site cation ($\sigma^2 = \langle r^2 \rangle - \langle r \rangle^2$) [70, 68, 69]. We will call the disorder induced using the methods discussed above “intrinsic disorder”. Due to the fact that experiments, in which this kind of intrinsic disorder is introduced, cannot distinguish between the effects of pure disorder and those of the strain itself, the role of disorder in the system, that is whether it acts as a scattering source for mobile electrons or magnons due to the presence of localized corresponding states [70] or it accommodates built in strain to localize electrons assisted by Jahn-Teller distortion, is not yet clear [69].

Now let us turn our attention to the effect of strain on manganite with a brief review of experiments related to this topic. The thickness dependent magnetoresistance of $\text{La}_{1-x}\text{Ca}_x\text{MnO}_3$ on LaAlO_3 substrates [72] and the thickness dependent transport properties of $\text{Nd}_{0.5}\text{Sr}_{0.5}\text{MnO}_3$ thin films on LaAlO_3 substrates [73] were explained by lattice strain. Thin films of

$\text{La}_{0.9}\text{Sr}_{0.1}\text{MnO}_3$ on SrTiO_3 substrates showed an unexpected metal insulator transition due to the compressive substrate induced strain [74] and $\text{La}_{0.7}\text{Sr}_{0.3}\text{MnO}_3$ films on different substrates LaAlO_3 and SrTiO_3 , which induce compressive and tensile strain respectively, on the $\text{La}_{0.7}\text{Sr}_{0.3}\text{MnO}_3$ structure, showed magnetization with a different direction [75]. In-plane anisotropy in the magnetic hysteresis loops of $\text{La}_{0.7}\text{Ca}_{0.3}\text{MnO}_3$ films on NdGaO_3 (NGO) substrates (low epitaxial stress) was suggested to have originated from the anisotropy of the in plane stress [76]. It was observed that variations in the oxygen content of single phase thin films of $\text{La}_{1-x}\text{Ca}_x\text{MnO}_3$ on LaAlO_3 ($0.1 < x < 0.5$) can result in different phases by inducing strain effects to the structure due to cationic vacancies [77]. Based on the theory of strain induced hopping amplitude change, phase competition in the phase-separated state will be affected by substrate-induced strain [78]. However, this conclusion is controversial. Phase separation cannot explain an experiment on $\text{La}_{2/3}\text{Ca}_{1/3}\text{MnO}_3$ on SrTiO_3 , which shows an anomaly of the transport properties, induced by biaxial strain, in which the film has metallic properties in the plane of the film and insulating properties in the direction perpendicular to the plane of film. This experiment suggests that strain accommodates orbital orderings and it results in orbitally ordered layers of ferromagnetic manganese oxide planes to form an A-type antiferromagnetic state [79]. The experiments suggested above can be categorized as thickness dependent, substrate dependent and/or oxygen content dependent magnetic and electric transport measurements. The experiments above, in which strain is considered, report results that are expected from the disorder effect on the films, which are a decrease of the transition temperature, an increase of the residual resistivity and an enhancement of the magnetoresistance at the Colossal Magneto Resistive (CMR) region etc. The main cause of ambiguity is that these experiments cannot distinguish the effect of disorder from that of strain. Therefore, this dissertation suggests new

methods to apply extrinsic disorder (more precisely increasing the electrically dead layers by creating defects) and mechanical strain separately to manganite thin film which grown on top of comparably small lattice mismatch substrate. We will compare the effect of two different type of disorder.

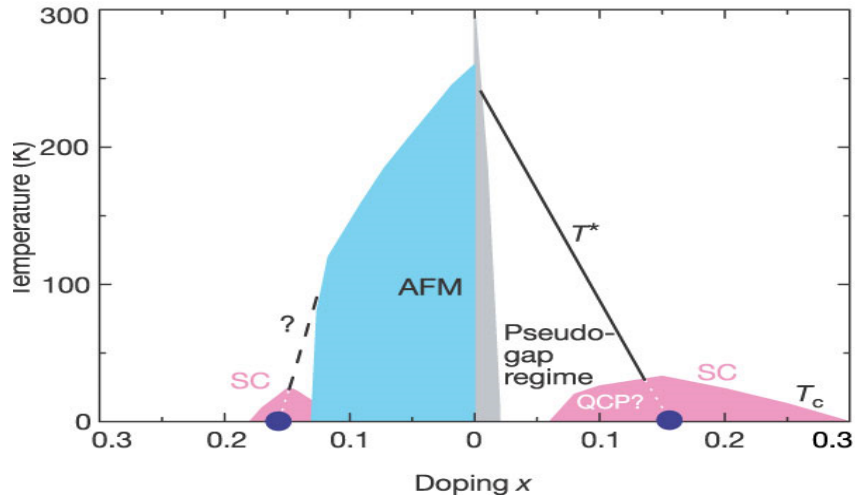


Figure 1-1: Phase diagram of a High T_c super conductor. Left for electron doped HTSC – (La,Pr,Nd) Ce CuO₄, right for LaSrCuO₄(hole doped HTSC) [3].

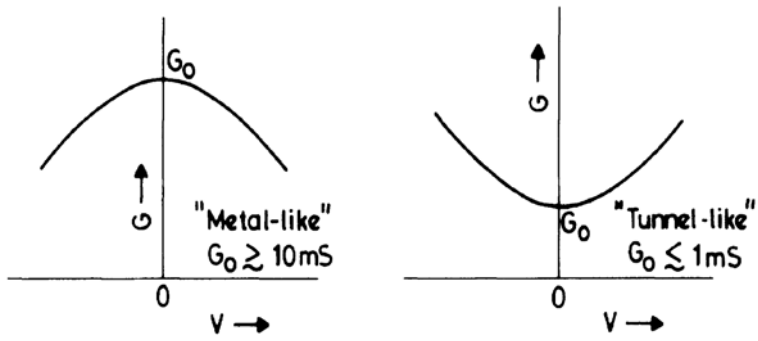


Figure 1-2: Schematic graph of conductance for a metal like junction and a tunnel like junction are plotted [35].

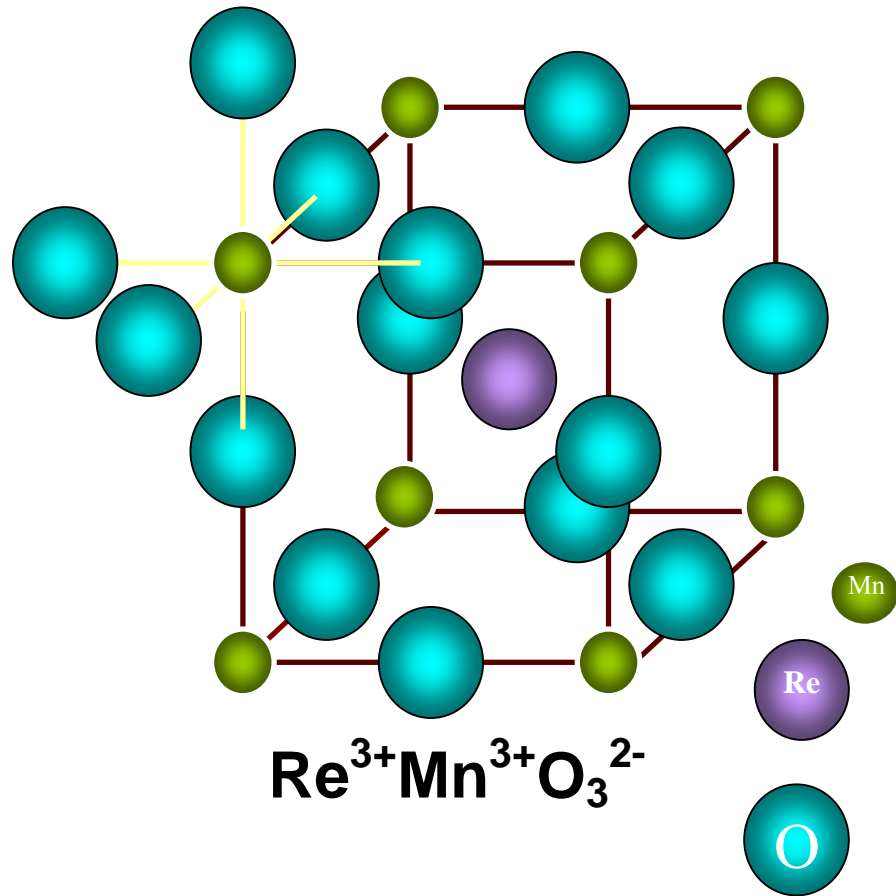
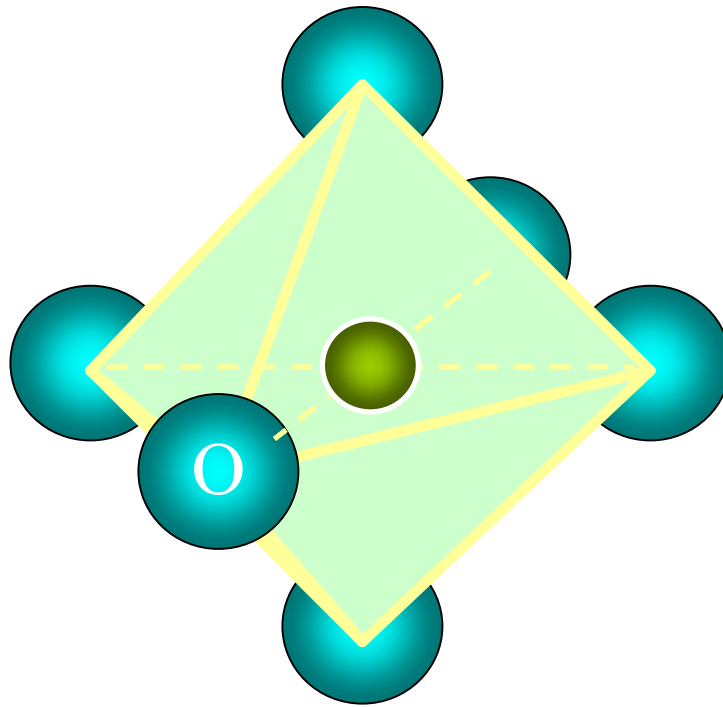


Figure 1-3: Model for the perovskite manganite. Re indicates a rare earth material, Mn indicates manganese and O indicates oxygen.



Octahedral MnO_6

Figure 1-4: MnO_6 octahedral structure. O indicates oxygen and at the center of the octahedron is Mn.

$^{25}\text{Mn}: 1s^2, 2s^2, 2p^6, 3s^2, 3p^6, 4s^2, 3d^5$

$\text{Mn}^{3+}: 1s^2, 2s^2, 2p^6, 3s^2, 3p^6, 3d^4$

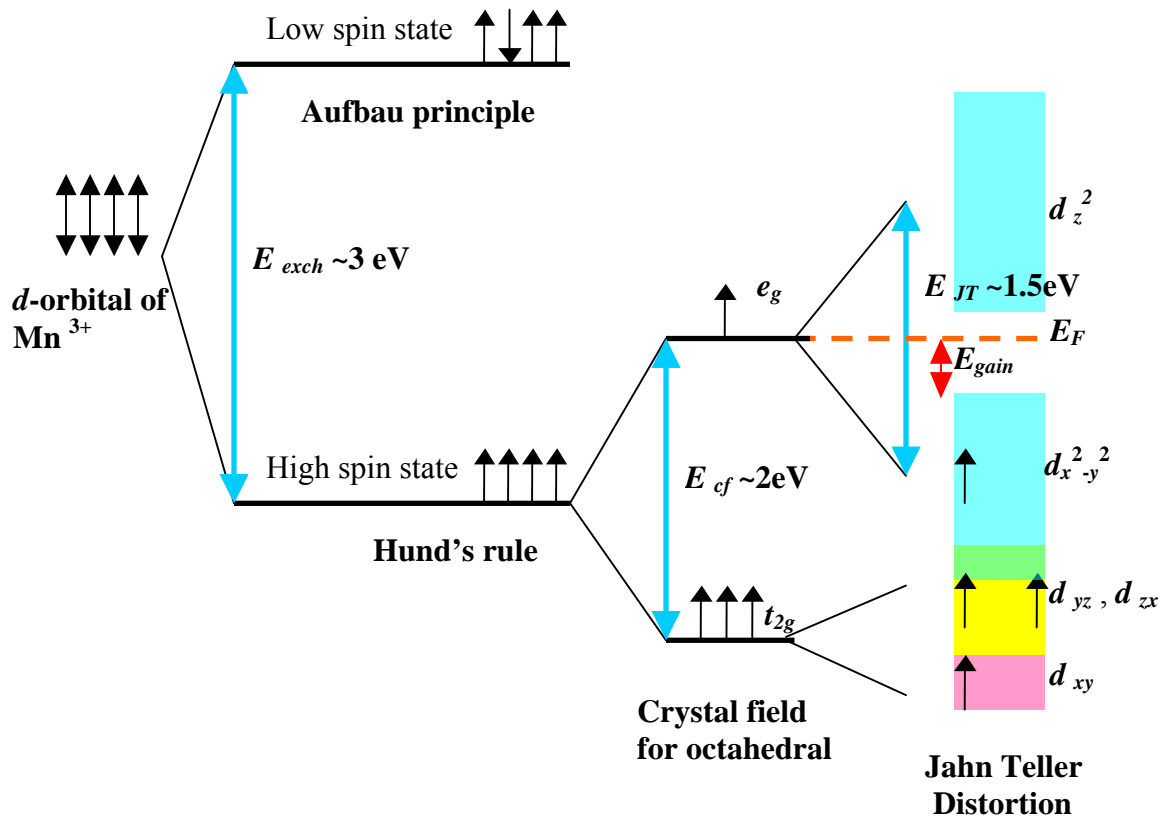


Figure 1-5: Manganese ionization for Mn^{3+} and its outer most orbital (d -orbital) map suggested by density functional methods. The Energy band splits due to exchange, crystal field, and J-T interactions. The e_g orbital includes the $d_{x^2-y^2}$ state and d_z^2 state and the t_{2g} orbital includes d_{xy}, d_{yz} and d_{zx} . The E_{gain} (Energy gain) induced by J-T distortion is approximately 0.25 eV . The Jahn Teller distorted band splitting suggested by the figure above assumes the octahedral structure is compressed along the z -axis. The bandwidths are ~ 1.3 to 1.8 eV [61].

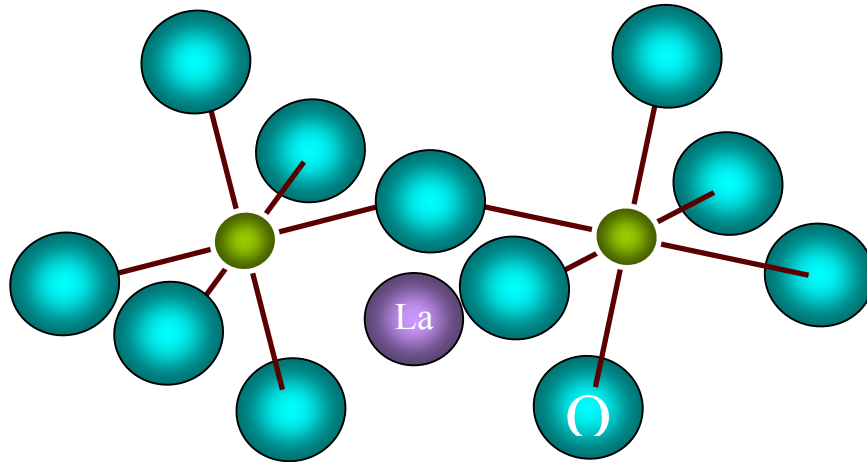


Figure 1-6: Model describing a Jahn-Teller distorted LaMnO_3 structure

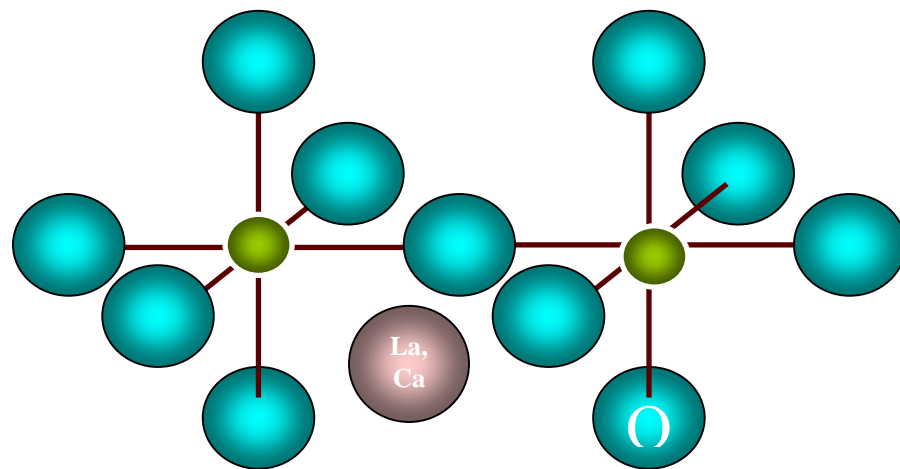


Figure 1-7: Hole-doped mixed valence manganite $\text{La}_{1-x}\text{Ca}_x\text{MnO}_3$. For certain doping ($0.2 < x < 0.5$) the structure is cubic.

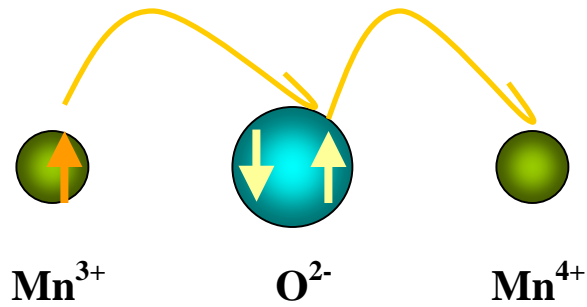


Figure 1-8: Drawing for the double exchange process. A Mobile electron in the d-orbital hops from the Mn^{3+} site to the O^{2-} and at the same time an electron in the p-orbital in the O^{2-} hops to the $\text{Mn}^{4+} e_g$ state in the d-orbital. This exchange is possible only if the spin of the core electrons (t_{2g} electrons) of both Mn^{3+} and Mn^{4+} are parallel.

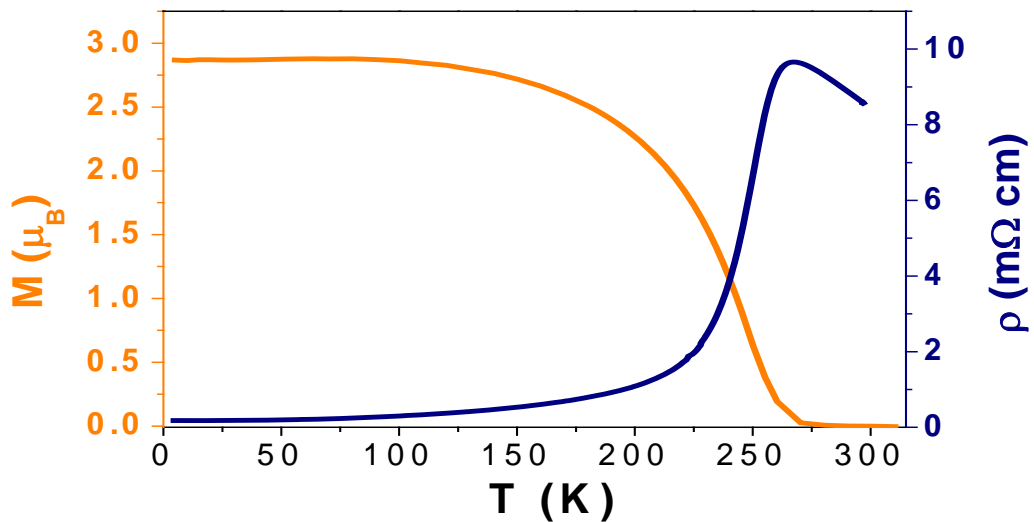


Figure 1-9: Magnetization and resistivity of the LCMO film. It shows the coexistence of the ferromagnetic phase with the metallic phase and the insulating phase with paramagnetic phase, which supports the double exchange mechanism.

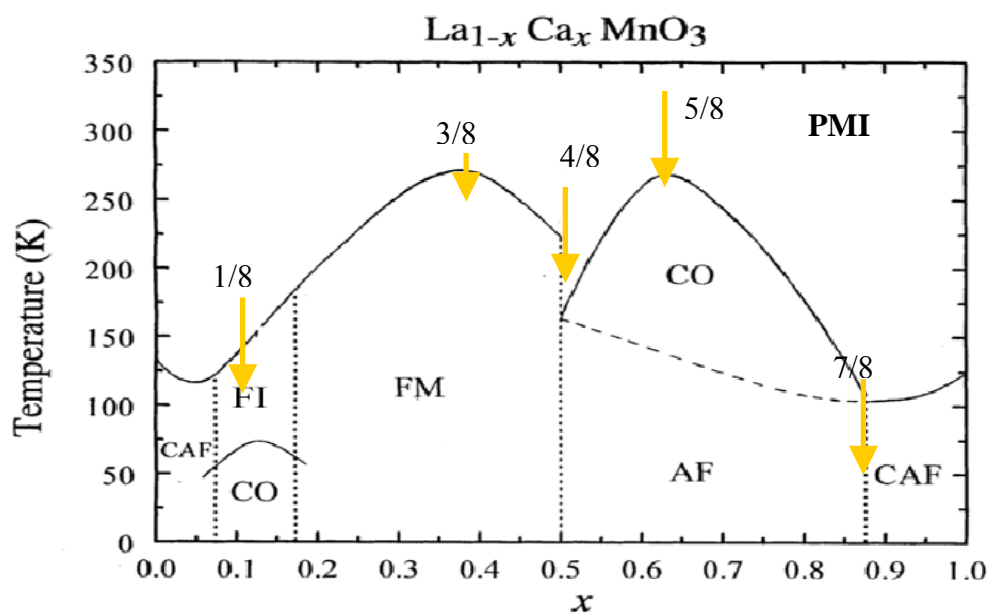


Figure 1-10: Phase diagram for $\text{La}_{1-x}\text{Ca}_x\text{MnO}_3$. CAF, FI, CO, FM and AF indicate Canted antiferromagnetic, Ferromagnetic insulating, Charge ordered, Ferromagnetic and antiferromagnetic respectively [63].

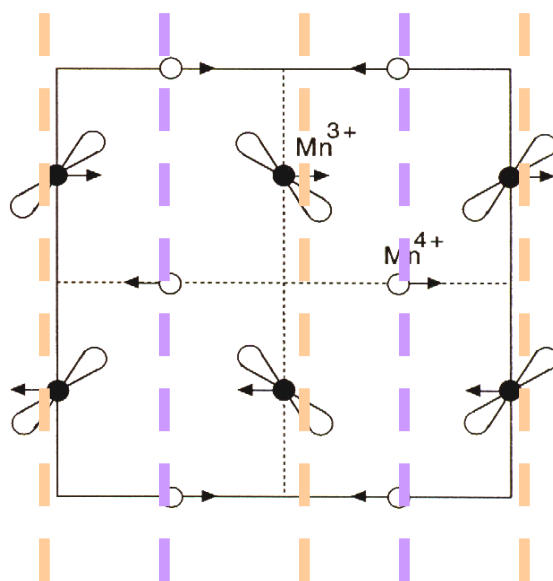


Figure 1-11: CE type charge ordering with orbital ordering, which appears in LPCMO. The dotted lines indicate that the Mn^{3+} and Mn^{4+} are ordered in stripes.

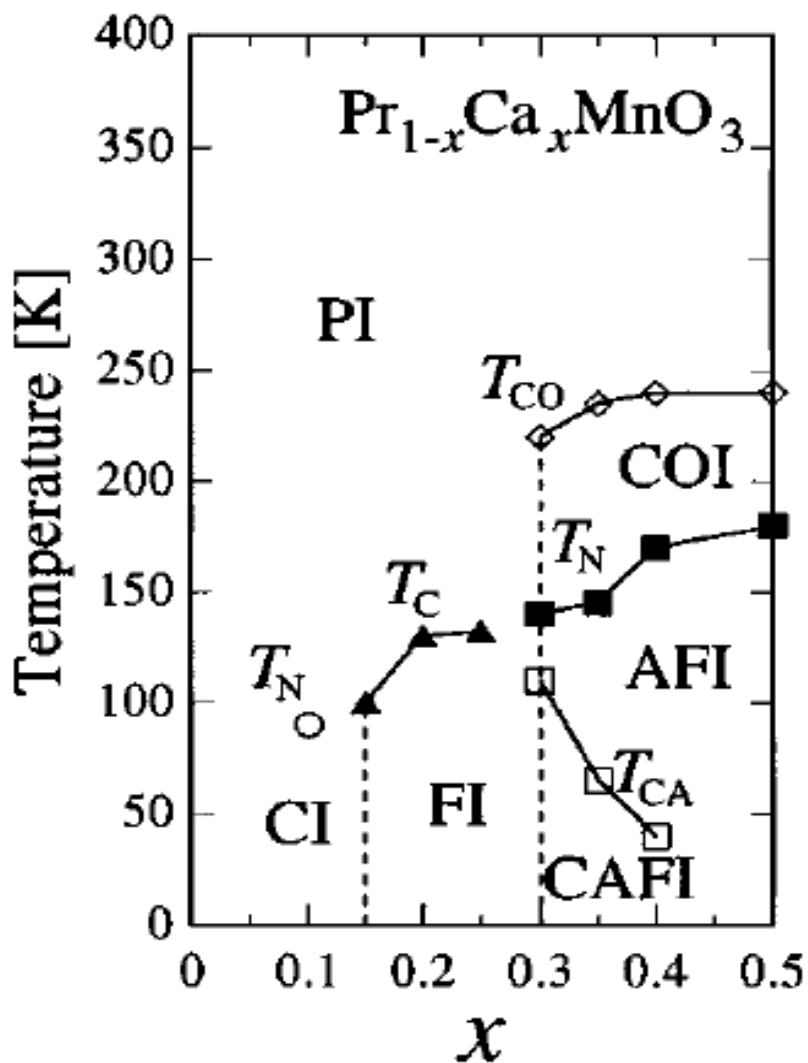


Figure 1-12: The phase diagram for $\text{Pr}_{1-x}\text{Ca}_x\text{MnO}_3$. COI, AFI, CAFI, FI and CI indicate charge ordered insulator, antiferromagnetic insulator, canted antiferromagnetic insulator, ferromagnetic insulator and canted insulator respectively. This shows that changing the A-site cation can result in a different phase for the same doping ratio of similarly doped manganites with different A-site cations [66].

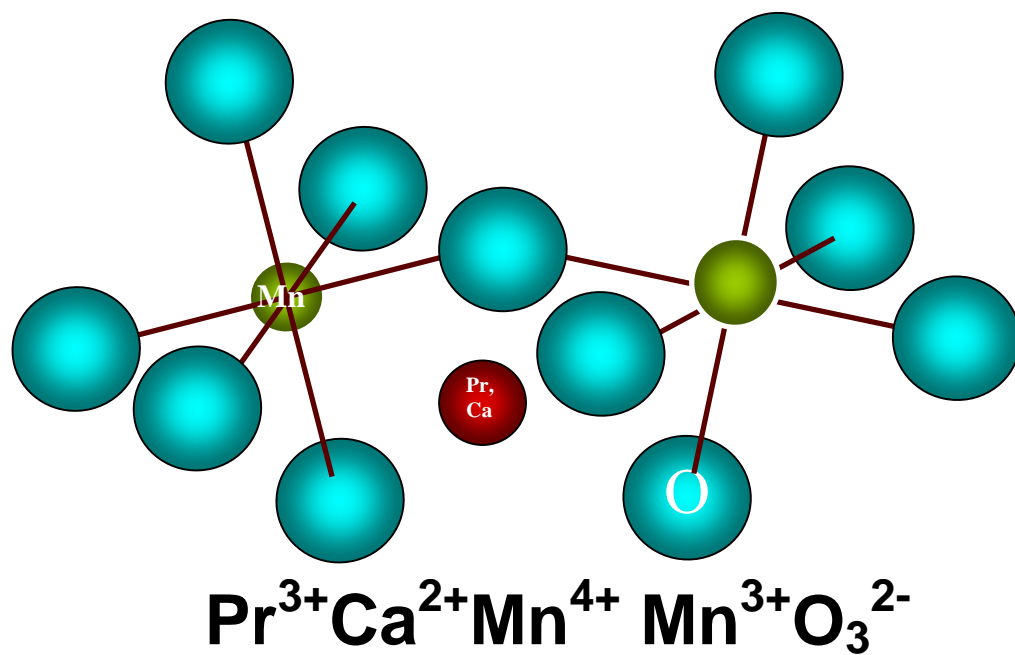


Figure 1-13: Schematic drawing for the Jahn Teller distorted PCMO due to the small size of the Pr ion.

CHAPTER 2 EXPERIMENTAL SETUP

2.1 Temperature Control System and Magnet

All of the measurements related to manganite in this thesis were done using ‘Blueman’, which is the nickname of the dewar (which includes a variable temperature insert, helium reservoir, American Magnet Institutes (AMI) superconducting magnet) in the Biswas lab. Therefore we start this chapter with a short guide on how to baby-sit Blueman. Four different experimental techniques will then be discussed.

2.1.1 Janis Superveritemp Insert with Dewar Description

The dewar consists of an outer vacuum jacket, a helium reservoir, and a Janis Superveritemp Insert inside the bore of the superconducting magnet. The variable temperature insert is composed of a sample tube and an isolation tube, which thermally isolates the sample tube from the outer helium reservoir. The sample probe used in each experiment will be located inside the sample tube. The helium from the reservoir can pass into the sample tube through a needle flow control valve and capillary tube. During this procedure, helium could be vaporized and heated by a heater, which is located at the bottom of sample tube. A Cernox CX-1050–SD sensor is in thermal contact with the capillary. Depending on the opening of needle valve, the heater can increase the vaporization rate or just increase the temperature of the helium vapor. By increasing the vaporization rate, we can increase the cooling speed of the sample when its temperature is greater than the temperature of liquid helium. We have an additional thermometer and heater for the sample for each probe and this is discussed in detail in the thermometry section.

2.1.2 Cooling Procedure

At room temperature, we evacuate the sample tube by mechanical pump until the pressure reaches around 140mtorr through the 3/8" vent port, which is marked in the figure 2-1 and then backfill with He gas. Second we evacuate the helium reservoir until it reaches 55 mTorr and backfill twice. After removing air and moisture using the previous procedure, the helium jacket is cooled down to 77 K by transferring liquid nitrogen (LN₂) to the reservoir until the resistance across the magnet drops to 18ohm. After finishing the transfer, LN₂ was left in the reservoir until the resistance decreases to 17 ohm (about 30 minutes), which indicates the magnet has reached 77 K. Next, we remove the LN₂ from the reservoir. It is important purge all LN₂ from the reservoir. For this we again evacuate the reservoir (down to 200 mTorr) and flush with He gas until we see the temperature start to increase. Once this is done we evacuate the sample tube and backfill with He gas. Then we transfer liquid He (LHe) to the He reservoir until the level reaches 25". The LHe loss rate is about 0.6 ~0.7 liters/hour and once the reservoir is full LHe will remain for approximately 2 and half days if no measurements are done.

2.1.3 AMI Superconducting Magnet

The magnet inside Blueman is a superconducting solenoid as shown in figure 2-1[80], which allows for fields up to 9 T. The magnet uses constant voltage to ramp up the current and hence the magnetic field. When the heater in the persistent switch is on so that the switch is off, current will pass only through the superconducting coil (A 9025-3). The constant voltage across the inductive coil will increase current in a constant rate ($V=LdI/dt$). This current will correspond to the magnetic field ($B=\mu I$). In case it is necessary to stay at one field for a long time, to reduce the LHe consumption due to heating and to save power, the magnet can be operated in persistent mode. By turning off the heater in the persistent switch, the switch will go into the superconducting state, and this leads to a closed current circuit composed of the magnet and the

superconductor inside the persistent switch, which allows the power to be turned off without affecting the magnet current (see figure 2-2). While the persistent heater was on, the field ramp rate was kept at 0.01 T/sec and for measurements in which the magnetic field was swept; the rate was kept at either 0.01 T/sec or 50 gauss/sec.

2.1.4 Thermometry

Our Point contact spectroscopy experiment was conducted at the National High Magnetic Field Lab (NHMFL) using their temperature control system. In this experiment, the system was set to 1.5 K by evaporative cooling, pumping the He4 at the rate suggested by the NHMFL. Due to the high magnetic fields used (upto33 T) the reading from the commercial thermometer loses its meaning at the low temperatures used. However, since the sample was immersed in superfluid He₄ it can be safely assumed that the temperature read at zero field is maintained in the high fields. A Lake Shore Model 332 Temperature Controller was used for the remaining 3 experiments, which were carried out in our lab at University of Florida. Three different kinds of temperature sensors were used. First a Cernox CX-1050-SD with 0.3 L calibration was used for the Needle valve sensor of the dewar. A Cernox CX-1030-SD with 1.4 L calibration was used for the Strain and Disorder experiment. A Silicon Diode DT-470-SD was used for the probe, which was used for all resistance measurements. The first two sensors are safe to use when $T > 2$ K and $B < 19$ T and so are well suited for our magnet, which has a maximum possible field of 9 T.

2.2 Point Contact Spectroscopy (PCS) and PCCO Overview

We have constructed a PCS probe for the 32 mm bore DC field magnets and have used it for measurements with fields up to 33 tesla and at temperatures down to 1.5 K. The first requirements were a probe design that would fit into the small space in the cryostat and the magnet bore, increase the resonance frequencies of the tip-sample approach mechanism, and improve the stability of the point-contact junction. Since cuprates are highly anisotropic

materials, tunneling and point contact spectra show a strong dependence on the direction of tunneling. For our experiments we need to tunnel into the a-b plane. At the same time, a magnetic field will be applied perpendicular to the a-b plane to magnify the effect of the magnetic field as a decoherence field. Such a configuration adds a further complication to our probe design because we now need to be able to move the tip with respect to the sample, perpendicular to the magnetic field. Such a configuration was achieved by using a bevel gear (Figure 2-3), which was used in the experiment at the NHMFL and a cantilever method (Figure 2-4), which was used in Blueman, to change the direction of rotation. The barrier strength (or junction resistance) Z is determined by the pressure of the tip on the sample (in the bevel gear methods) or by changing the pressure on the cantilever (cantilever method). For both cases, Z was finely controlled by rotating a worm gear (1:96 ratio) at the top of the probe. Experiments were performed at constant magnetic field, which reduced the eddy current heating in the brass or copper probes.

Specialized electronics and software for data acquisition are also essential for PCS. The PCS data needs to be presented as plots of dI/dV vs. V (I and V are the junction current and voltage respectively). dI/dV is approximately proportional to the DOS for low voltages (~ 20 mV). A digital voltmeter monitored the junction voltage as it was slowly ramped (20 mHz, 50 mV Peak to Peak) as a saw tooth wave by a function generator. One lock-in amplifier/detector supplied a sine wave that was used to modulate the junction voltage with Reference frequency ~ 960 HZ (see equation 2-1). That lock-in measured dI/dt through a resistor in series with the junction, while a second lock-in measured dV/dt across the junction (see figure 3-5).

$$V = V_0 + \delta V \sin \omega t$$

$$I(V) = I(V_0) + \left. \frac{\partial I}{\partial V} \right|_{V=V_0} \delta V \sin \omega t \quad (2-1)$$

The two lock-in signals and the junction voltage were recorded by the NHMFL Data Acquisition program [81], which calculated $dI/dV = (dI/dt)/(dV/dt)$ and plotted it against V .

A dI/dV vs. V curve for a point-contact junction between the n-doped cuprate $\text{Pr}_{2-x}\text{Ce}_x\text{CuO}_4$ (PCCO, $x = 0.15$) and a Pt-Rh wire taken at $T = 1.5$ K and $H = 0$ is shown in figure 2-6(a) [82]. The data clearly reveal the superconducting gap, and the value of the gap shows excellent agreement with the published data. Figure 2-6(b)[82] shows the PCS data at 1.5 K in a field of 31 T. The data show that the pseudogap exists even in a field of 31 T. Figure 2-6(c) [82] shows the variation of the point contact spectra from 0 T to 23 T. The PCS probe can be used for high field studies of the density of states of new superconducting systems such as heavy fermion systems. It can also be used to perform point contact Andreev reflection experiments on ferromagnetic materials using superconducting tip.

For this experiment optimally doped single crystals and thin films of electron doped PCCO were used (see figure 2-7). It has a T_c of around 22 K~ 25 K and a H_c 5~6 T at 4.2K 7~8 T at 1.5 K for the optimally doped case. The Ce doping range is 0~0.2 and the critical doping is 0.149. For the thin film, SrTiO_3 was used as the substrate

2.3 Low Field Magnetoresistance of Manganite Thin Film

For the study of low field ultra thin film (7.5 nm) of manganite $(\text{La}_{0.5}\text{Pr}_{0.5})_{0.67}\text{Ca}_{0.33}\text{MnO}_3$ was grown using pulsed laser deposition (PLD). And the resistance was measured 3 different ways. Temperature dependent resistance measurements without magnetic field and with a static magnetic field and at fixed temperatures and magnetoresistance with a slow magnetic field sweeping rate (100 gauss/sec or 50 gauss/sec) were obtained. .

2.3.1 Thin Film Growth

All manganite samples discussed in this thesis were grown using Pulsed Laser Deposition (PLD) techniques. An excimer laser of 248 nm wavelength with pre-mixed Kr and F gas was used

to make an ionized manganite plume from a rotating target. The parameters for the deposition were optimized to give the highest phase transition temperature. The thickness of the samples can be controlled by the deposition time and the laser firing frequency. However, every sample, which appears in this thesis was grown using the same frequency (5 Hz). This gives a growth rate of 30 nm / 8 min. NdGaO₃ (110) substrates were used for all manganite experiments due to the similarity of its lattice constant to that of bulk LPCMO. The in-plane lattice constants for NGO (110) are 0.3885 nm and 0.3864 nm and for LPCMO (at room temperature single phase) are approximately 0.384 nm for both directions. The substrates were sonicated with Acetone and then Ethanol until a clean surface could be seen and it was then mounted using silver paint (Leitsilber 200 from TED PELLA, INC Product No 16035) on the cleaned surface of our heater. Before we insert the heater into the chamber we heat the sample up to 100°C to dry the silver paint. After the heater is placed in the deposition chamber, shown in figure 3-8, the chamber was pumped down using a turbo pump, with a mechanical back up pump, until the pressure reaches 5×10^{-6} mTorr. Once it reaches the desired pressure, we start to increase the temperature to 820°C. When the temperature reached 300°C, oxygen was introduced to prevent the loss of oxygen from the substrate and to provide ambient oxygen pressure during deposition. The Oxygen pressure was maintained around 440 mTorr. At 820°C we deposited the film from a plume produced from a 5-minute pre-ablated polycrystalline target. The Laser power was set to be a constant approximately 480 mJ. Later it was found that higher power ~500 mJ gives smoother surfaces so for some experiments which required a smoother surface, the film was deposited with this power. After growth oxygen was controlled in a post annealing process until the temperature decreased to approximately 300°C with a cooling rate of 20°C/ min.

2.3.2 Experimental Setup for Transport Measurements

Due to its high resistance ($10^6 \sim 10^{12}$ ohm), an indirect method was used to measure the sample resistance (See figure 2-9). In this way the sample resistance R_s can be obtained by measuring V_L (See equation 2-2). Since the sample has extremely high resistance we can ignore the effect of contact resistance on the result. Specific values of the bias voltage and Load resistance for each measurement were marked on the graph with results shown in chapter 4.

$$R_s = (V_{\text{Source}} - V_L) / (V_L / R_L) \quad (2-2)$$

2.4 Microfabricated Double Layer Structure

To study the transportation properties in the direction perpendicular to the thin film of LPCMO, we fabricated a proper structure as suggested in figure 2-10. This structure could also be used to study the dielectric properties of the phase-separated state of LPCMO.

2.4.1 Fabrication of Structure

Figure 2-10 shows the structure, which we used for this experiment. First a 60 nm LCMO film was grown on top of a NGO substrate. And then a 26.5 nm LPCMO film was grown on top of the LCMO film. Micrometer thick gold contact pads were deposited on top of it. These gold contact pads act as an etching mask while etching. Two different types of etching were tried which were chemical etching and Ar ion (which is not reactive) etching using the Unaxis Shuttlelock RIE/ICP (Reactive Ion Etcher with Inductively Coupled Plasma Module). Chemical etching is superior in the sense that it leaves a more uniform surface after etching is done. However the etching rate during chemical etching was not consistent. It has a strong dependence on the size of the films and the age of the etching solution and it is difficult to control the etching time even though the sample was taken out of the solution and rinsed with deionized (DI) water it may not enough to stop the etching process thoroughly right away. Therefore for this experiment in which etching needs to be stopped at certain depth Ar ion etching was more

dependable. Figure 2-11 shows the schematic drawing for the common RIE/ICP module. The ICP (Inductively Coupled Plasma) power, which is proportional to Plasma density, was kept at 600 W and the table power (RF bias power), which is proportional to the ion energy, was kept at 100 W. The Ar pressure was 5mtorr and the flow rate was 20 sccm. The sample was mounted on top of a silicon wafer and the backside of the wafer was cooled by He gas of flow rate 10 sccm. To achieve a uniform surface after etching, etching was done 3 separate times with etching times of 30 sec, 35 sec and 35 sec. Each time the sample was remounted.

2.4.2 Experimental Setup for Capacitance Measurement

Using the merits of our structure the Complex Impedance of the sample was measured using 2 Lockin amplifiers (see figure 2-12). The modulus of the sample impedance can be obtained by measuring the complex current passing through the series resistance and the complex voltage across the sample, $|Z_s|=|V_s| / |I_s|$. The corresponding phase can be calculated using equation 2-3.

$$\text{Phase} = \tan^{-1} (V_i/V_r) - \tan^{-1}(v_i/v_r) \quad (2-3)$$

V_i and V_r indicate the imaginary part and real part of the voltage for the sample and v_i and v_r indicate the imaginary part and real part of voltage for the load resistance respectively.

2.5 Strain and Disorder Effect on Manganite Thin Films

For the strain and disorder effect on manganite thin films three different compounds of LPCMO 30nm thick films were used. They are $(La_{0.6}Pr_{0.4})_{0.67}Ca_{0.33}MnO_3$, $(La_{0.5}Pr_{0.5})_{0.67}Ca_{0.33}MnO_3$ and $(La_{0.4}Pr_{0.6})_{0.67}Ca_{0.33}MnO_3$. First we measured the temperature dependent resistance for all of them and we applied tensile strain along the in plane direction of those films and measured R vs. T again. The strain probe used is the same as the PCS probe shown in figure 2-4 with a modification shown in figure 2-13. This modification was made by undergraduate student Jacob Tosado.

After that we applied external disorder to these films with the help of Rajiv Misra (graduate student, Hebard group), by bombarding them with Ar ions using SHIVA (sample handling in vacuum). SHIVA can be used to conduct an extremely well controlled ion milling process and allows for the monitoring of the resistance of the film in-situ while the milling is proceeding. The disorder was applied within a limit, which does not change the thickness of the films. The resistances of the films, while applying disorder, were carefully observed for this purpose. The parameters used for applying disorder were Cathode current 6.7 A, Discharge voltage 40 V, Beam Current 7 mA Beam Voltage 200 V and Accelerating Voltage 45 V. The sample was exposed over three separate intervals of time 30 sec, 20 sec and 10 sec. R vs. T for each disordered sample was measured again. After the same amount of strain (5.6×10^{-4}) as in the non-disordered case was applied to each disordered sample and R vs. T was measured and compared. For the $(La_{0.5}Pr_{0.5})_{0.67}Ca_{0.33}MnO_3$ sample both resistance measurement techniques, which are the regular 4 probe method with a current source and a voltage source with a load resistance shown in figure 2-7 were used and compared. For the other compounds the latter method was used.

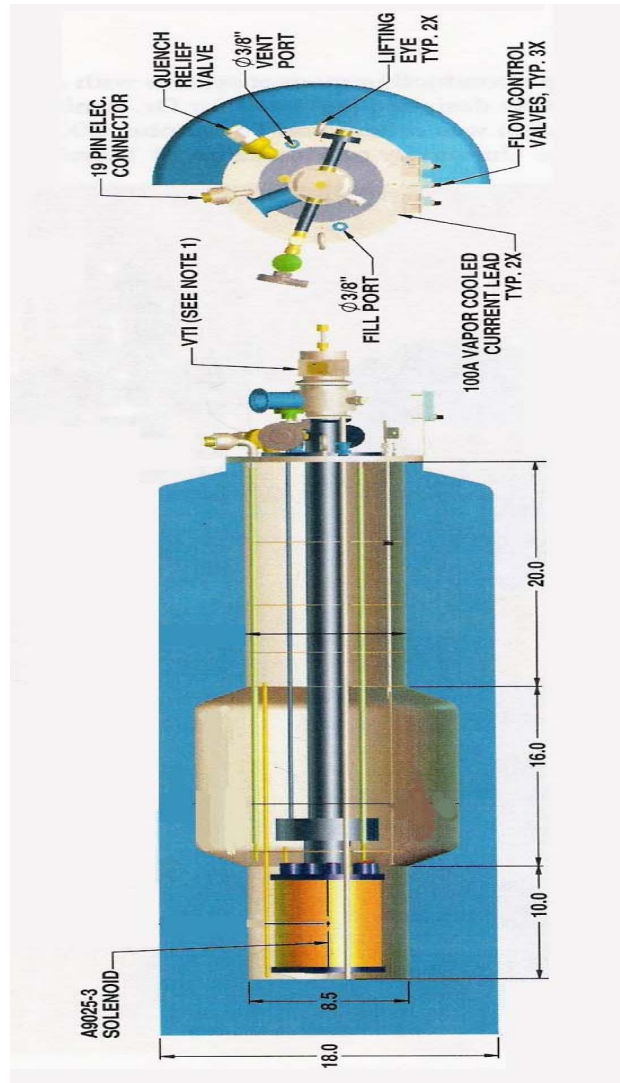


Figure 2-1: Drawings of the Blueman, which includes, helium reservoir, Janis varitemp insert and AMI superconducting magnet. This drawing is presented courtesy of American Magnet Institute (AMI) [80].

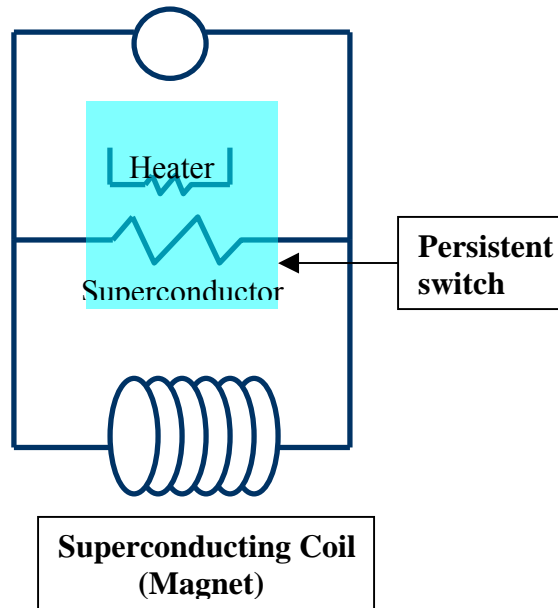


Figure 2-2: Superconducting magnet.

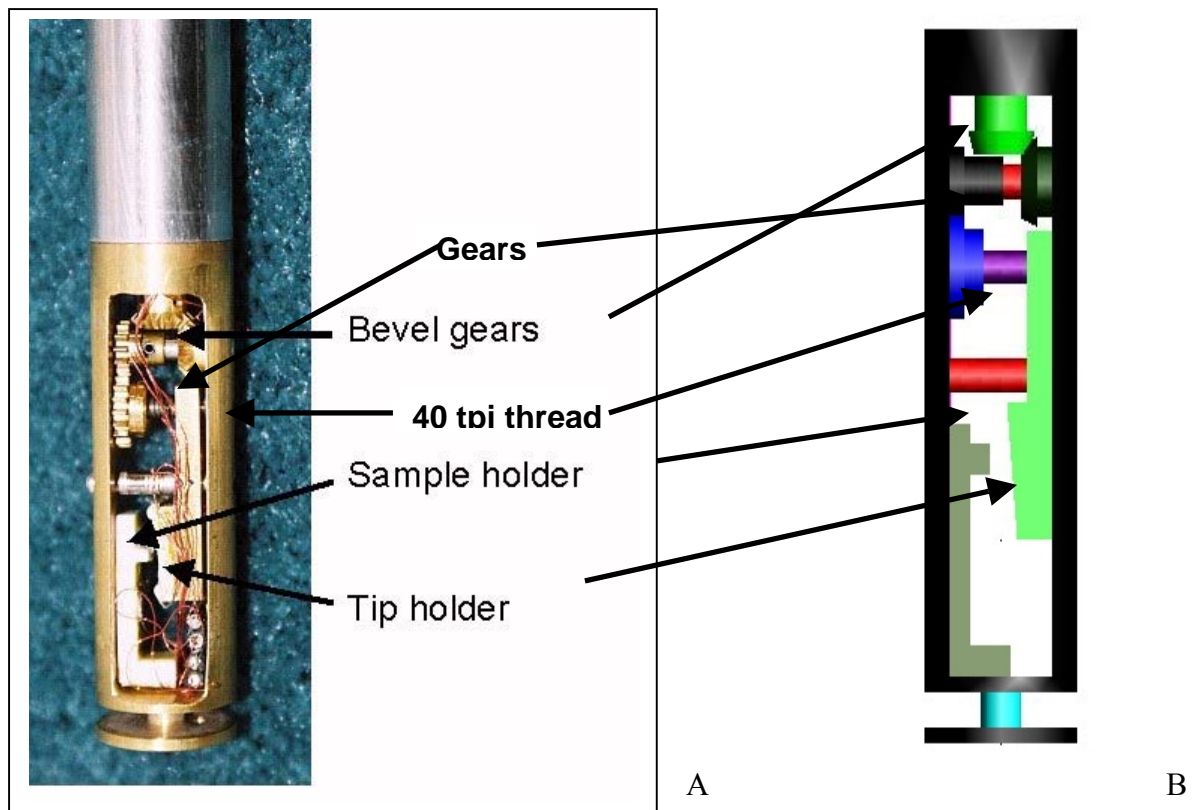


Figure 2-3: PCS design using bevel gears as a mechanical approaching system. (a) A photograph is shown.(b) Its schematic drawing is shown [82].

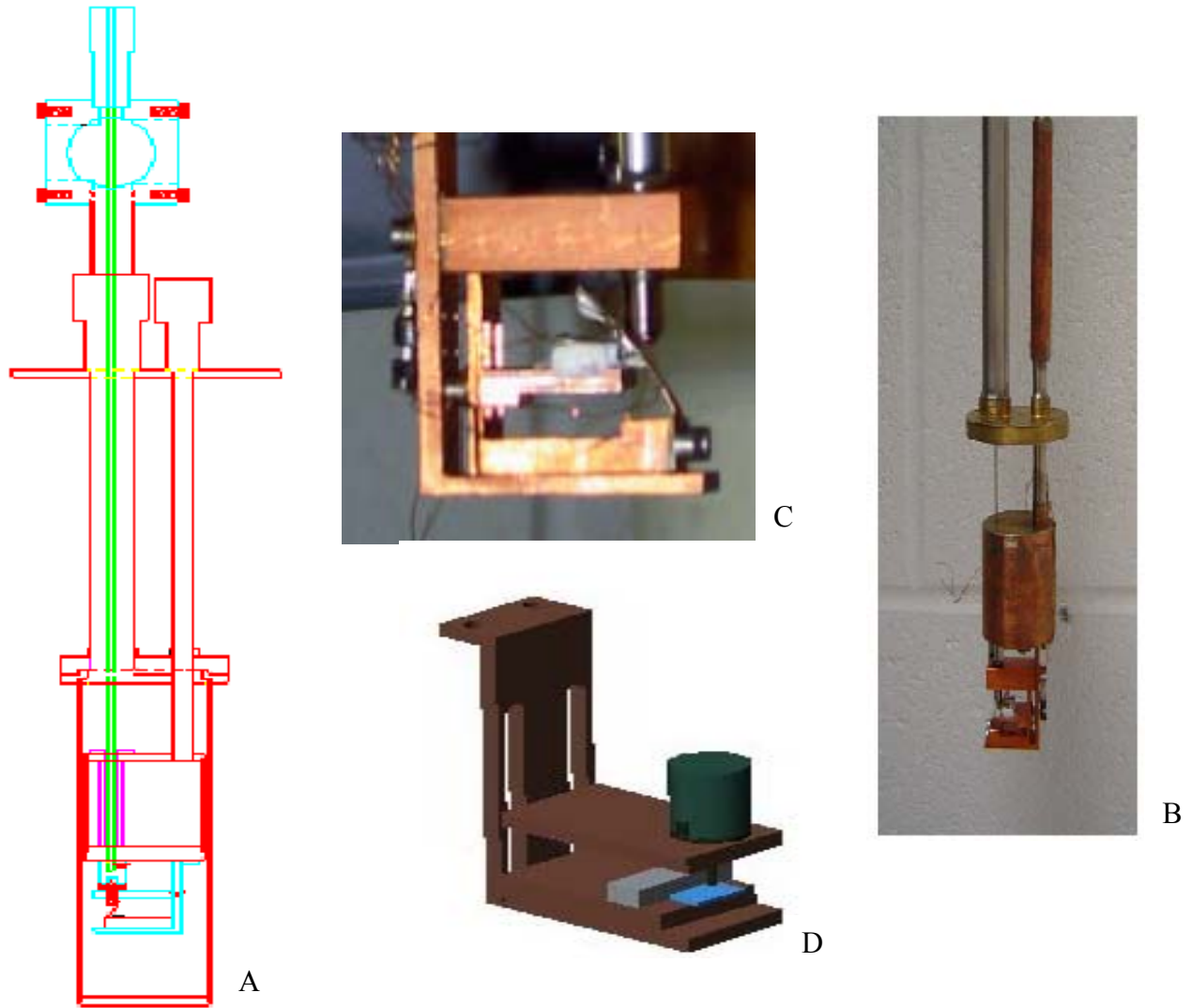


Figure 2-4: Probe for PCS and strain measurements for manganite and details of mechanical approaching system. (a) A schematic diagram of PCS probe. (b) A photo of PCS probe. (c) A photo of mechanical approaching system using a cantilever for PCS. (d) 3dimensional drawing of mechanical approaching system.

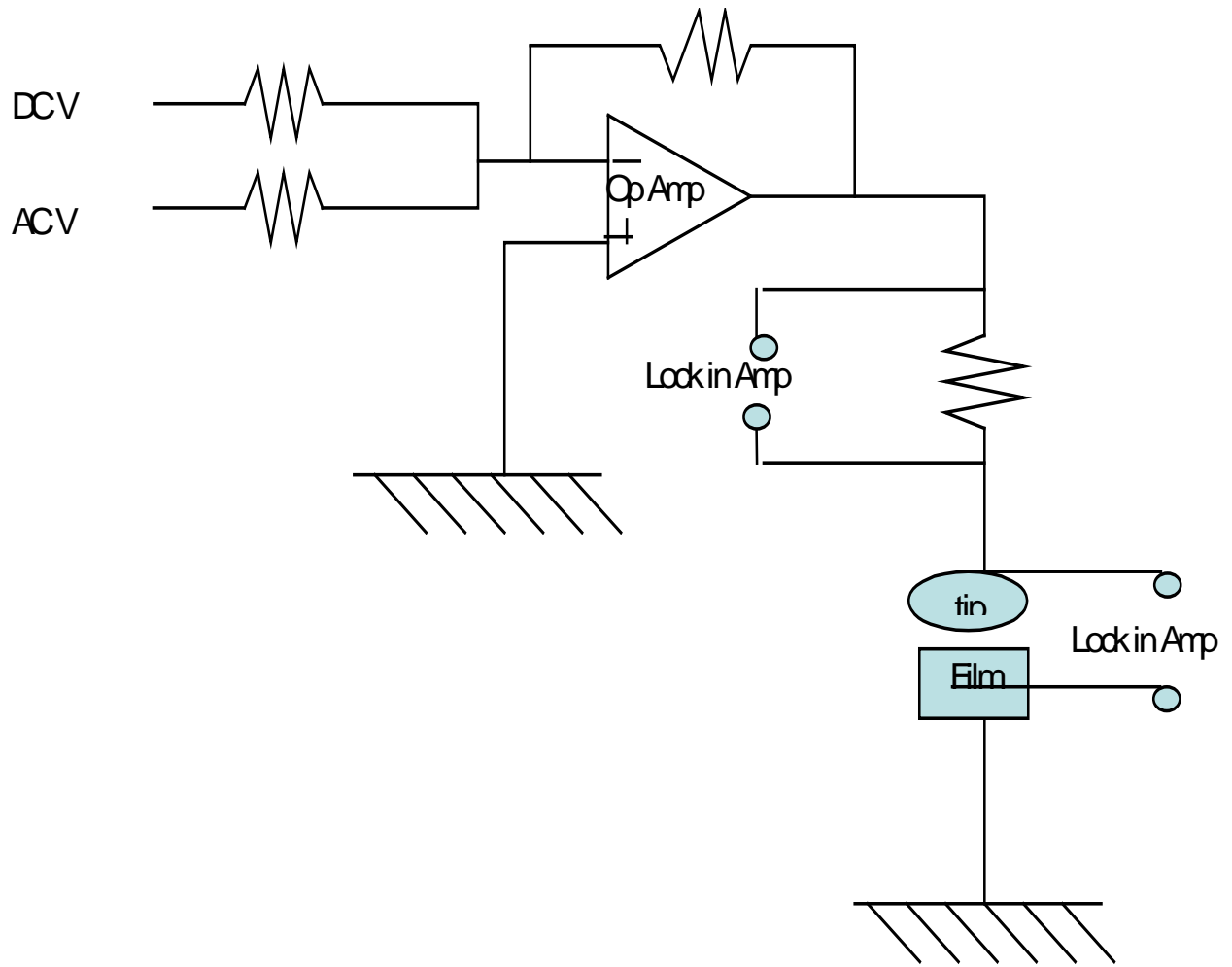


Figure 2-5: Circuit diagram for point contact spectroscopy

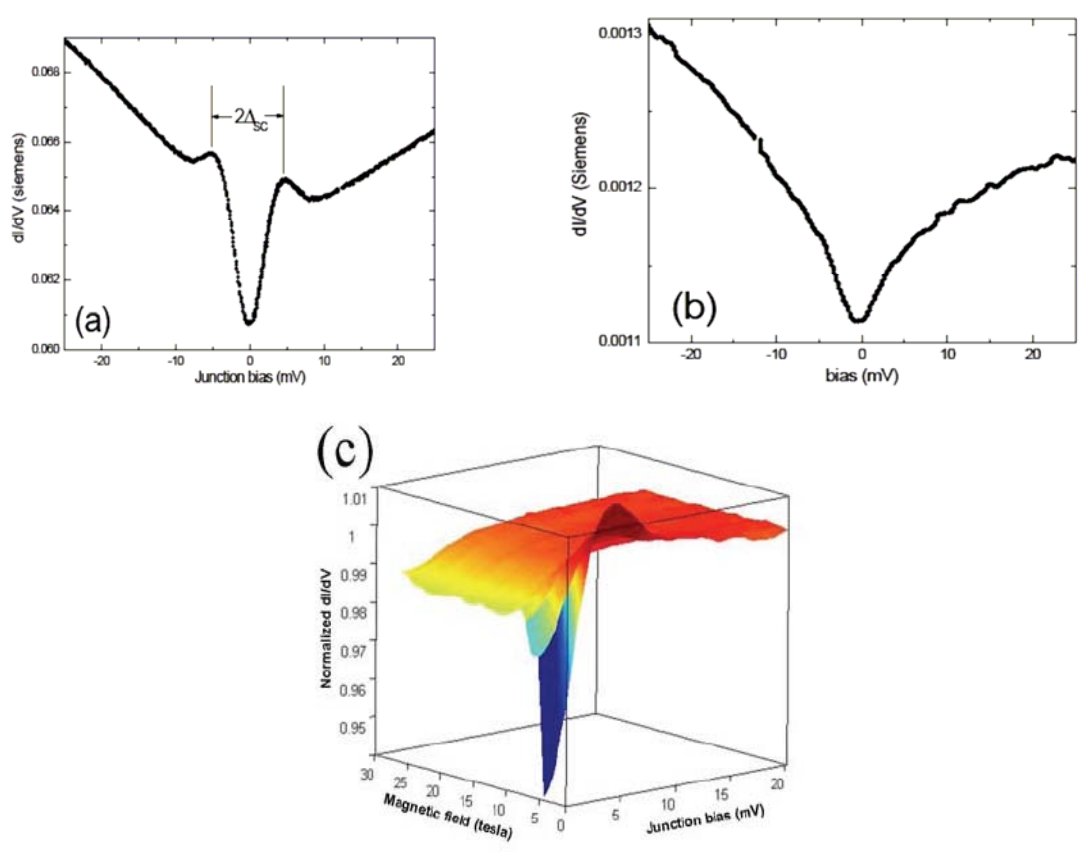


Figure 2-6: Point contact spectra of a junction between PCCO and a Pt-Rh tip taken at 1.5 K in a field of (a) 0 T and (b) 31 T. (c) Evolution of the point contact spectra with magnetic field [82].

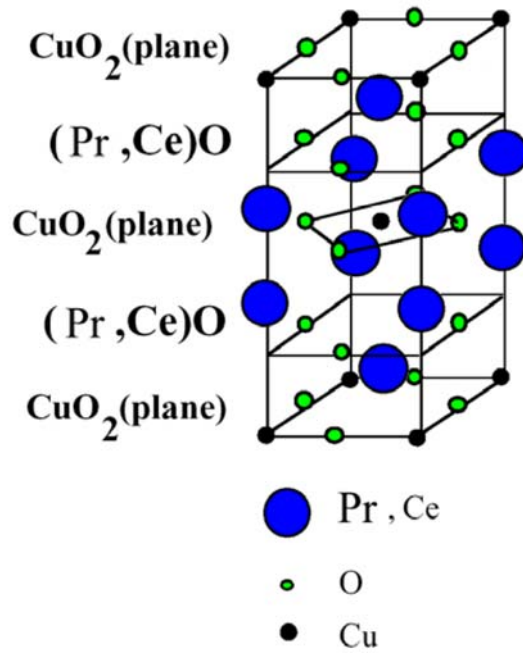


Figure 2-7: Electron doped cuprates PCCO

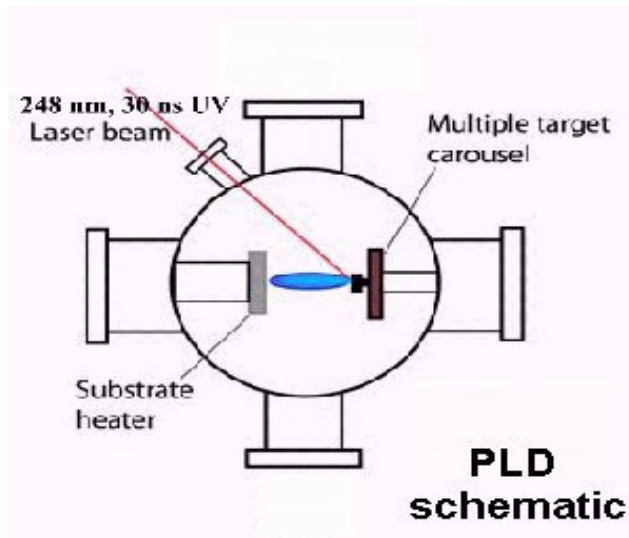


Figure 2-8: Pulsed laser deposition chamber

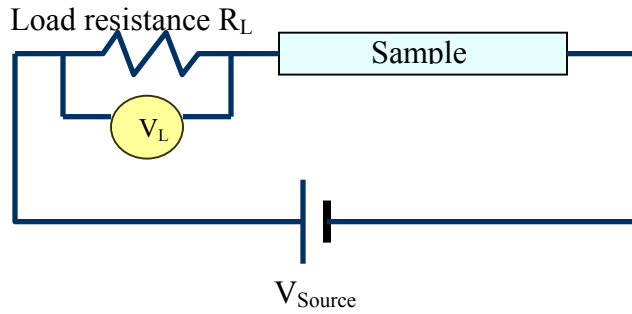


Figure 2-9: Circuit for the measurement of a Sample with High Resistance

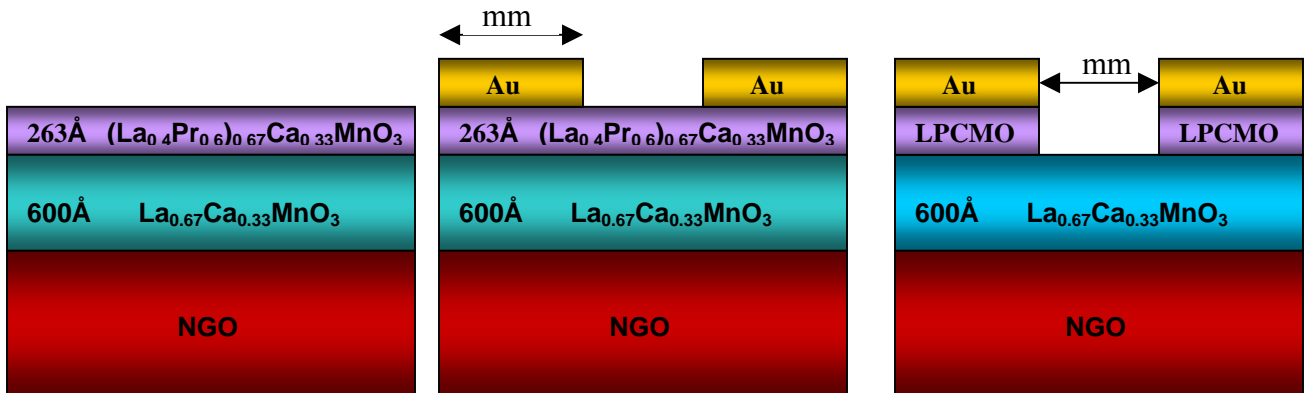


Figure 2-10: Process by which the structure, used to measure transport properties in the direction perpendicular to the manganite LPCMO thin film, was formed.

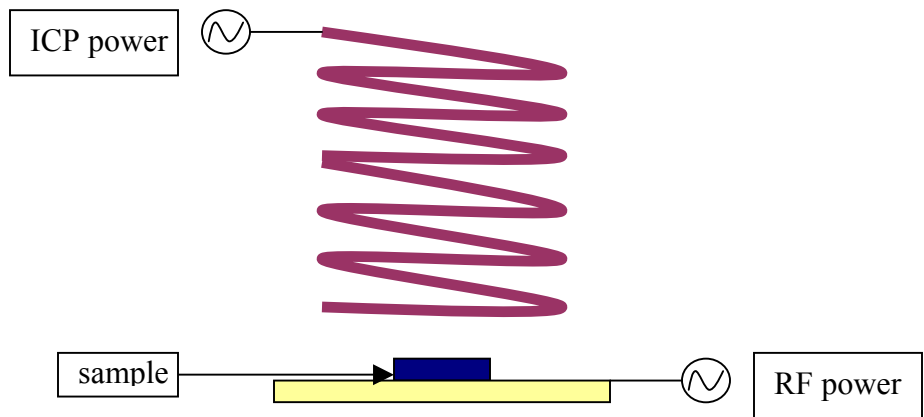


Figure 2-11: RIE/ICP (Reactive Ion Etcher with Inductively Coupled Plasma Module)

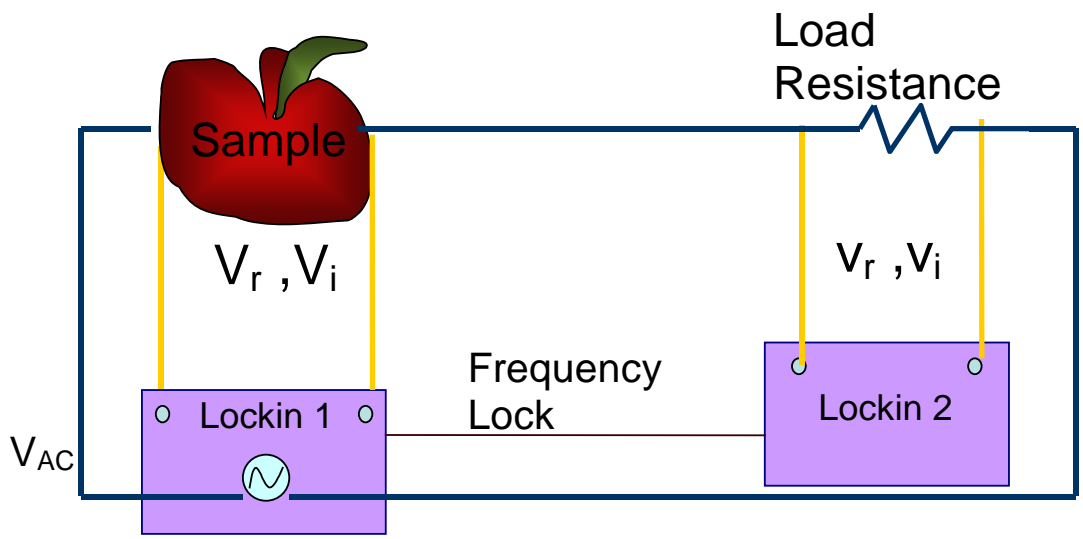


Figure 2-12: Two Lock-In Amplifier Methods for the Impedance measurement of the sample.

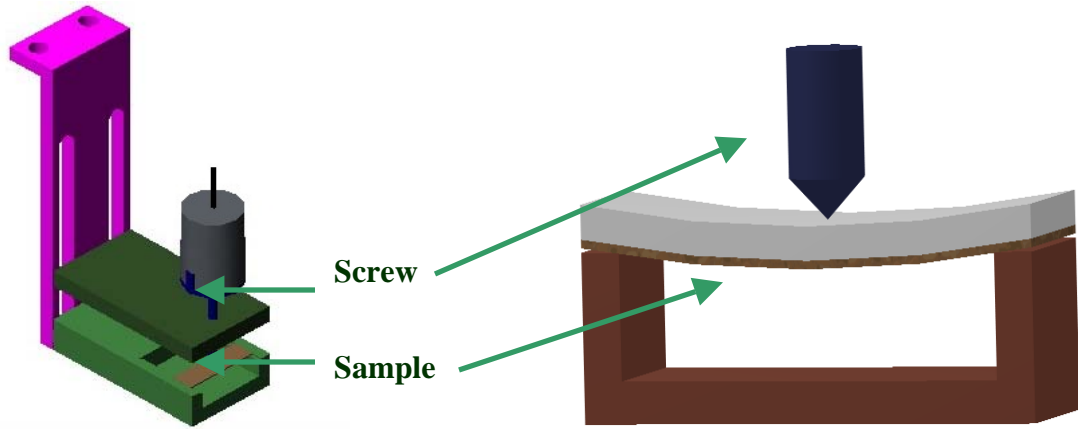


Figure 2-13: Sample holder in which strain is applied using a 3 point beam balance technique.

CHAPTER 3
POINT CONTACT SPECTROSCOPY ON ELECTRON DOPED CUPRATES

3.1 Pseudogap Research on Electron Doped Cuprate PCCO Overview

A detailed experimental and theoretical status of the pseudogap phenomenon in hole and electron-doped cuprates was given in chapter 1. It is clear that when compared to studies done on the pseudogap in hole-doped cuprates, studies on electron-doped cuprates have received relatively little attention [26]. However, the fact that the electron doped cuprates have much lower critical fields (~ 10 T) at low temperatures) than their hole-doped counterparts (~ 100 T) allows us to study the normal state in the region, inside the superconducting dome at 0 T, which was not possible for the hole-doped cuprates. This information is expected to shed light on the nature of the normal state in this compound. Even though the superconducting gaps from both n-doped and p-doped compounds show a similar dependence on doping [83, 40, 37], it is not possible to conclude that the superconducting state has the same origin for the following reasons. First, it does not have a phase fluctuation region above T_c like the one in the hole-doped case as observed by Nernst effect measurements [58]. Second, the pseudogaps of the electron-doped compounds have 2 different energy scales as observed from different measurements. Tunneling type measurements (tunneling across the grain boundary and point-contact spectroscopy) in the normal state in the region, inside the superconducting dome at 0 T of the electron-doped cuprates show a smaller gap (~ 10 -20 meV), which is comparable to the scale of its own superconducting gap [40, 34, 36]. However angle-resolved photoemission spectroscopy and optical reflectivity measurements reveal a gap which is an order of magnitude larger (~ 100 -200 meV) [31, 85] and which is of a similar scale to the gap in hole-doped cuprates. Third, if the normal state gap¹ of

¹ The low energy gap for the electron-doped compound and the high energy gap for the hole-doped compounds were considered

the electron doped compound observed in tunneling type measurements had the same origin as the pseudogap in the hole-doped compound, it is suggested that it would exist inside the superconducting dome and vanish as the doping increases and approaches its optimum value [3]. On the contrary, the experimental results from tunneling measurements on the electron-doped cuprate PCCO show that the normal state gap exists even in the over doped regime [38]. Furthermore, this experiment also suggests the possibility of a strong relation between this normal state gap and superconductivity, since the normal state gap closing temperature is very close to the superconducting T_c .

Hence, the importance of the normal state behavior of electron-doped cuprates inside the superconducting dome for the profound understanding of the origin of the normal state gap is clear. Previously, the pseudogap in n-doped cuprates was measured by interlayer tunneling transport in the compound $\text{Sm}_{1-x}\text{Ce}_x\text{CuO}_4$, and it was shown that the normal state gap in both n-doped and p-doped cuprates originated from the spin-singlet, which is formed above T_c [33, 86]. In this thesis we report the first point contact spectroscopy measurements of the normal state inside the superconducting dome (in magnetic fields up to 31 T) on optimally doped PCCO single crystals for a complementary understanding of the origin of the normal state gap.

3.2 Field Dependent Normal State Gap from PCS

Four different sets of magnetic field dependent point contact spectra (differential conductance vs. applied bias voltage) are shown in Figure 3-1, 3-2, 3-3 and 3-4. The different sets indicate different junction resistances, which are named junction A, B, C and D, for the same single crystal of PCCO. Junction A, B and C show the result starting from the low field. Junction D includes only the high field data, which resulted from failing to keep the previous junction as the magnetic field is increased above 28 T from the Junction C experiment, however the Junction D result is consistent in that high field range. All point contact spectra shown in this thesis were

taken at T=1.5 K. In each low field spectrum, the coherence peaks, which are the signature of the superconducting gap, were clearly observed. The value of the superconducting gap is about 10 meV.

3.3 Analysis of Normal State Gap

As the magnetic field is increased above H_{c2} , the resistance of the junction increases due to the increase of the resistance of the sample, which results in a vertical shift of the G-V curves when the applied field is higher than H_{c2} . (For the cases of junctions A and C, there is a big shift between zero field and the next higher field due to an unexpected modification of the junction in an applied field. Since such a change does not affect our data analysis, the zero field data has been included). This shift has to be removed to isolate the field dependence of just the junction by removing the field-induced resistance of the crystal for each field and adjusting the sample voltage accordingly. The resistance of the crystal R_{crys} , in the point contact junction in a magnetic field H can be obtained from comparing the conductance of the region outside the gap in the following way, $R_{crys} = G^{-1}_{at\ field} - G^{-1}_{at\ 0T}$. The corresponding junction bias will be $V_j = V_{meas} - I_j \times R_{crys}$, where V_{meas} is the measured junction bias and I_j is the junction current which can be obtained by $V_{meas} \times G_{at\ filed}$. Figure 3-5 shows an example of this adjustment for the junction B. For further analysis only the negative bias data was chosen for convenience and adjusted with the technique shown above for each junction and those results are shown in Figures 3-6(a), (b) and (c).

The asymmetric (in the sense that the left and right side of the gap are not exactly the same) linear background seen outside the region of the superconducting gap, which is also found in other scanning tunneling experiments on cuprates [87, 88], can be explained within the Gutzwiller-Resonating Valence Bond theory or by multiple inelastic scatterings through the

tunneling barrier [89]. In either case, this linear background needs to be removed to understand the effect of the magnetic field on the normal state gap. This linear background could be subtracted based on the method by Shan *et. al* [90] by taking the linear fit of the region outside the gap and dividing each field dependent conductance curve by that linear function. The results for each junction are shown in Figure 3-7 through 3-9. For clarity, in some junctions, high field and low field results are shown separately. The normal state gap appearing as a suppression of the density of states below the Fermi level in the normal state of PCCO, becomes clearly visible even for the highest fields for each junction. Unfortunately, as mentioned before, the highest field result, the junction D case, was obtained as a separate result without any lower field result, still we can see the clear suppression of the density of states below the Fermi level.

It is not easy to quantify the magnetic field dependence on the width of the normal state gap. However, a 2D plot of the result can make it more obvious. Figure 3-10(a), (b) and (c) are the 2D plots of those results and we can see from those plots that the normal state gap (which appears as a darker region in each plot) is not affected much by the magnetic field for any junction and it persists even for the highest field for each junction. A more careful observation of these 2D plots shows a slight reduction in the normal state gap starts around 20 T.

3.4 Disorder Effect and Normal State Gap

The fact that the normal state gap is not suppressed even at 31 T casts doubt on the possibility that this normal state gap is the pseudogap. If this normal state gap were the pseudogap suggested by the tunneling experiment for the region inside the superconducting dome of the electron doped cuprate $\text{Sm}_{1-x}\text{Ce}_x\text{CuO}_4$, this pseudogap closing field H_{pg} and pseudogap closing temperature (T^*) should be related through the Zeeman equation [33, 86]

$$k_B T^* = g \mu_B H_{pg} .$$

Since the pseudogap closing temperature for the optimally doped PCCO is ~ 38 K, in this case, the H_{pg} should be ~ 28 T. This contradiction to our result suggests two possibilities. Either the theory that the preformed spin singlet is the origin of the pseudogap was not correct or the normal state gap found in the electron-doped cuprate is not the pseudogap (i.e. it is another type of order parameter which is not directly related to superconductivity).

The plot of the field dependence of the zero bias normalized conductance, G_0 which is shown in figure 3-11, allows us to see the putative pseudogap closing field by extrapolating the result (basically by increasing the field value until we come across $G_0=1$). From the linear extrapolation of the junction C case (shown as a red dotted line in figure 3-11(c)), which has the most extended range of fields, $H_{pg} \sim 90$ T could be obtained. The relative energy to this is ~ 10 meV ($E = g\mu_B H_{pg}$) and this is close to the observed width of the normal state gap (NSG) or superconducting gap.

This correspondence of the energy scale is similar to the magnetic field dependence of the zero bias anomaly (ZBA), which originates from the electron-electron interactions in disordered metals [91] ZBA can be represented as the following relation in 3-D.

$$n(E) = n(0)(1 + \sqrt{E/\Delta}), \quad (3-1)$$

where Δ indicates the correlation gap. Al'tshuler and Aronov have theoretically shown that in a magnetic field H a correlation gap feature should appear at energy $E = \pm g\mu_B H$ [128]. However, these features are broadened by temperature, spin scattering of conduction electrons and the electron-electron interaction. Hence, the overall effect of a magnetic field is expected to be a smearing of the correlation gap with the gap disappearing when $g\mu_B H_{applied}$ is similar to the width of the conduction gap. Figure 3-12 shows one example of this fitting and the slope is inversely proportional to the correlation gap. This nice fit of the relation strongly suggests the possibility

that the origin of this gap can be the electron-electron correlation. Considering that the ZBA or the correlation gap is observed only in these materials following $\ln(T)$ conductivity, the existence of the NSG in overdoped PCCO, which shows metallic conductivity[38] is unexpected. However, the possibility that the NSG is purely a surface phenomenon should be considered. Since the NSG has been observed only in surface sensitive measurements [92] like scanning tunneling spectroscopy and point contact experiments [3, 35, 34, 36] and properties of the surface and bulk of cuprates can be different from each other [93, 94]. Figure 3-13 shows the field dependence of the slope obtained from the correlation gap fitting. The Slope of the graph for fields lower than H_{c2} is not meaningful by itself because it is well known that this is from the superconducting gap and not from the correlation gap or any other kind of gap. These results show that the normal state gap, even when it is interpreted as a correlation gap, is not affected by magnetic field, which is consistent with all of our other analysis.

3.5 Summary

The density of states near the Fermi level in the normal state of the electron-doped cuprate PCCO single crystal was studied using point contact spectroscopy. This normal state gap persists even in the highest applied magnetic field (31 T) and it has weak magnetic field dependence. This result can be interpreted and summarized in the following way. First, if the NSG is the pseudogap then the pseudogap closing field is higher (by about a factor of 3) than expected from a pure Zeeman relation between the pseudogap closing temperature and the pseudogap closing field, which is expected if the origin of pseudogap are preformed spin singlets. Therefore, preformed pairing above T_c may not be the origin of the pseudogap [33, 86]. A second possible explanation is that the NSG observed in electron-doped cuprates is formed due to electron-electron interactions at the surface of n -doped cuprates, which is not related to either the pseudogap phenomenon in p -doped cuprates or superconductivity itself.

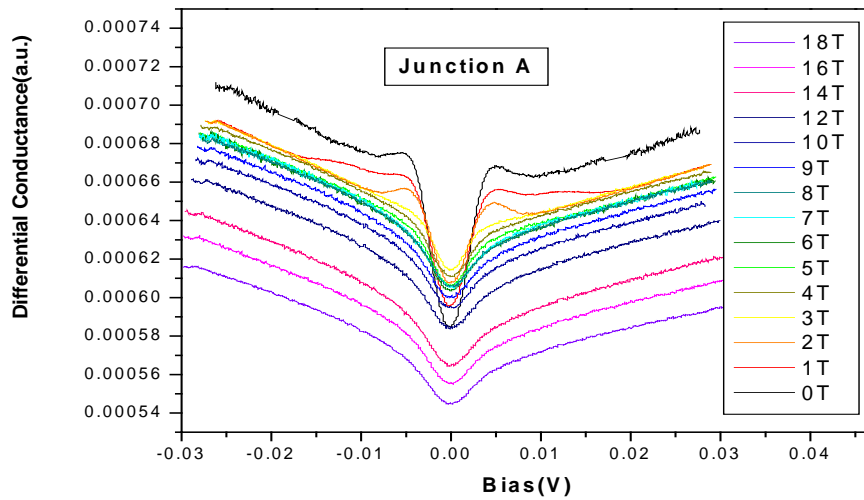


Figure 3-1: Differential conductance (dI/dV) vs. Bias voltage curves from the point contact spectroscopy result for junction A with magnetic fields of 0 T to 18 T. The superconducting gap marked here is about (10 meV)

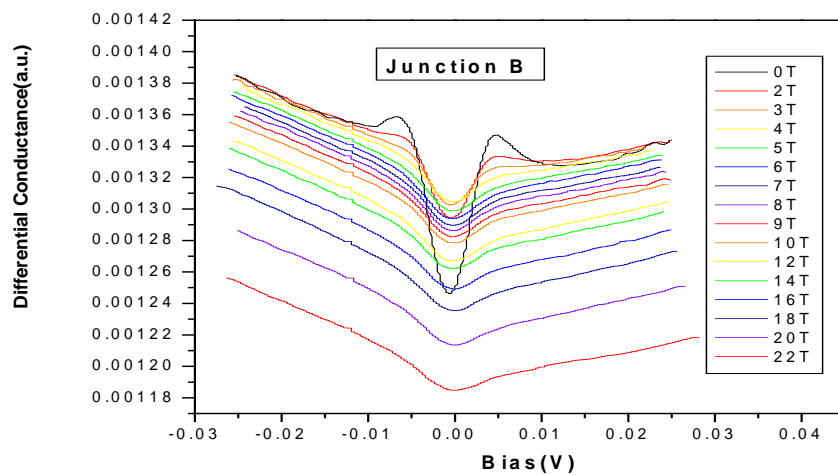


Figure 3-2: Point Contact spectroscopy result for junction B with magnetic fields from 0 T to 22 T.

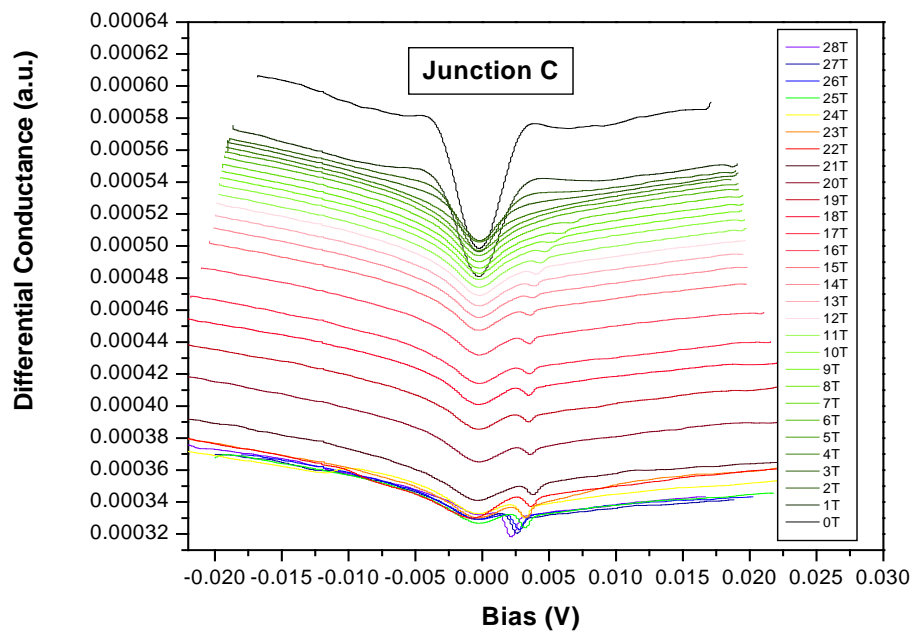


Figure 3-3: Point Contact spectroscopy result for junction C from 0 T to 28 T.

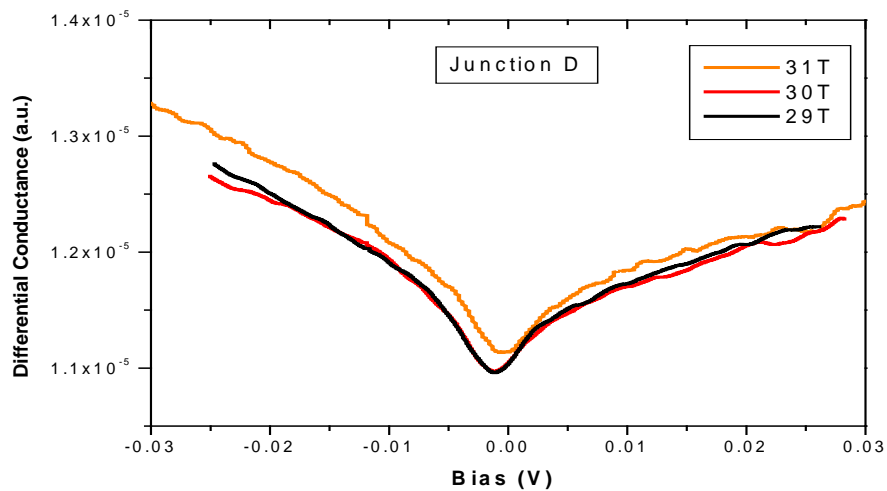


Figure 3-4: Point Contact Spectroscopy result of high magnetic fields using junction D

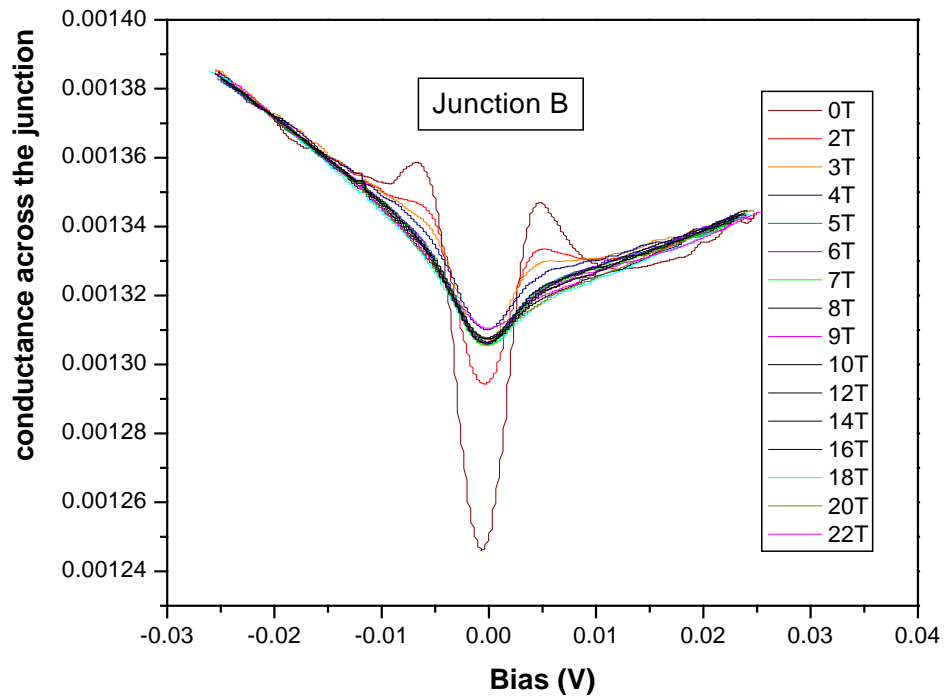


Figure 3-5: For the Junction B case, field dependent conductances across the junction only, after subtracting corresponding sample resistances at each field.

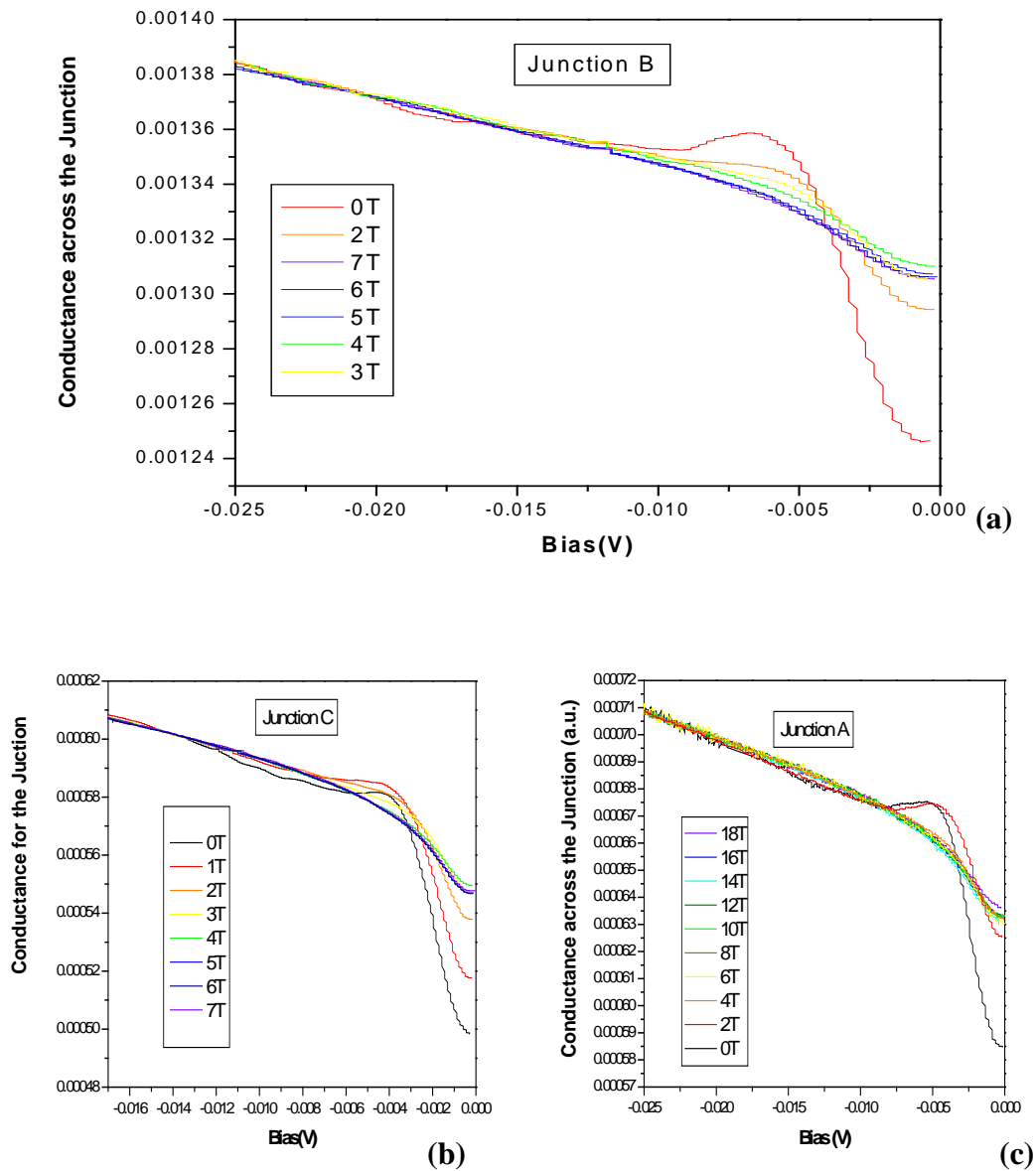


Figure 3-6: Detailed view of the conductance across the junction after subtracting the corresponding sample resistances at each field in the negative bias voltage regime. (a) Low fields dependent conductances across the junction B. (b) Low field dependent conductances across the junction C. (c) Field dependent conductances across the junction A.

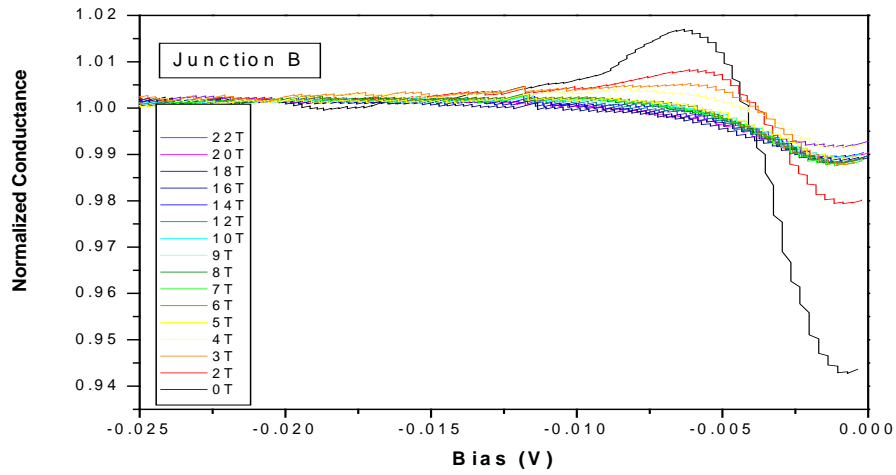


Figure 3-7: Normalized Conductance for the junction B case after getting rid of the linear background conductance from the result of figure 3-6(a).

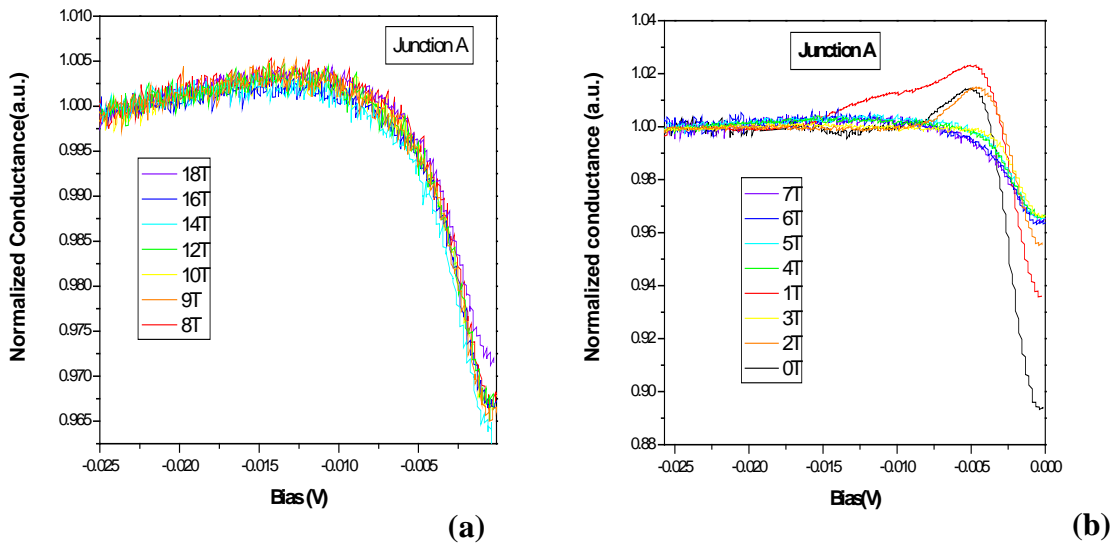


Figure 3-8: Normalized conductance for the junction A case after getting rid of the linear background conductance from the result of figure 3-6(b). (a) Low fields (0 T to 7 T) normalized conductance. (b) High fields (8 T to 18 T) normalized conductance.

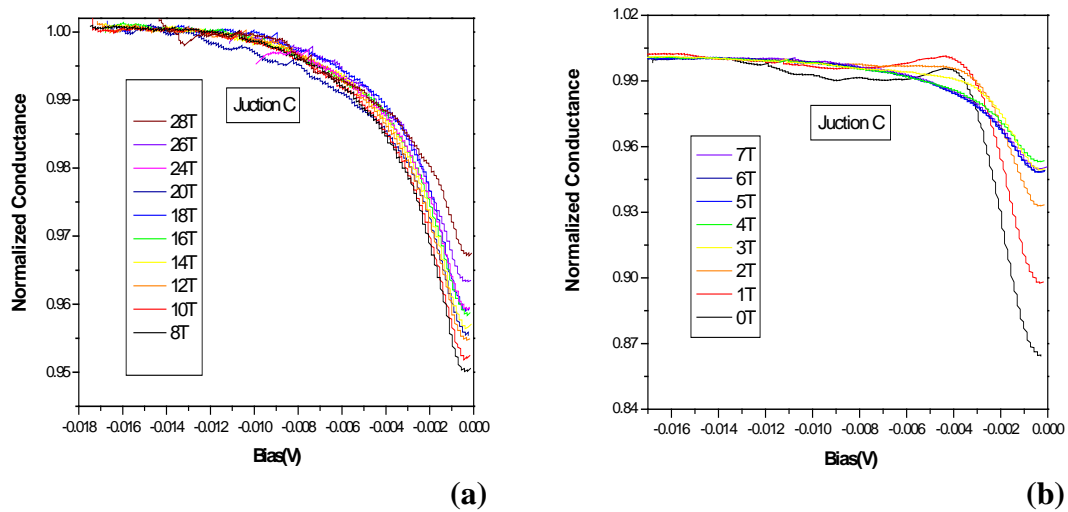


Figure 3-9: Normalized conductance for the junction C case after getting rid of the linear background conductance from the result of figure 3-6(c). (a) Low fields (0 T to 7 T) normalized conductance. (b) High fields (8 T to 28 T) normalized conductance.

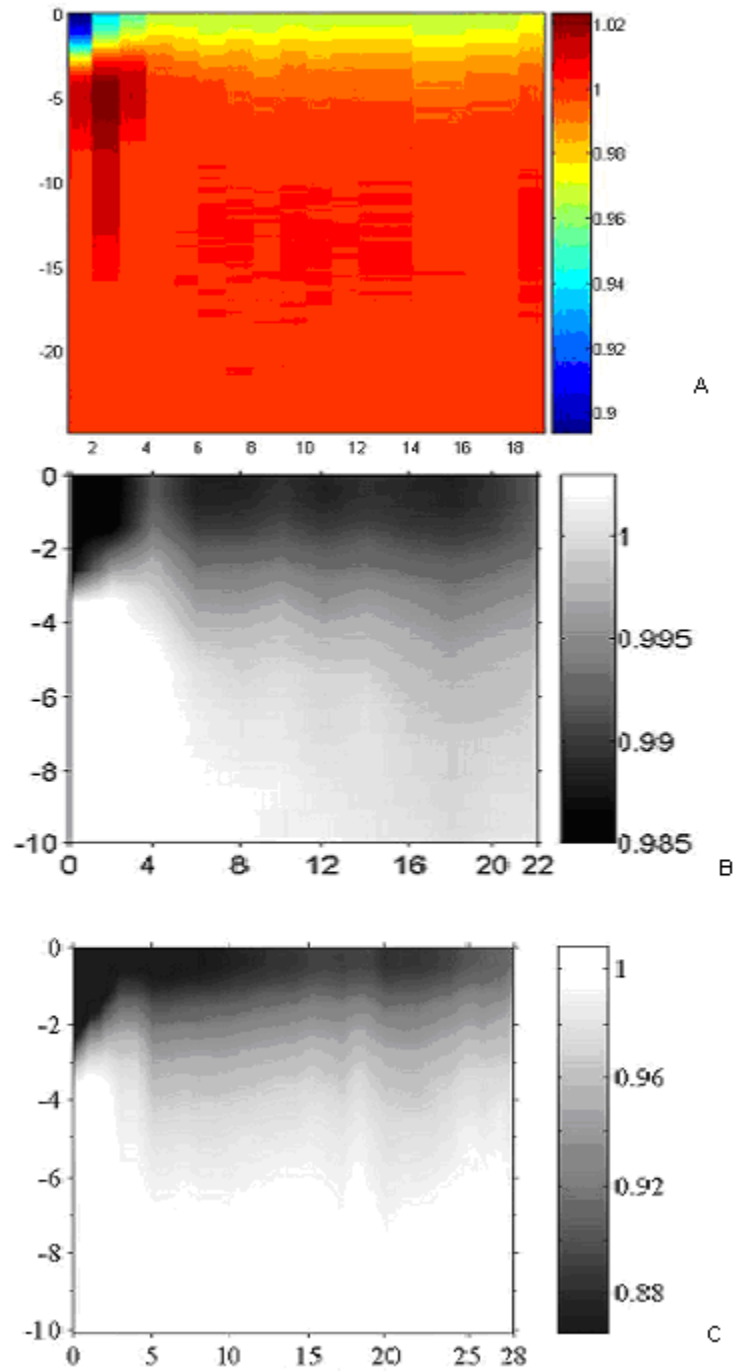


Figure 3-10: A 2D plot of the normalized conductance, which described as color brightness with the y-axis of the sample bias (mV) and x-axis of the applied field (T) for each junction. Figure (a), (b) and (c) correspond to junction A, B and C respectively.

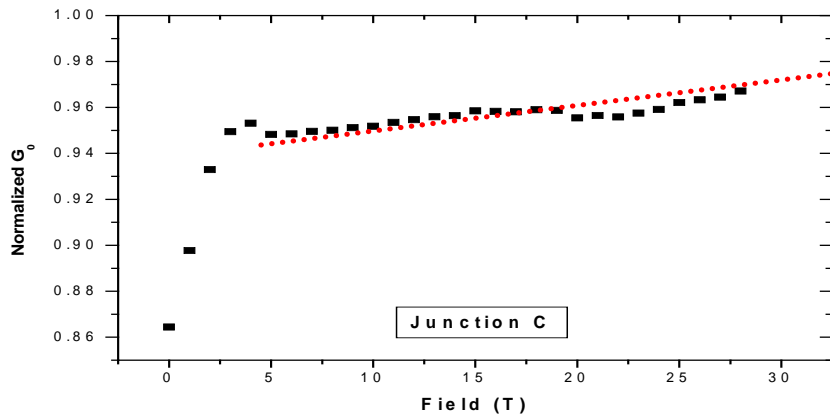
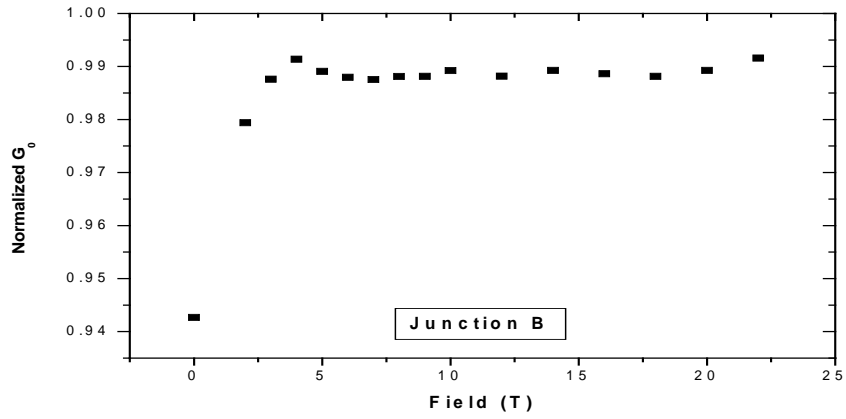
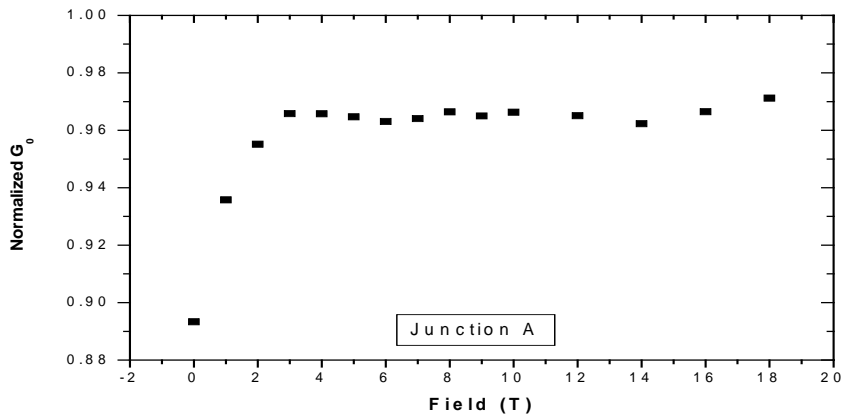


Figure 3-11: Normalized zero bias conductance for the each junctions.

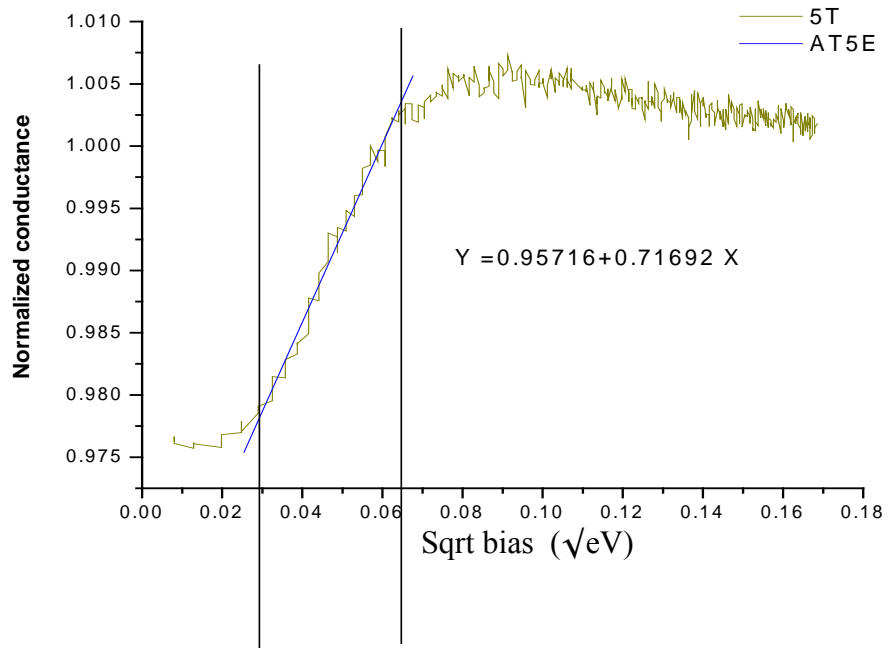


Figure 3-12: One example of the correlation gap fitting (junction A with 5 T), which is described as a square root dependence of the normalized conductance to the bias voltage.

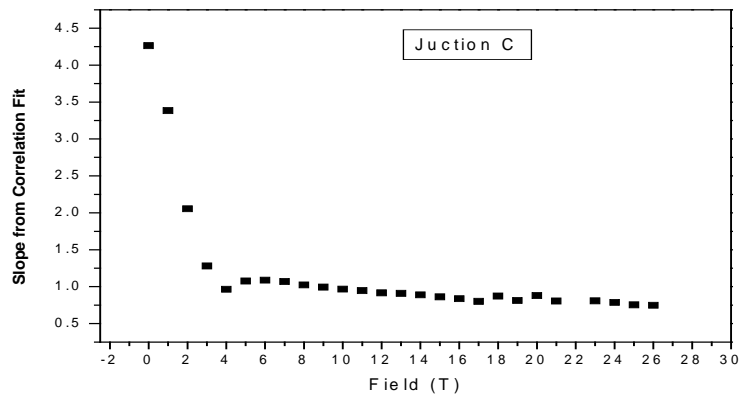
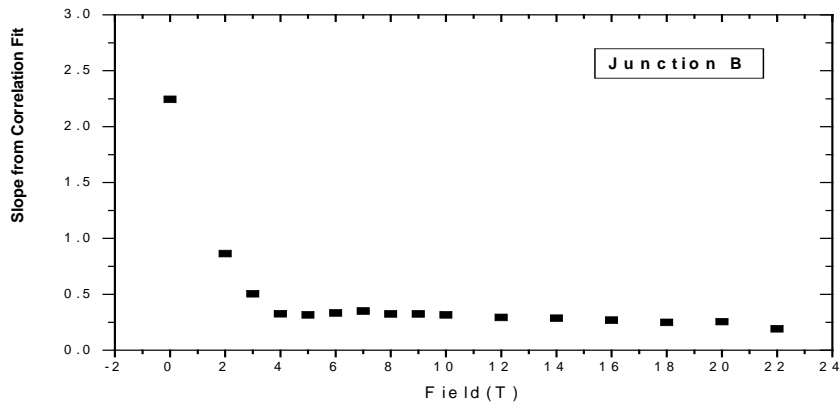
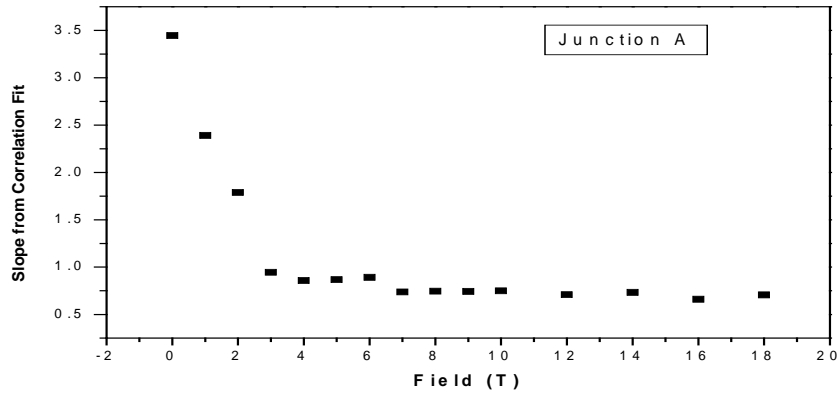


Figure 3-13: Slope vs. Field obtained by fitting the correlation gap for the normalized conductance for each junctions.

CHAPTER 4 POSITIVE MAGNETORESISTANCE OF MANGANITE THIN FILMS (PMR)

The low field magnetoresistance (LFMR) effect in hole-doped manganese oxides (manganites) has been studied extensively due to the potential for applications [95-97]. There is a strong connection between the magnetization and electronic transport properties of manganites, which affects properties at the microscopic level such as intrinsic tunneling due to the complex interdependence of spin, charge, and lattice degrees of freedom [56]. Although colossal magnetoresistance (CMR) is a characteristic of manganites, the required high fields (~ 1 T) are an impediment for practical applications. Several studies have attempted to overcome this limitation by studying the microscopic origin of the transport mechanism (e.g. spin dependent tunneling) at low fields. Here we report an intrinsic positive, anisotropic LFMR of a simple ultra thin film of $(\text{La}_{0.5}\text{Pr}_{0.5})_{0.67}\text{Ca}_{0.33}\text{MnO}_3$ (throughout this chapter LPCMO will indicate only this composition). We cautiously suggest that the LFMR may be due to tunneling magnetoresistance (TMR). We believe that this study of ultra thin films will lead to an understanding of TMR in more sophisticated manganite structures.

LPCMO thin films were grown on (110) NdGaO_3 (NGO) substrates by pulsed laser deposition (KrF 248nm) with a molecular oxygen pressure of 440mTorr. The NGO substrates were kept at 820 °C throughout the deposition. This procedure results in high quality epitaxial films. Thicknesses of 75 Å and 300 Å were used for this experiment. In the case of the 75 Å thick film, due to its high resistance the circuit shown in figure 4-1 was used for magnetoresistance measurements. The marked voltage for each result indicates the total bias across the circuit (V_B) i.e., the voltage across the sample and load resistance. Therefore the real applied bias across the sample will be much smaller for most cases. For the 300 Å thick film, a regular four-probe resistance measurement method was used.

4.1 LPCMO Thin Films (RvsT and Magnetization)

Figure 4-1 shows the temperature dependence of the resistance in different magnetic fields. In this measurement, the field was applied perpendicular to the plane of the film. At zero field, the metal insulator transition temperature, T_{IM} is around 65 K and it increases as the field is increased. The hysteresis, seen for lower fields in Fig. 1 decreases dramatically around 4 T. Colossal magnetoresistive behavior is observed around T_{IM} . The discrete steps, marked by arrows in the figure, can be due to the electronic phase separation, which is related to the fact that this film's thickness is small enough to confine the single-phase domain along the c-axis [98]. This R vs. T was taken before the field sweep (R vs. H) measurements. After the R vs. H measurement, R vs. T showed a different behavior in which no clear T_{IM} could be seen, which indicates the occurrence of irreversible changes in this system.

4.2 Metamagnetic Transition and Positive Magnetoresistance

Figure 4-2(a) describes one example of a metamagnetic transition (MMT) for the conditions in shown figure 4-3(a). The arrows indicate the field sweep direction. The irreversible MMT is clearly seen with 2 different resistances at zero field. A sharp drop accompanied these MMTs in resistance at a certain field (in this case at 1.8 T). The first LFMR after the MMT is circled. This set of LFMR data was obtained for one MMT at 50 K. It is observed that these LFMR data have a strong dependence on the history of the sample. The origin of the positive magnetoresistance (PMR) can be related to the spin flipping process between two ferromagnetic metallic (FMM) domains with different magnetization directions and spin dependent transport.

Figure 4-2(b) shows this spin flipping process with the sweeping of the magnetic field. Different size domains will have different coercive fields for each domain and it will misalign the magnetization of domains for weaker reverse fields (this is the origin of PMR) and as we

increase the field this misalignment will disappear. A, B, C and D throughout the remainder of this chapter correspond to the situations indicated in figure 4-2(a).

4.3 Directional and Strength Dependence of Bias Voltage and Field on PMR

Figure 4-3(a) shows the LFMR with the field aligned perpendicular to the plane of the film. For clarity, the MMT part has been removed from each LFMR result. The magnetoresistance $(R_H - R_0) / R_0$ for each temperature were shifted by a constant amount for clarity, where R_H and R_0 are resistances with and without magnetic field respectively.

The temperature dependence of this PMR can be interpreted as follows: After FMM domains and insulating regions are formed due to the MMT, the size of each metallic domain increases as the temperature is decreased, which results in a larger H_f (H_f indicates the magnetization flipping field for one domain and it is marked in the figures).

The LFMRs for a magnetic field in the plane of the film and in directions parallel and perpendicular to the current are shown in Figure 4-3(b) and Figure 4-3(c) respectively. In the case in which the field is parallel to the current, the H_f (~ 500 gauss) is similar in magnitude to the coercive field when the field is applied in the plane of the film, which is found in magnetization measurements for the thicker film (300 Å). If the coercive field does not change significantly within this range of thickness, this result will support the possibility that this PMR is due to spin dependent tunneling magnetoresistance.

The different H_f for the two in-plane field directions of (Figure 4-3(b) and 4-3(c)) is possibly due to the current assisted domain wall motion resulting from the spin torque in the magnetic domain under simultaneous field and current application [99].

For both the in-plane field directions, H_f increases as temperature decreases, but the magnitude of the PMR has a different behavior than the magnetic field applied perpendicular to the plane of the film as shown in Figure 4- 3(a). The difference in behavior between the in-plane

and out-of-plane magnetic fields still needs to be addressed keeping in mind the microscopic domain formation and correlation between the spin alignment and current. We have measured the LFMR for the 300 Å film and observed a similar PMR effect in that case, although the detailed behavior is different from the LFMR of the 75 Å film.

The data in figure 4-4(a) provides a test for the spin dependent tunneling mechanism. As bias voltage decreases we can see an increase in the effect of PMR, which is expected for the tunneling case. However, for higher bias voltage, no consistent result could be obtained as shown in figure 4-4(b) which shows an increase of PMR with increasing bias voltage and figure 4-4(c), which shows a decrease of PMR with increasing bias voltage.

4.4 Discussions

The LFMR effect for LPCMO thin films on NGO was measured for 3 different field directions: field perpendicular to the plane of the film, field parallel to the film plane but perpendicular to the current and field parallel to the current. Each direction has a distinctive PMR. The difference in the temperature dependence of the PMR magnitude between the case in which the field is perpendicular to the film (Figure 4-3(a).) and that in which the field is parallel to the film (Figure 4-3(b) and (c)) reflects the different domain formation mechanisms and domain sizes due to the intrinsic film properties such as the different strains for these two directions [126]. The difference in the PMR for each of the three directions may also indicate an anisotropic magnetoresistive (AMR) response of the material similar to that found in other compositions of manganites [100, 101]. This AMR is generated not only by the structural anisotropy but also by the dynamical response of the domains to the simultaneous application of the current and magnetic field and the resultant spin-orbit scattering which is due to the anisotropic electron mean free path's dependence on the spin and the angle between current and the magnetization [102, 103].

Hence, the origin of LFMR in this film can be considered to be an additional magnetoresistance resulting from some type of spin dependent scattering, which appears due to the fact that the polarization axis of the conduction electrons cannot be arranged adiabatically along the local magnetic field within the domain wall when its thickness approaches the spin diffusion length [104]. Whether or not, this spin-dependent scattering at the domain boundary is related to the TMR, which is found in other perovskite-type transition-metal oxides [105] is debatable, although the bias dependence of the LFMR points to such an effect. The microscopic description of the domain formation (phase separation) and spin and electron dynamics is expected to play a key role in determining the LFMR. The phase separation in manganites has been described earlier and I will now discuss the possible role of a spin-glass like state in manganites in determining the nature of the LFMR. On the application of a magnetic field, polycrystalline $(\text{Tb}_{0.33}\text{La}_{0.67})_{0.67}\text{Ca}_{0.33}\text{MnO}_3$ shows an insulator-metal transition at low temperatures as a result of the alignment of Mn^{3+} and Mn^{4+} core spins [106]. This low temperature magnetic state is considered to be a spin glass state. The formation of this state is a universal phenomena for $\text{Re}_{0.67}\text{A}_{0.33}\text{MnO}_3$ in which the tolerance factor $f \leq 0.907$ [61]. For our compound $(\text{La}_{0.5}\text{Pr}_{0.5})_{0.67}\text{Ca}_{0.33}\text{MnO}_3$, f is 0.85 so it is in this regime. Based on another magnetic and magneto transport properties experiment on $(\text{Tb}_x\text{La}_{1-x})_{0.67}\text{Ca}_{0.33}\text{MnO}_3$ new superparamagnetic states¹ were also suggested [107]. As shown in figure 4-5 superparamagnetic states appear in a certain range of Tb concentration (x), which directly corresponds to the tolerance factor f of the material. In our material, the formation of ferromagnetic domains (clusters) which start to appear before the insulator to metal transition (as seen from magnetization measurements), suggests the possibility of the existence of such

¹ Here superparamagnetic state means a paramagnetic state with a large net magnetic moment due to micro-scale clusters of ferromagnetic phases.

superparamagnetic states, i.e. the metamagnetic transition observed in a certain temperature range may be due to the existence of a superparamagnetic state in that temperature range.

Do such spin-glass like and superparamagnetic states determine the origin and nature of the phase separated state in our material? Magnetization measurements of polycrystalline samples of $\text{La}_{0.225}\text{Pr}_{0.4}\text{Ca}_{0.375}\text{MnO}_3$ show dynamic phase separated and spin glass states in a certain temperature range [108]. The spin glass state can be considered to be a blocked (frozen) metastable state due to the high energy barriers and strain in between domains of different phases. This state can be unblocked by either increasing the thermal energy to overcome the barrier energy or increasing the field at a given temperature. For our epitaxially grown $(\text{La}_{0.5}\text{Pr}_{0.5})_{0.67}\text{Ca}_{0.33}\text{MnO}_3$ thin films, disorder caused by Pr substitution induces comparable energies between phases and this results in phase competition which could lead to a spin glass state in the presence of disorder (detailed discussion in chapter 6).

Additionally, in such ultra-thin films the energy barrier between domains will depend on the magnetic structure of the domain walls and three possible types of domain walls can be considered for a classical double exchange ferromagnet [109]. They are the conventional Bloch wall, abrupt Ising-type wall and stripe wall (a stripe of AFM phase between FM domains) depending on the spin stiffness and the strength of anisotropy. The Ising-type wall is feasible only when the doping is extremely small which is not the case for our sample ($x = 0.33$). We expect that the domain walls, which appear in our ultra-thin films are either a Bloch type or stripe wall², which could become insulating due to the substrate induced strain. The LFMR could be due to tunneling across such insulating domain walls [127].

² When a structure is strongly anisotropic and the free energy for the ferromagnetic and antiferromagnetic phases are very close to each other, the stripe wall is preferred over the Bloch wall.

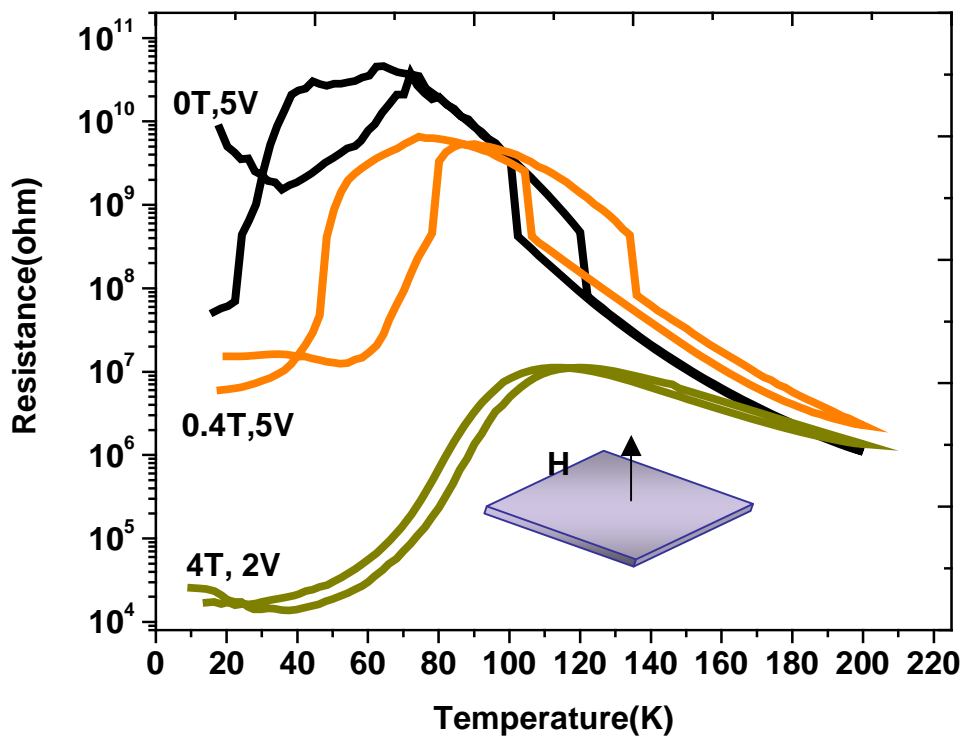


Figure 4-1: Resistance vs. Temperature curves for different magnetic fields. The magnetic field is applied perpendicular to the plane of the film. The load resistance R_L was 10 Mohm and the bias voltages across the whole circuit used for each field are given in the figure. The inset shows the circuit diagram used for the measurement and $R_{\text{sample}} = (V_B - V_L) / (V_L / R_L)$

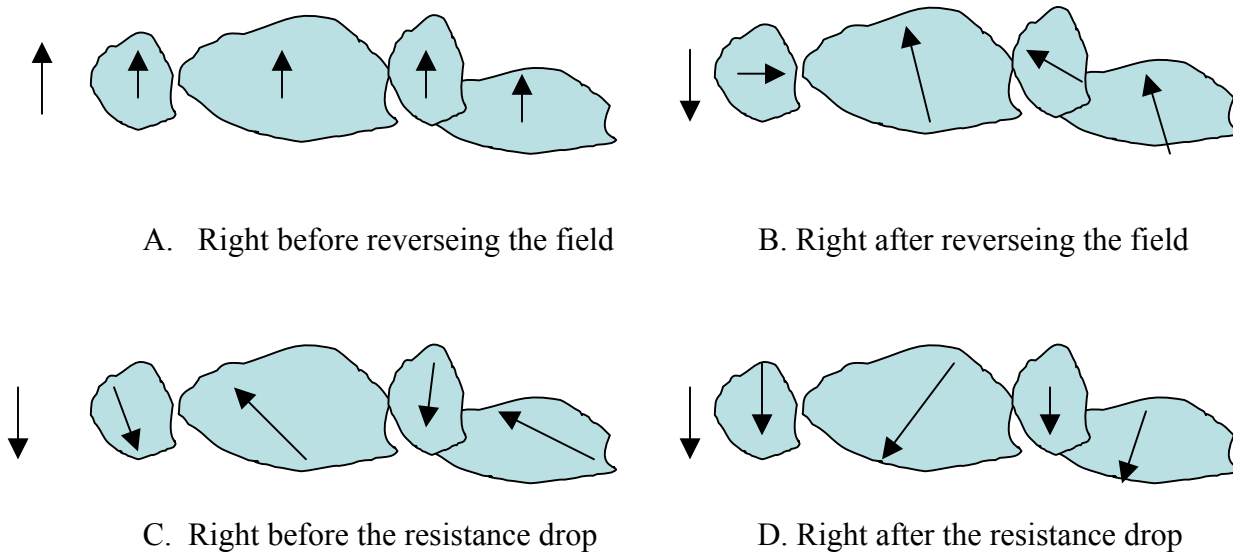
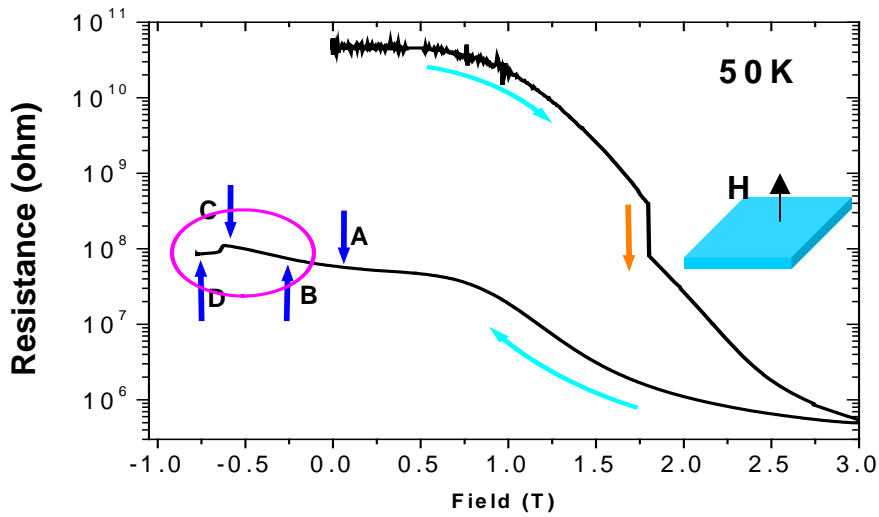


Figure 4-2: Metamagnetic transition and its mechanism. (a) Metamagnetic transition at 50 K for the conditions shown in figure 4-3 with a bias voltage through the whole circuit $V_B=2$ V, connected in series with a resistance $R_L=10$ Mohm (b) Schematic drawing for the spin flipping process in magnetic domains with a switching magnetic field.

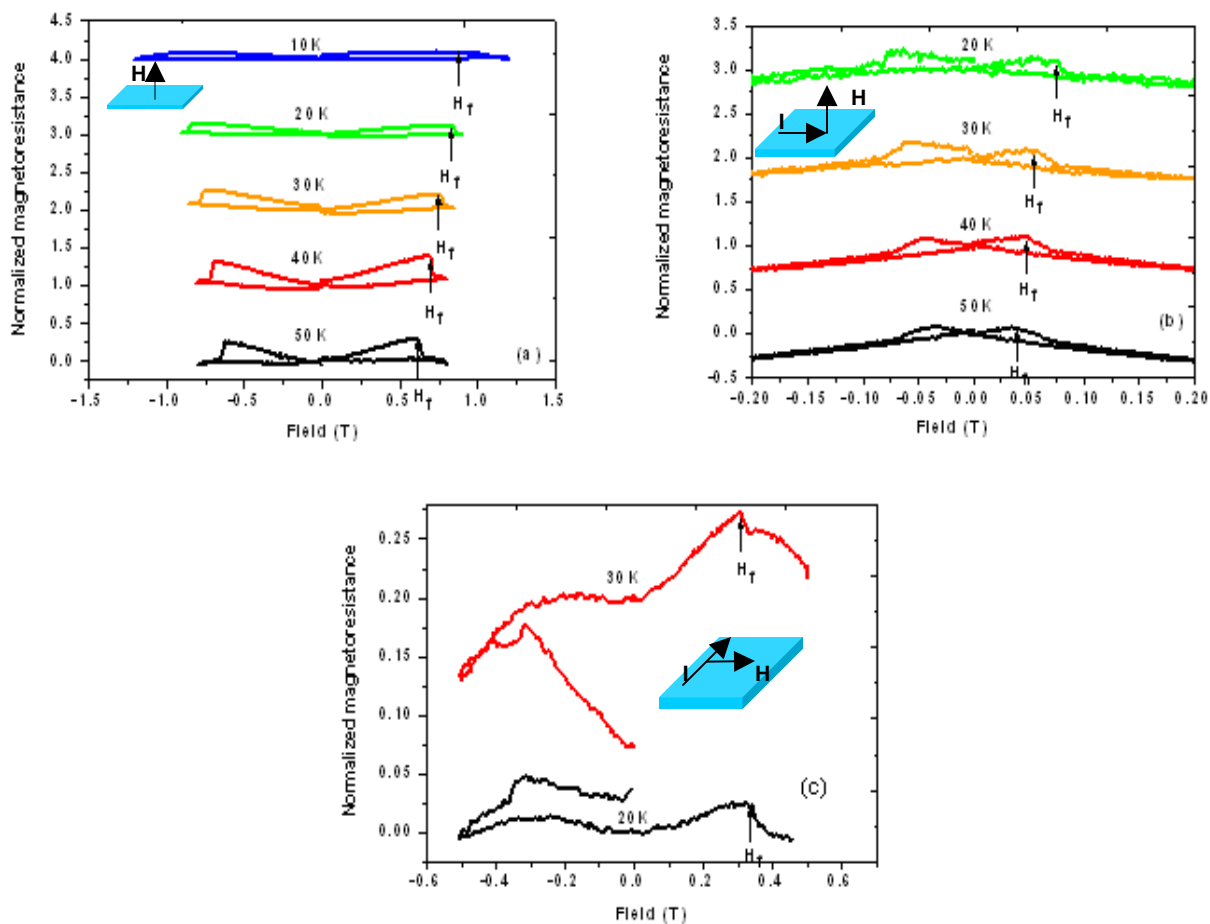


Figure 4-3: Low field magnetoresistance for each direction of applied field. (a) Low field magnetoresistance when the field is applied perpendicular to the film plane with $V_B=2$ V, $R_L=10$ Mohm. (b) Low field magnetoresistance when the field is applied parallel to the current with $V_B=5$ V, $R_L=10$ Mohm. (c) Low field magnetoresistance when the field is applied parallel to the plane of the film and perpendicular to the current with $V_B=5$ V, $R_L=10$ Mohm.

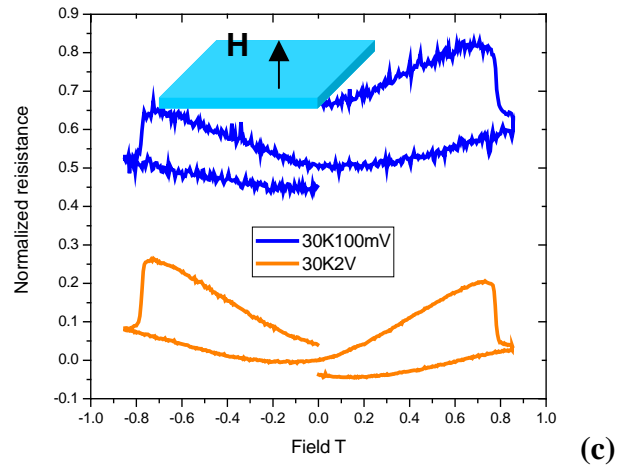
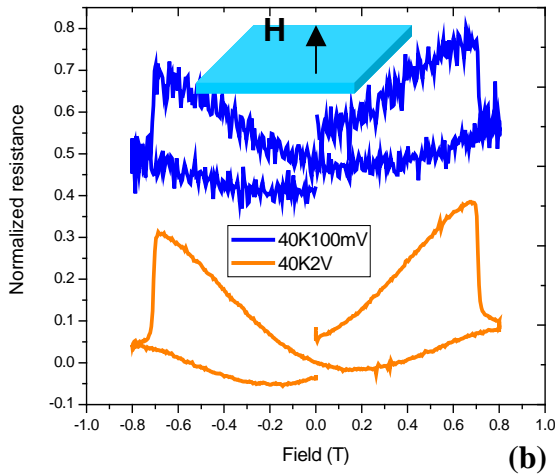
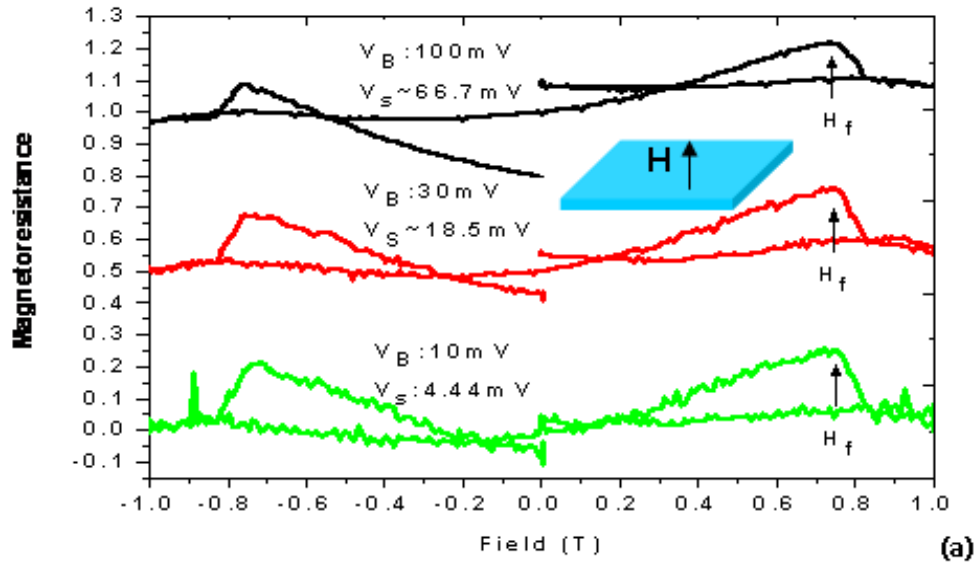


Figure 4-4: Bias voltage dependence of LFMR. (a) Bias voltage dependence of LFMR in the low applied bias voltage range at 40 K. Bias voltage across the whole circuit V_B and across the sample only V_S are marked in the graph. (b) Bias voltage dependence of the LFMR in the high-applied bias voltage. The magnetic field was applied perpendicular to the film and the current direction was parallel to the film. (c) Another bias voltage dependence of the LFMR in the high applied bias voltage range at 30 K. The magnetic field was applied perpendicular to the film and the current direction was parallel to the film.

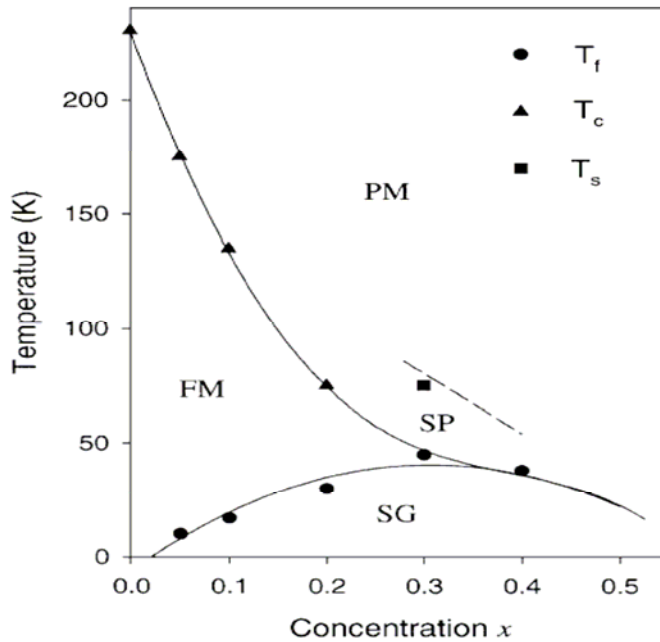


Figure 4-5: Phase diagram of $(Tb_xLa_{1-x})_{0.67}Ca_{0.33}MnO_3$ obtained from magnetic and magnetic transport measurement as a function of Tb concentration x . SP and SG indicate superparamagnetic state and spin glass state respectively [107].

CHAPTER 5 MICROFABRICATED DOUBLE LAYER STRUCTURE

Along with the study of transport properties in the direction parallel to the plane of the study of transport properties in the out of the plane direction can provide information necessary for a more complete understanding of the dynamics of the phase separated state in mixed-valance manganite thin films. First, the intrinsic anisotropic properties caused by the nature of sample growth (epitaxially grown on a substrate with a small lattice parameter mismatch) lead to the importance of this experiment. Second, due to the nature of a thin film, the length scale along the out-of-plane electron transport direction is constrained to a dimension on the scale of nanometers and this can create a special condition for the dynamics of phases.

However, to study the transport properties in the perpendicular direction of the thin films, we need a specially designed structure. For this purpose, we used an etched double composition layered manganite structure. The fabrication of this structure was described in detail in Chapter 2. This structure can be described as two capacitors connected in series consisting of a gold contact pad and an LCMO (through this chapter LCMO will indicate $\text{La}_{0.67}\text{Ca}_{0.33}\text{MnO}_3$) layer acting as electrodes and a LPCMO (through this chapter LPCMO will indicate $(\text{La}_{0.4}\text{Pr}_{0.6})_{0.67}\text{Ca}_{0.33}\text{MnO}_3$) layer in between acting as a dielectric material. The advantage of this structure is that the dielectric properties of the phase separated state of LPCMO can be studied along with the out-of-plane transport properties.

5.1 Perpendicular Direction of Transport Properties (RvsT)

Figure 5-1(a) shows resistance versus temperature (R vs. T) behavior of monolayer LPCMO and LCMO films. It also shows the R vs. T behavior of LPCMO grown on top of LCMO and partially etched LPCMO on top of LCMO films. The Resistance of LPCMO was measured along the in-plane direction of the film and it shows a metal-insulator transition at 70

K with the characteristic hysteresis for warming and cooling. The resistance of LCMO was also measured along the in-plane direction of the film and it shows a metal-insulator transition at 250 K and no hysteresis. A 26 nm thick LPCMO film grown on top of 60 nm LCMO shows the combined characteristics of LPCMO and LCMO, which are two metal insulator transitions at temperatures near the transition temperatures of LPCMO and LCMO and hysteresis corresponding to that seen in LPCMO. After that we deposited gold contact pads, which also acted as masks for etching. The resistance curve, which was obtained after the exposed LPCMO was etched, showed higher resistance due to the reduction of the cross sectional area through which current could pass. The resistance value is very close to that of the LCMO thin film before LPCMO was deposited on it except around the transition temperature, which is expected if the exposed LPCMO has been etched away and we have obtained the structure shown in figure 5-1(b). However it still has the two distinct transitions due to the LCMO and LPCMO and hysteresis from the LPCMO film. This behavior can be attributed to the out-of-plane transport properties of the remaining LPCMO under the gold pads.

Figure 5-2(a) shows the current dependent resistance for the etched double compound layer of the LPCMO and LCMO. A clear current dependence is observed around the temperature region where hysteresis is seen in the R vs. T curves and at low temperatures.

In the low temperature region, with low applied current, the resistance upturn is clearly shown in figure 5-2(b). The origin of this upturn was hypothesized to be the presence of disorder in the LPCMO film, since this kind of upturn was observed in other experiments with thin films of LPCMO with low applied current (or low bias voltage) measurements but not in the LCMO thin films. As we increase the current, this upturn starts to decrease and the effective starting current is the same as the effective starting current of the hysteresis region, which is between 10

μA and $100 \mu\text{A}$. This suggests that this upturn is closely related to the phase separations of LPCMO. Possibly, the amount of disorder increases during the growth of LPCMO on top of LCMO. This is suggested by the comparison of (Atomic Force Microscopy) AFM images of LPCMO films grown on bare perfect crystal NGO substrates and LPCMO films grown on top of LCMO films grown on similar NGO substrates. As a result, the charge ordered state in the LPCMO films could be enhanced and may have induced this current (or electric field) dependent phenomenon in the low temperature region. To eliminate the possibility of a heating effect as the origin of this dependence of the upturn on the current, we measured the resistance in the lower temperature region (down to 50 mK) with the help of Yoon Lee's group the measurements were made by Pradeep Bhupati and Matt Spencer. The result allows us to distinguish the heating effect, which results in a plateau in the resistance curve below 100 mK , which is clearly different from this reduction of the upturn. Also the result from the low temperature measurement shows the logarithmic dependence of the resistance, which is expected from sample, which is disordered due to weak localization.

Around the temperature region of hysteresis, the metal insulator transition induced by current (or electric field) was observed and this is shown in detail in figure 5-2(c).

As the current is increased from $100 \mu\text{A}$ to $500 \mu\text{A}$ the temperature dependence of the resistance for the cooling curve changed from insulator like to metal like. To estimate the voltage (or current) at which the insulator to metal transition occurs, we plotted the voltage drop across the sample as a function of applied current, which is shown in figure 5-2(d). In the low current (or voltage) region, the cooling plot of this sample shows a clear contrast to the almost ohmic dependence of the warming plot. And the insulator to metal transition activation voltage can be

estimated to be around 0.25 V, which is 2 orders of magnitude smaller than the transport measurement in the parallel direction of the LPCMO thin film of the same composition [51].

To confirm this nonlinear conductivity for the cooling curve, we directly measured I-V of the sample, for the given temperature in the cooling case (Figure 5-3). As the temperature is reduced, the nonlinearity of the conductance curve decreases. However this process could be reversed by applying current (or electric field), contrary to the case in which the electric field (or current) was applied along the direction parallel to the sample with same compound [51]. The magnetic field dependence of this nonlinearity was also measured (Figure 5-4). As the magnetic field increases, a decrease of the nonlinearity could be observed. From this result, it can be concluded that the origin of the magnetic field induced ohmic relation in the conductance is related to the formation of the magnetic metallic domains, which resulted from the melting of the charge ordered phase as observed in other similar charge ordered manganite samples [110, 111]. The current induced (or electric field induced) metallic state is explained by a percolation process with the same origin as the magnetic field induced phase transition observed in another result [112] and not as the formation of filamentary conducting paths between metallic domains [50]. However this can still be controversial based on a new magnetization measurement on LPCMO samples. Recently, measurements of magnetization and conductivity of cross-structured thin films, done by Tara Dhakal in our group reveals that the magnetization of $(\text{La}_{0.4}\text{Pr}_{0.6})_{0.67}\text{Ca}_{0.33}\text{MnO}_3$ is not significantly affected during the temperature induced insulator-metal phase transition and for the electric field induced metal-insulator transition, a reshaping of the present metallic domains occurs at the transition temperature.

With this complicated background scenarios concerning the phase dynamics surrounding the insulator to metal transition in mixed- valence manganites, we studied the dielectric characteristics in this sample due to its phase-separated nature at the transition temperature.

5.2 Capacitance Effect (From Structure and Intrinsic Phase Separation)

The metal-insulator phase separated nature of LPCMO at the temperature around which hysteresis is seen, and the characteristics of the structure as shown in figure 5-7, this structure shows frequency dependent capacitance properties as mentioned before at the introduction of this chapter. First we measured frequency dependent complex impedance using two lock-in amplifier methods as shown in detail in Chapter 2. Figure 5-5 shows the modulus of the impedance and figure 5-6 shows and the corresponding phase change as a function of temperature. The Low frequency (up to 2 kHz) modulus result shows no significant changes overall (Figure 5-5(a)).

As frequency increases over 10 kHz, a significant change appears around the insulator to metal transition temperatures for LPCMO. A Detailed view of this temperature range for a given frequency is shown in figure 5-5(b). In the temperature range 130 K to 105 K for the cooling curve, a frequency dependent insulator to metal transition could be clearly observed which implies the existence of some kind of threshold frequency for the dielectric domains inside the LPCMO film. Since LPCMO is not a perfect insulator with their fluid phase separated nature, we can expect leakage in this capacitor model, which devolves the interpretation of the result into a difficult and complex mystery.

The frequency dependent phase changes of the complex impedance shown in figure 5-6, is obtained by setting the phase to zero at high temperature (close to room temperature) which is expected to have a single paramagnetic charge delocalized phase. We also tested setting the phase to zero at low temperature (10 K), which is considered to be a static phase separated state, it resulted in a vertical shift of the whole curve, and other than that everything remained the same

as in the case in which the phase was set to zero at high temperatures. Therefore the meaning of the absolute value of each phase might be meaningless at this point. Only their relative values at a given temperature between different frequencies or relative phase values through a temperature range for a given frequency, are considered to have significant meaning. The increase and decrease of the hysteresis in the phase is observed as frequency is increased (maximum hysteresis is expected between 10 kHz and 40 kHz). The temperature for a local minimum phase value, when it exists, (at 100 kHz, no more local minimum is observed) for both warming and cooling cases, at a given frequency, stays at the same temperature with the variation of frequency. The meaning of this local minimum value is not so clear, however considering its temperature is same as the local maximum of the resistance in DC transport measurements, it can be suggested that this feature is strongly related to the phase separation of LPCMO in that temperature range. Also it is possible that this hysteresis reflects the difference in the mobility (or rigidity) of each dielectric domain itself [113] of their polarization during fluid phase separation between cooling and warming cases for a given frequency. Those dynamic mechanisms for each domain can be applied for a different frequency result in the same way, for example, the mobility of either domain itself or the polarization of a domain can be maximized at 20 kHz among the results shown.

We first made a capacitor model based on our structure and electrical properties, which is shown in figure 5-7 through figure 5-9. With the model suggested in figure 5-9 we can set

$$R_{Loss} \equiv \frac{1}{\omega C_2} \quad , \quad R_{Leak} \equiv R_0$$

And as shown in figure 5-7, $R_S = R_{LCMO}$.

In this case the total impedance of the circuit can be described in the following way

$$Z = Z_R + iZ_{im}$$

where Z_R is the real part of the impedance and Z_{im} is the imaginary part.

$$\begin{aligned} Z_r + iZ_{im} &= R_s + \frac{1}{\left(\frac{1}{i\omega C_1}\right)^{-1} + \left(\frac{1}{\omega C_2}\right)^{-1} + \frac{1}{R_0}} \\ &= R_s + \frac{1}{i\omega C_1 + \omega C_2 + \frac{1}{R_0}} \\ &= R_s + \frac{\frac{1}{R_0} + \omega C_2 - i\omega C_1}{\left(\frac{1}{R_0} + \omega C_2\right)^2 + (\omega C_1)^2} \end{aligned}$$

Then from this we can get real part and imaginary part of the impedance which is,

$$Z_r = R_s + \frac{\frac{1}{R_0} + \omega C_2}{\left(\frac{1}{R_0} + \omega C_2\right)^2 + (\omega C_1)^2}$$

$$Z_{im} = \frac{-\omega C_1}{\left(\frac{1}{R_0} + \omega C_2\right)^2 + (\omega C_1)^2}$$

Now we want to get C_1 and C_2 separately using the relation above.

$$\frac{Z_r - R_s}{Z_{im}} = \frac{-\left(\frac{1}{R_0} + \omega C_2\right)}{\omega C_1}$$

$$Z_r - R_s = \frac{\frac{1}{R_0} + \omega C_2}{\left(\frac{1}{R_0} + \omega C_2\right)^2 + (\omega C_1)^2}$$

$$Z_{im} = \frac{-\omega C_1}{\left(\frac{1}{R_0} + \omega C_2\right)^2 + (\omega C_1)^2}$$

$$(Z_r - R_s)^2 + Z_{im}^2 = \left\{ \left(\frac{1}{R_0} + \omega C_2\right)^2 + (\omega C_1)^2 \right\}^{-1}$$

Finally, the variables C_1 and C_2 could be separated.

$$Z_r - R_s = \left(\frac{1}{R_0} + \omega C_2\right) \left\{ (Z_r - R_s)^2 + (Z_{im})^2 \right\}$$

$$Z_{im} = -\omega C_1 \left\{ (Z_r - R_s)^2 + (Z_{im})^2 \right\}$$

Then with simple math we can get C_1 and C_2 separately in terms of other variables. The variables Z_r , Z_{im} and R_s can be very easily determined experimentally other than R_0 , which is the leaky part of the capacitance due to the fact that LPCMO is not a perfect insulator. Therefore we used the DC resistance measurement of the resistance of LPCMO as R_0 . The result is shown in figure 5-10. However, we were not able to fit the result to the Cole-Cole plot [114]. This implies that our model is not quite right for our sample partially due to the fact that the interface effect related to the Schottky barrier was ignored. Therefore we measured the capacitance of this sample directly using a capacitance bridge in collaboration with Hebard's group the measurements were made by Seffatin Tongay, which showed more or less a qualitatively similar result. We are still looking for a better model for this structure, which can provide an interpretation for our data.

5.4 Summary

DC and AC transport properties for the perpendicular direction of the LPCMO thin film were studied using the specially designed etched double compound layered maganite structure. Resistance plots obtained by DC measurement give clear indications concerning the characteristics of LPCMO around the insulator to metal transition temperature for LPCMO. Nonlinear conductance due to the phase separated nature of LPCMO was observed and their magnetic relevance is further suggested by removing this nonlinearity by applying a magnetic field. A reduced critical current (or static electric field), in comparison with transport measurements in the parallel direction, for the insulator to metal transition in the temperature region of fluid phase separation was observed. The dynamics of these phase separated domains in LPCMO was studied by measuring complex impedance. Short consideration about the rigidity of the domain itself and/or polarization inside the domain was suggested. However, we need a more detailed interpretation and insightful model for a deeper understanding of this result.

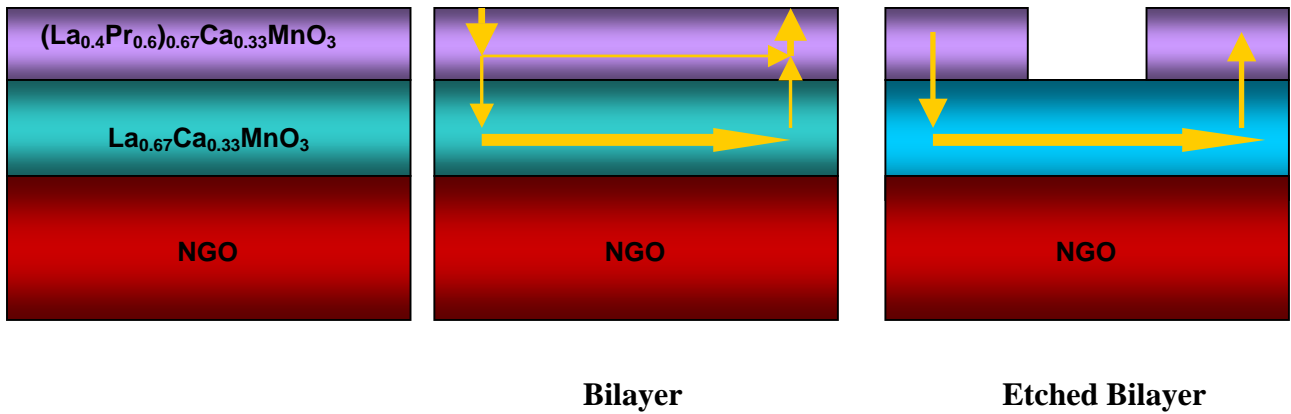
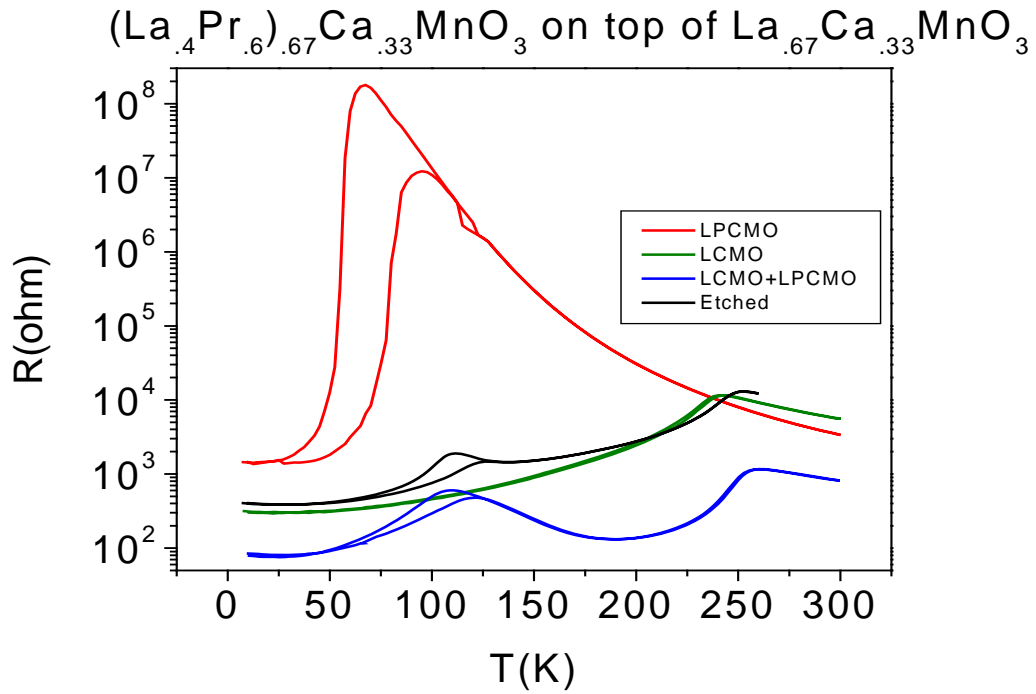


Figure 5-1: Double layer structure with LPCMO on top of LCMO. (a) Resistance vs. Temperature for 30 nm LPCMO (Red), 30 nm LCMO (Green) Double layer with 26 nm LPCMO on top of 60 nm LCMO (Blue) and partially etched 26 nm LPCMO on top of 60 nm LCMO (Black). All films were deposited on NdGaO_3 substrates. (b) Schematic drawing for the current paths depending on the related structure.

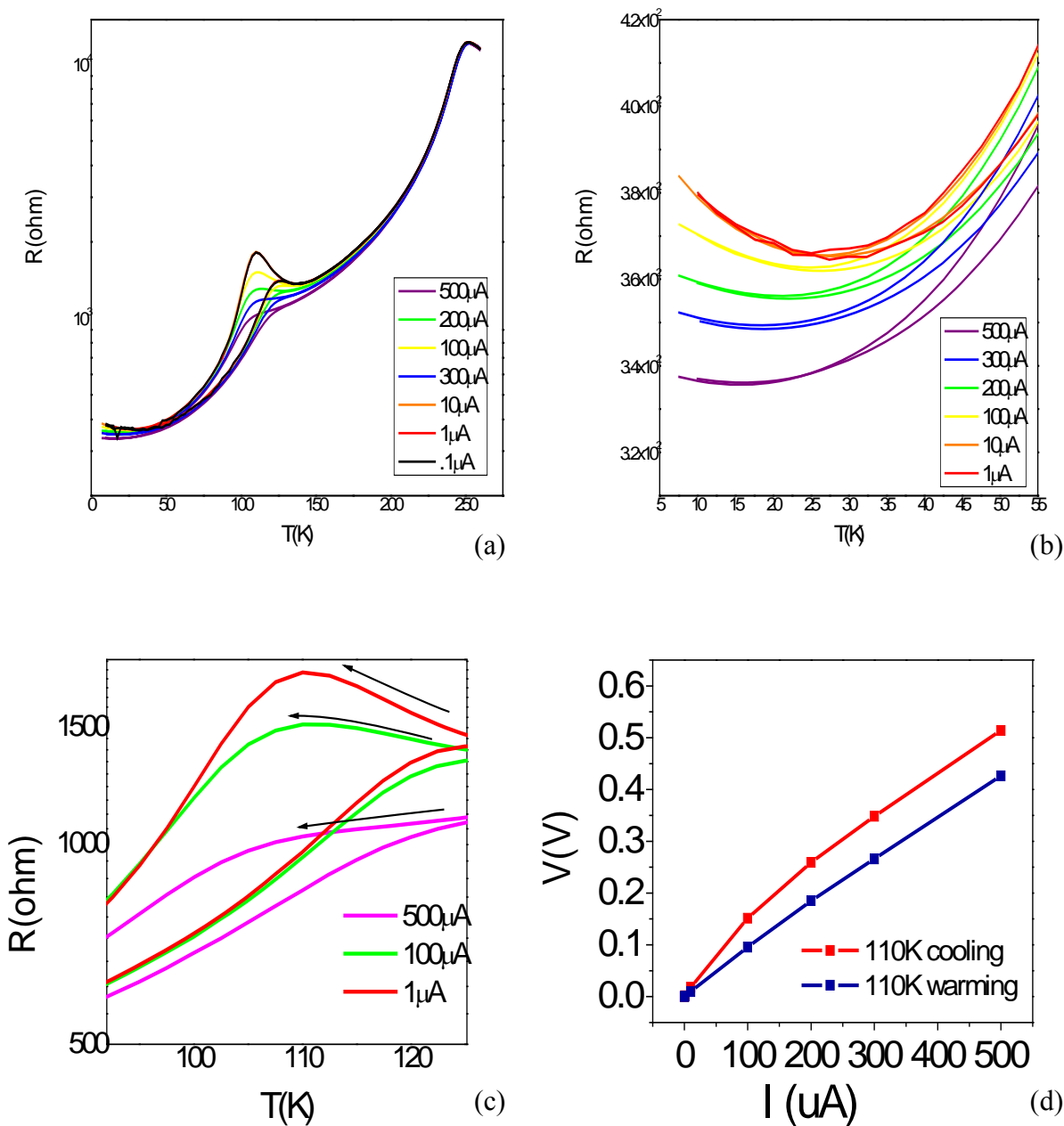


Figure 5-2: Current (or electric field) effect for the partially etched double compound layer of LPCMO on top of LCMO (a) Current dependent resistance vs. temperature. (b) Detail of the region of low temperature. (c) Detail of the region around transition temperature. (d) Plot of the current dependence of the voltage drop across the sample at 110 K obtained by reading the current dependent R vs. T of (a).

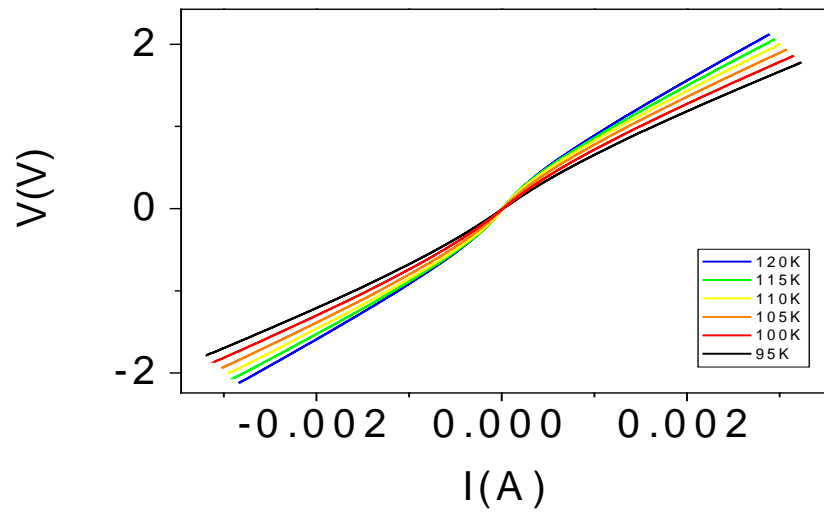


Figure 5-3: Actual measurement of the current dependence of the voltage drop for a different set temperatures while cooling

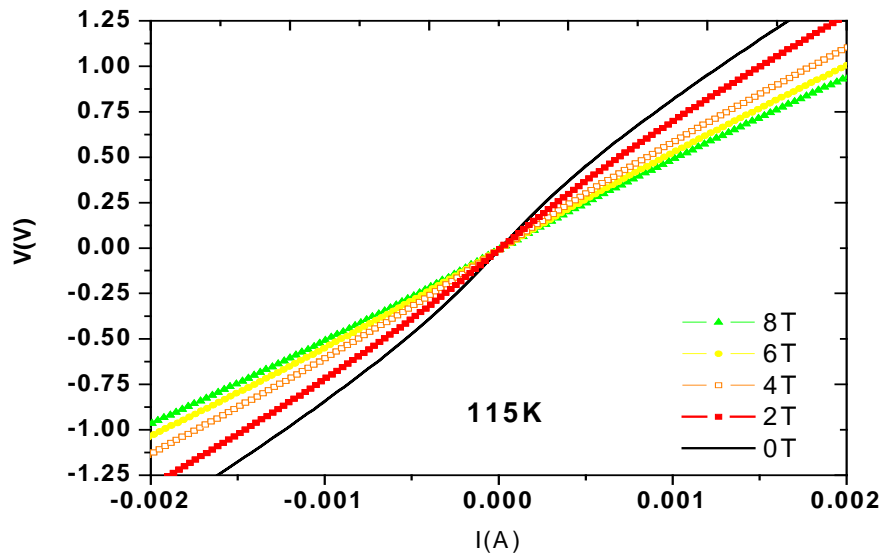
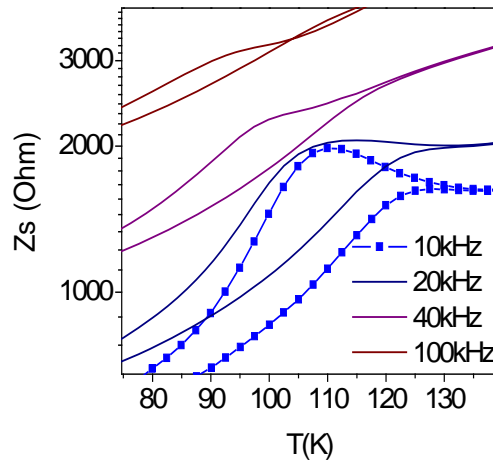
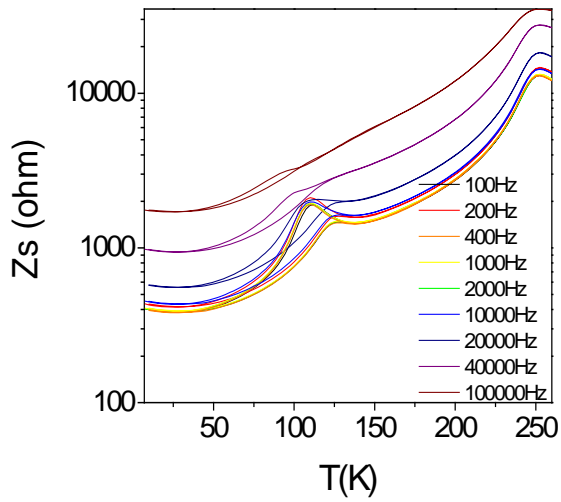


Figure 5-4: Measurement of the current dependence of the voltage drop for a different set of fields at 115 K while cooling



A

B

Figure 5-5: The modulus of the complex sample impedance as a function of temperature (a) Frequency dependent complex impedance in entire temperature range. (b) Detailed view of the frequency dependent modulus of the sample impedance around the transition temperature.

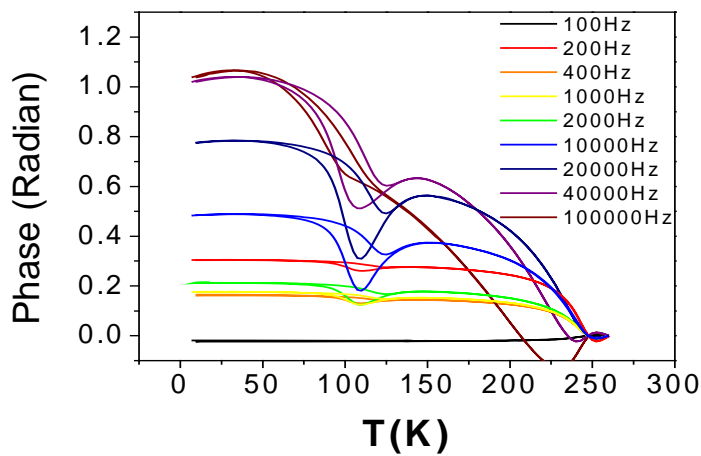


Figure 5-6: Frequency dependent phases of the complex sample impedance as a function of temperature.

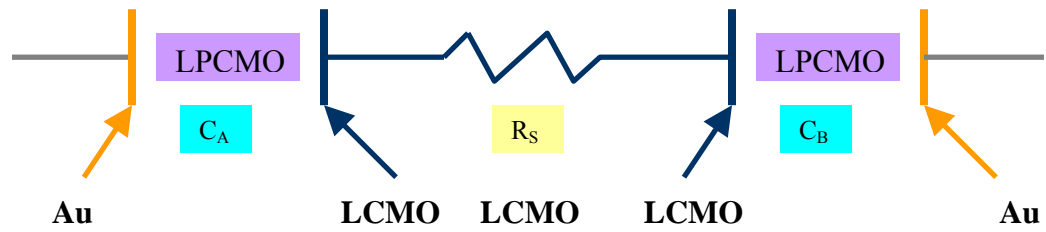


Figure 5-7: Conceptual diagram of the model of our sample structure in the LPCMO phase transition temperature range. The sample is modeled as two capacitors in series with the LPCMO as a dielectric material of each capacitor with a Au contact pad as one electrode and LCMO as a the other electrode and as a resistor connecting the two capacitors.

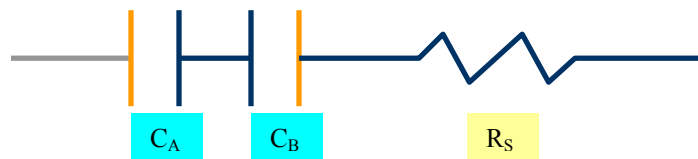


Figure 5-8: Changing the position of a capacitor from figure 5-7 to an equivalent circuit to allow the combination of the two capacitors C_A and C_B into one modified complex capacitor.

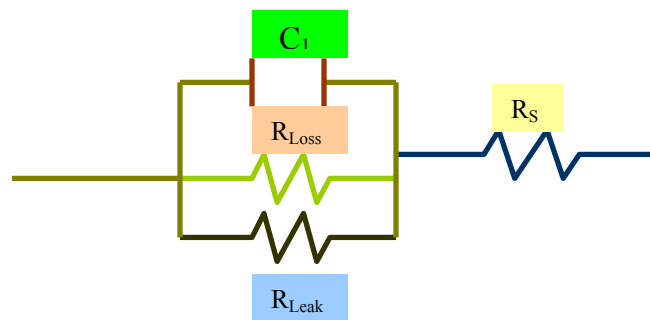


Figure 5-9: Complex capacitor model for our etched double layer structure, which has a leaky and a lossy part in it due to the phase separated nature (which indicates it is not a perfect insulator) of LPCMO.

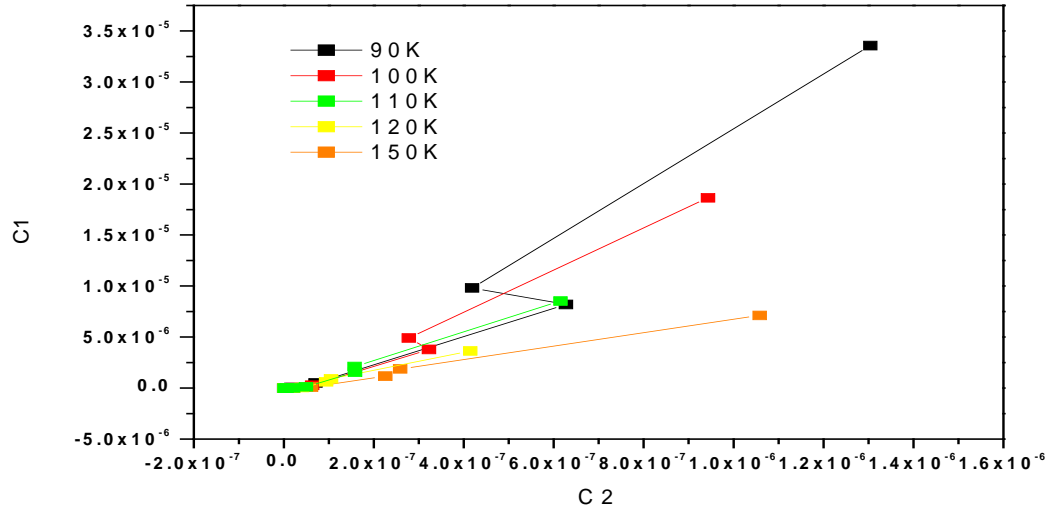


Figure 5-10: Plot of C1 Vs. C2 obtained from suggested modeling in figure 5-9. Warming run values for each temperature were considered in here.

CHAPTER 6
STRAIN AND DISORDER EFFECT ON MANGANITE

6.1 Overview about Strain and Disorder Effect on Manganite

The Jahn Teller distortion induced polarons and Holstein breathing mode polarons (or in short small polarons) explains the high temperature insulating behavior of manganite systems [63, 115-117] while double exchange explains the ferromagnetic metallic phase in manganite system [54-56]. However, even for pure phase manganite systems, the temperature dependence of the resistance through the whole temperature range, which includes the phase transition from the ferromagnetic metallic phase to the paramagnetic insulating phase and the Hall effect can not be explained only by these polarons. The inelastic carrier hopping between localized states induced by magnetic disorder and nonmagnetic disorder is crucial to solving these problems. Magnetic disorder is usually caused by an inhomogeneous core spin distribution due to the topological stability obtained from thermal fluctuations and nonmagnetic disorder can be caused by structural disorder which is caused by randomly replacing a La ion by a dopant ion or the different lattice distortion around the Mn^{3+} and Mn^{4+} for mixed valence manganites etc [116]. For example, it has been shown that the existence of magnetic disorder brings up an Anderson metal-insulator transition with the transition from ferromagnetic to paramagnetic phases [118]. Also, it has been suggested that the strength of coupling between electron and spin can affect the relation between localization and magnetic disorder in the presence of nonmagnetic disorder [119]. For example, in the double exchange limit, which is in the strong coupling limit in which manganites exist, the carrier localization can be enhanced by magnetic disorder and can results in a decrease of T_c or an increase in residual resistance. This story becomes more complicated if we consider manganite system which exhibit phase coexistence such as our LPCMO samples used in this experiment. At least 3 phases, which are paramagnetic insulating (PMI), charge ordered

insulating (COI) and ferromagnetic metallic phases (FMM) are considered to be coexisting in the fluid phase separated region for this sample. It is suggested that this charge ordered insulating phase can be formed (and pinned) around structural disorder [120]. And disorder can stabilize this phase during the phase competition, which occurs during the insulator metal phase transition. This stabilized phase also forms a boundary for the other insulating phase (PMI) and so helps it persist further down to lower temperatures, which can affect T_c , the residual resistivity and the magnetoresistance at low temperature etc [121].

One of the most interesting characteristics of manganites as a strongly correlated electron system is the effect of strain on the system. It was observed that the biaxial (epitaxial) strain, which usually can be found in manganite thin films due to the mismatch between the film and substrate lattice constants, can affect many important characteristics of the system as mentioned in chapter 1.

The mechanism behind this sensitivity is well understood in the scope of the double exchange model, which shows that epitaxial strain leads to the modification of the electron hopping matrix element t of the Mn-O-Mn bond by changing the Mn-O bond length d and the bond angle θ , which are related by equation (6-1) [78] in a way that for tensile strain, (which is the case in which the lattice parameters of the thin film are larger than those of the bulk) results in an increase of the bond length d while the bond angle θ remains approximately the same and for compressive strain the bond angle θ decreases while the bond length remains approximately the same [122]. Epitaxial strain can also enhance the localization of carriers and it can influence the phase separation among coexisting phases by affecting the electron-phonon coupling of the carriers [123].

In the sections below we report this important disorder and strain effect on the manganite system. There are two distinguishing features of this experiment separating it from similar experiments. First, instead of depending on the intrinsic disorder only, we created external disorder by ion bombardment creating defects in the surface of the sample. Second, almost all experiments concerning biaxial strain are referring only to the strain induced by lattice constant mismatch between the film and the substrate. However in this experiment samples are grown in such a way that a minimum amount of substrate induced strain exists and strain is applied externally, by mechanically bending the sample. With this, the pure effect of the strain on the manganite thin film, without the growth mode dependence on the substrate, could be considered. Disorder was applied by bombarding the film with Ar ions without changing the thickness of the film, which can be assured by measuring the room temperature resistance of the sample before and after the procedure to ensure that they are consistent. Applying disorder in this way was done in collaboration with Prof. A. F. Hebard's lab and, this procedure was carried out by Rajiv Misra. Biaxial tensile strain along the a-b plane was applied using a strain probe, which is described in Chapter 2. Three different samples were used for this experiment ((La_{0.6}Pr_{0.4})_{0.67}Ca_{0.33}MnO₃, (La_{0.5}Pr_{0.5})_{0.67}Ca_{0.33}MnO₃ and (La_{0.4}Pr_{0.6})_{0.67}Ca_{0.33}MnO₃). For each sample, the same amount of disorder and strain (5.6×10^{-4}) was applied.

6.2 Disorder and Strain Measurement on LPCMO Thin Films with Three Different Concentration of Pr

Strain was applied at temperatures in which the fluid phase separated state is present, which shows the most sensitivity to applied strain. For the (La_{0.5}Pr_{0.5})_{0.67}Ca_{0.33}MnO₃ sample, strain was applied at 90K, then the temperature was decreased to the lowest temperature range (~10 K) and a RvsT measurement was made by warming the system, the result is marked as

RAAS (right after applying strain), in figure 6-1. Then one more R vs T curve was obtained and is marked as SS (strain settled).

The comparison of RAAS and SS gives the effect of strain on the static phase separated state. During the first R vs. T measurement the system goes through the fluid phase separated state and, the phases reflect the applied strain dynamically. The same kind of explanation can be applied when the strain is released. Considering the result we obtained, it is not necessary to distinguish these two consecutive measurements related to the settling of the strain on the system, for the $(\text{La}_{0.5}\text{Pr}_{0.5})_{0.67}\text{Ca}_{0.33}\text{MnO}_3$ and $(\text{La}_{0.6}\text{Pr}_{0.4})_{0.67}\text{Ca}_{0.33}\text{MnO}_3$ samples, since the change seen is negligible for the static phase separated region. However, for the $(\text{La}_{0.4}\text{Pr}_{0.6})_{0.67}\text{Ca}_{0.33}\text{MnO}_3$ sample, a dramatic difference is seen and should not be ignored and, this is discussed in detail later. For the $(\text{La}_{0.5}\text{Pr}_{0.5})_{0.67}\text{Ca}_{0.33}\text{MnO}_3$ sample two types of measurement, first regular four-probe method with a current source and second a series resistance method with a voltage source, were conducted, as described in Chapter 2. Both of them exhibited the same R vs. T curves except at low temperatures (static phase separated regime) as discussed before, where strong current or static electric field dependence is seen. In that region, the voltage source measurement is not sufficiently accurate to reflect the resistivity upturn at low temperature¹. Therefore the disorder and strain effect for this temperature range is shown in detail (Figure 6-2(b)) with the result of the current sourced measurement.

Figures 6-2 and 6-3 show the comparison of four different conditions for the epitaxially grown 30 nm thickness $(\text{La}_{0.5}\text{Pr}_{0.5})_{0.67}\text{Ca}_{0.33}\text{MnO}_3$ thin films on NGO substrates with current and voltage source measurements respectively which show the exact same tendency other than in the very low temperature region as mentioned before. Therefore the following observations can be

¹ See Chapter 5 about the current effect on the low temperature resistivity upturn.

extracted from either measurement. For both the disordered and nondisordered case, applying strain reduced the T_c for the insulator to metal transition by about 5 K. Both the strained and nonstrained cases are also affected by disorder in the same manner. In addition, the disordered sample shows slightly more precipitate transitions compared to the nondisordered sample. These results are observed both for the warming and cooling curves. This decrease of T_c by the biaxial tensile strain is expected from the reduction of in-plane hopping due to the applied strain [78].

The decrease of T_c under disorder can have several origins such as increased structural disorder enhanced carrier localization resulting in a decreased hopping rate between these localized states and/or possibly the charge ordered phase is enhanced due to this new intruding disorder which causes the insulating phase to persist during the insulator to metal phase transition. Figure 6-2(b) is a detailed view of the current source measurement. It shows a clear increase in the low temperature resistivity upturn for the disordered cases. This suggests the origin of this upturn is related to the carrier localization due to the presence of disorder. T_c reduction induced by applying strain brings enhanced residual resistivity whether the sample is disordered or not.

$(La_{0.6}Pr_{0.4})_{0.67}Ca_{0.33}MnO_3$ thin films on NGO and the result is shown in figure 6-4. After applying strain at 100K, the temperature was decreased to the lowest measuring temperature range (~10K) and an R vs. T measurement was started by warming the system and the result is marked as RAAS in figure 6-4. Then R vs. T was measured once more and is marked as SS. Also after releasing the strain at low temperature (10K) RARS was taken and a second strain released R vs. T measurement was taken and is marked as RSS. As can be seen from figure 6-4 almost no changes are present for any of these cases. This implies that for disordered $(La_{0.6}Pr_{0.4})_{0.67}Ca_{0.33}MnO_3$ films, strain does not have a significant effect. Figure 6-5 shows a comparison of voltage source measurements on epitaxially grown 30 nm thickness

$(\text{La}_{0.6}\text{Pr}_{0.4})_{0.67}\text{Ca}_{0.33}\text{MnO}_3$ films on NGO substrates under 4 different conditions. As we observed previously in figure 6-4, for a disordered sample strain does not change the insulator to metal phase transition temperature T_c while for nondisordered samples it is slightly decreased. Disorder affected the sample in such a way that it became insensitive to applied strain. Compared to the nondisordered $(\text{La}_{0.5}\text{Pr}_{0.5})_{0.67}\text{Ca}_{0.33}\text{MnO}_3$ case the nondisordered $(\text{La}_{0.6}\text{Pr}_{0.4})_{0.67}\text{Ca}_{0.33}\text{MnO}_3$ sample is less affected by the same amount of strain. The reduction of T_c by introducing disorder can still be observed. The figure 6-5 inset shows the low temperature region magnified. Since for this sample we did not measure R vs. T using a small current source, the behavior of the resistivity upturn at low temperature could not be observed (as mentioned before the applied voltage was too high to observe this effect). Another interesting point is that the Pr concentration in a sample is usually considered to be proportional to the structural distortion and ultimately induces disorder in the system. However, if we compare the result of the $(\text{La}_{0.6}\text{Pr}_{0.4})_{0.67}\text{Ca}_{0.33}\text{MnO}_3$ film to the $(\text{La}_{0.5}\text{Pr}_{0.5})_{0.67}\text{Ca}_{0.33}\text{MnO}_3$ film, the disordered $(\text{La}_{0.6}\text{Pr}_{0.4})_{0.67}\text{Ca}_{0.33}\text{MnO}_3$ film has a reduced dependence on strain while the $(\text{La}_{0.5}\text{Pr}_{0.5})_{0.67}\text{Ca}_{0.33}\text{MnO}_3$ film has greater dependence on strain. This contradicting evidence can lead us to the possibility that the intrinsic disorder, which is related to the compound itself, is not exactly the same as the extrinsic disorder, which is applied externally after the sample structure is completed. Magnetization measurements of this sample will be very helpful to clarify this mystery but the technical problem (a strong effect from the paramagnetic substrate) prohibits the observation of very subtle changes in the sample. Our results suggest that the disorder introduced by Pr-substitution sets up the microscopic pattern of phase separation due to long range strain interactions [124]. Once this pattern is set up, the Pr-ions do not play any additional role such as pinning sites for the phase boundaries. The random disorder produced by the Ar-ion

bombardment then acts only as pinning sites for the phase boundaries. Among those 3 LPCMO samples, the $(\text{La}_{0.4}\text{Pr}_{0.6})_{0.67}\text{Ca}_{0.33}\text{MnO}_3$ sample showed the most dramatic changes under strain and disorder. Before conducting the measurements shown in figure 6-6, R vs. T was measured using a lower bias voltage and it showed no insulator to metal phase transition. For the purpose of this experiment, the phase transition is essential, since the applied strain can only be measured at the temperature at which the resistance drops during the phase transition, which is most strain sensitive region. Therefore we increased the bias voltage until the static electric field induced insulator to metal phase transition was observed, which occurred at 70V, the result is marked as NDNS in figure 6-6. After strain was applied at 35K and the sample was cooled down to low temperature, at high temperatures an unexpected low resistance state was found and when it came back to the low temperature region after sweeping at high temperature, the phase transition could no longer be observed and the state remained as an insulating phase (the result is marked as NDS in figure 6-6). This implies that the biaxial tensile strain suppressed the metallic state until no more percolation is possible. After this measurement, the strain was released at low temperature (10K) and R vs. T measurement was begun at that temperature. It started with the same high resistance state as was observed with the strained settled state, and while the system was warmed up it showed a dramatic phase transition to the original phase separated state with a metal to insulator transition. This strongly suggests that the fluid phase separation also exists for the warming period of the system not only for the cooling transition and the effect of strain (or the release of strain) can be settled for this warming procedure. When the system was returned to low temperature again, it showed a low resistance state as expected. Figure 6-7 shows a R vs. T measurement of an $(\text{La}_{0.4}\text{Pr}_{0.6})_{0.67}\text{Ca}_{0.33}\text{MnO}_3$ film in which disorder has been applied starting

with a high resistance state the same as in the case in which strain was applied for the non-disordered sample.

As discussed before, while the system passes through the warming fluid phase separated temperature region, it experiences a phase transition and when it came back to low temperature after sweeping the high temperature region, it recovers the low resistance state as it does in the non-disordered case (the result is marked as DNS in figure 6-7). The second measurement shows that this low resistance state is reproducible and stable even after repeatedly going through the phase transition. For this disordered settled system (marked as DNS2 in figure 6-8), we applied strain at 35K and cooled down from that temperature and started a R vs. T measurement and the result is shown in figure 6-8 and is marked as DS. As seen in the graph, when it came back to the low temperature region, it showed the high resistivity state, which is a result of the effect of strain settlement concomitant with the system undergoing fluid phase separation. From these results it is clear that if strain is released the system will return to their original state while in the fluid phase separated state (during warming) and when it is brought to low temperature again it will recover its low resistance state. However the result is a little bit puzzling. The system did not go back to the low resistance state while it was warmed and it recovered its low resistance state while it was cooling. The result is shown in figure 6-9, DS 2 indicates the measurement for the strain settled system and DNSR indicates the measurement starting right after the strain was released at 10K and the temperature was swept. DNSR2 indicates the measurement after releasing the strain and allowing the system to settle, in which the original low resistance state is recovered. Due to the fluctuation of T_c with the temperature sweeping rate, the absolute change of T_c could not be compared between the disordered and non-disordered sample.

Figures 6-10 to 6-12 show the measured resistance while strain was applied for each sample and the sample conditions are indicated. Time corresponds to the number of rotations of the worm gear, which can be converted into the amount of is applied strain applied to the system. Sometimes (Figure 6-11(a), Figure 6-12(a) and (b)), the strain was applied discontinuously with pauses between rotating the worm gear. Furthermore after strain was applied there was a time delay, which differs from case to case, for the settling of the strain through the film (for example in figure 6-10(b), we finished applying strain at 400 sec but it settled at 500sec). In every case the strain was applied the same in a way by first determining the point at which the screw makes contact with the sample and then applying same amount of rotation of the worm gear.

6.3 Discussion

We studied the external disorder and biaxial extrinsic tensile strain effect on three compositions of LPCMO thin films on NGO substrates.

For the $(La_{0.5}Pr_{0.5})_{0.67}Ca_{0.33}MnO_3$ sample, both the effect of disorder and strain reduced T_c of the insulator to metal phase transition. The suppressing of the ferromagnetic metallic phase may originate from the reduction of in-plane hopping due to the applied strain. The disorder effect can be explained by a decrease in the hopping rate between localized states due to the increasing structural disorder enhanced carrier localization and also for this kind of phase separated material we can not ignore the possibility of a persisting insulating phase during the insulator to metal phase transition by the enhanced charge ordered phase due to the introduction of increased disorder by ion bombardment. The resistivity upturn in the low temperature region is enhanced with applied disorder, which means this upturn is related to the carrier localization induced by disorder. For the $(La_{0.6}Pr_{0.4})_{0.67}Ca_{0.33}MnO_3$ sample, the reduction of T_c by the effect of disorder can be observed for both the strained and nonstrained case. However, for the disordered $(La_{0.6}Pr_{0.4})_{0.67}Ca_{0.33}MnO_3$ sample, the effect of strain was negligible, while for the non-disordered

sample strain had the effect of reducing T_c . This contradicts the fact that the $(La_{0.5}Pr_{0.5})_{0.67}Ca_{0.33}MnO_3$ sample, which can be considered a more disordered system than the $(La_{0.6}Pr_{0.4})_{0.67}Ca_{0.33}MnO_3$ sample, shows a clear effect under strain. Also, it is observed that for both the $(La_{0.5}Pr_{0.5})_{0.67}Ca_{0.33}MnO_3$ and $(La_{0.6}Pr_{0.4})_{0.67}Ca_{0.33}MnO_3$ samples, reduction of T_c due to the effect of strain resulted in an increase of the residual resistivity. For both samples, a reduction of T_c due to the effect of disorder resulted in a decrease of the minimum resistivity, which is not usually expected. From this, we could infer that the external disorder we applied to this system is not acting in the same way as the intrinsic film disorder, which here is the intrinsic structural disorder caused by increasing the Pr concentration. However, we expect that if we decreased the temperature further down, an increase of the residual resistivity would be observed due to the enhancement of the curvature of the upturn for both disordered samples as is usually expected. The $(La_{0.4}Pr_{0.6})_{0.67}Ca_{0.33}MnO_3$ sample showed most sensitive changes under strain and disorder. By applying strain we could eliminate the insulator to metal phase transition and by releasing the strain we could recover the phase transition for both the disordered and non-disordered cases. Also, by observing how the strained sample settled in the $(La_{0.4}Pr_{0.6})_{0.67}Ca_{0.33}MnO_3$ system, we suggest that the fluid phase separated state can exist during the phase transition of the warming run and not only during the cooling run.

To sum up our ideas for this disorder and strain experiment, we review two dominant models for the origin of phase separation in perovskite manganites, which are a long range strain induced phase coexistence scenario [124] and enhanced nucleation of the insulating phase under the presence of disorder [125]. The strain induced phase coexistence model is based on the dynamics of the movable boundary between domains of different phases with similar free energies but different crystal structures. In the latter model, the insulating phase, (which was not

preferred in our system due to the substrate-induced strain [51]) is trapped by disorder causing static phases separation. Therefore, with our experimental result, we could observe a dynamic response (movement of phase boundaries) of the phase separation to the external applied strain in the fluid phase separated (FPS) state. This result suggests that the FPS state is formed due to long-range strain interactions. On the other hand, an enhancement of static phase separation was observed when external disorder was introduced i.e. the phase boundaries were pinned by the extrinsic disorder. Both experiments were done under the effect of ionic size disorder (Pr-substitution), which was necessary to balance the free energies of FMM and COI phase. Our results suggest that at least in thin films, ionic size disorder does not play a significant role in pinning the phase boundaries in the FPS state since the strain effect increases for larger Pr-concentrations. The insensitivity of the phase boundaries to the ionic size disorder is most likely due to the substrate-induced strain. However, below ~ 50 K the ionic size disorder leads to a static phase separated (glassy) state [51]. Our results have shed new light on the mechanism leading to the formation of the micrometer scale phase separated state in manganites. In addition, these results will be significant in understanding the behavior of other materials, which undergo solid-solid structural transitions such as ferroelectrics.

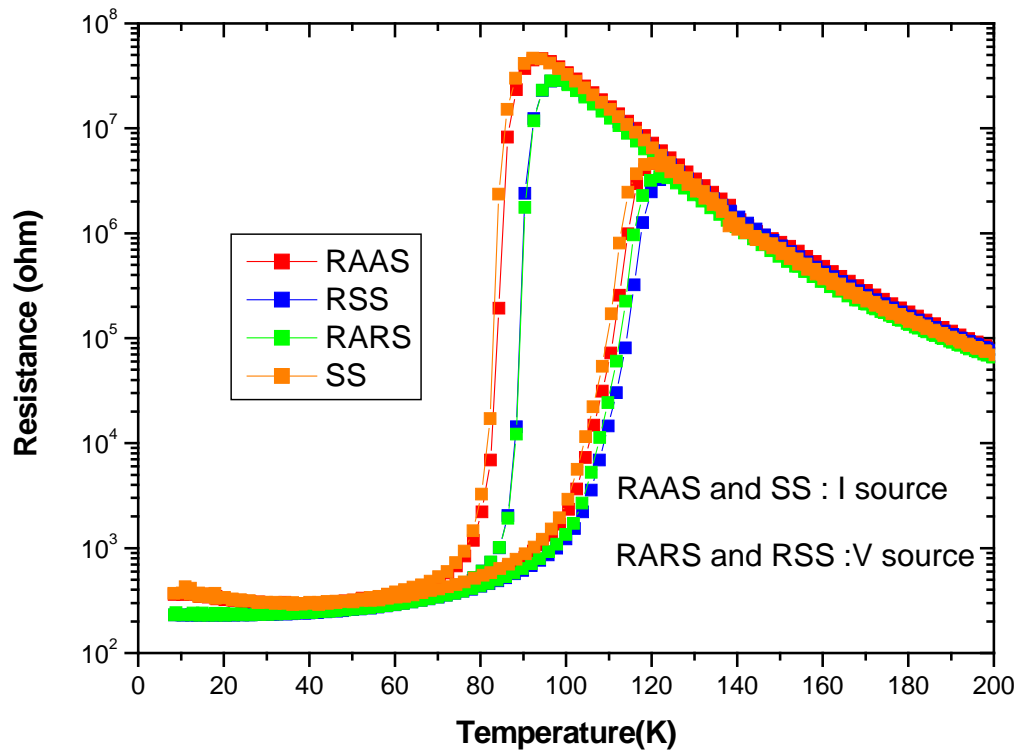
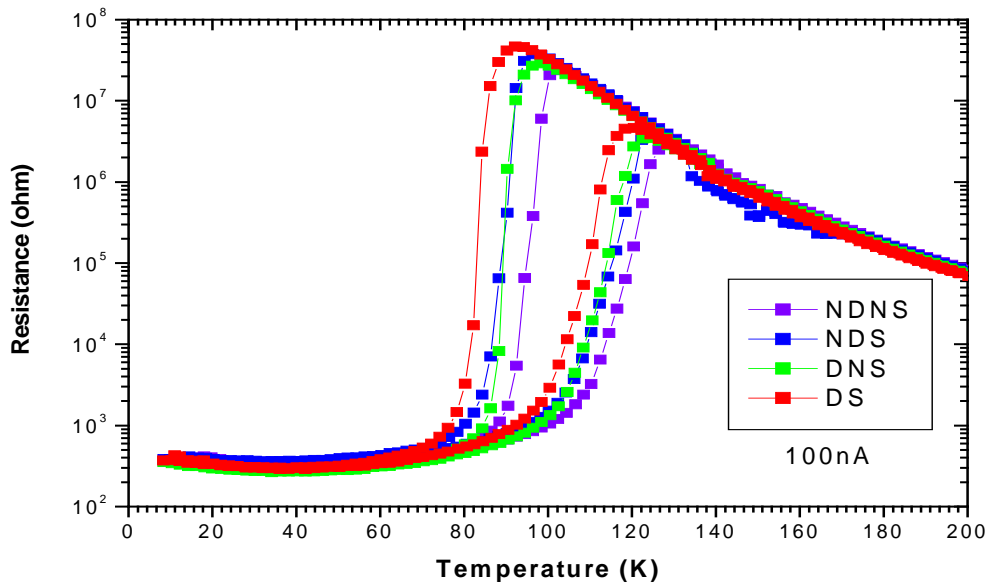
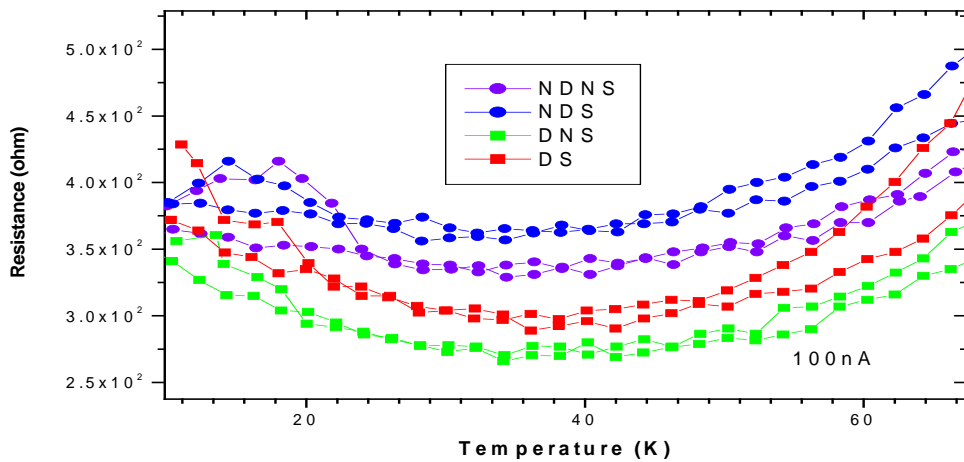


Figure 6-1: Comparison of the resistance for the cases in which the measurement is taken right after applying strain (RAAS), after the strain has settled (SS), right after releasing the strain (RARS) and after the strain releasing has settled (RSS) for disordered $(La_{0.5}Pr_{0.5})_{0.67}Ca_{0.33}MnO_3$ thin films on NGO



(a)



(b)

Figure 6-2: Resistance obtained from a current source measurement (100nA) for the $(\text{La}_{0.5}\text{Pr}_{0.5})_{0.67}\text{Ca}_{0.33}\text{MnO}_3$ thin films on NGO. (a) Comparison of the Nondisordered and Nonstrained case (NDNS), Nondisordered and strained case (NDS), Disordered and Nonstrained case (DNS) and Disordered and strained (DS) case. (b) Low temperature details for each case.

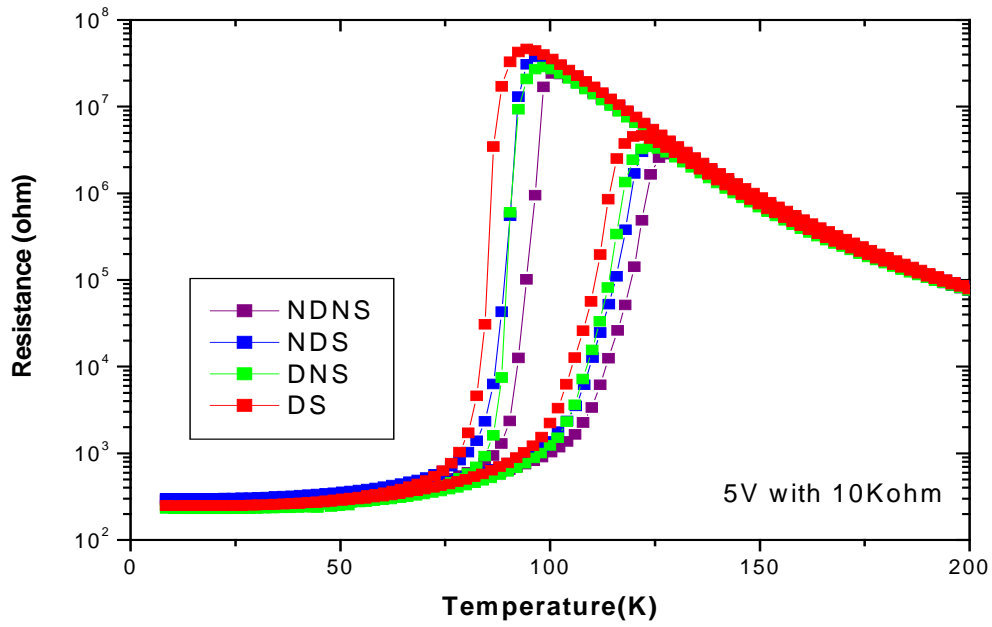


Figure 6-3: Resistance obtained by a voltage source measurement for $(\text{La}_{0.5}\text{Pr}_{0.5})_{0.67}\text{Ca}_{0.33}\text{MnO}_3$ thin films on NGO. Comparison between Nondisordered and Nonstrained case (NDNS), Nondisordered and strained case (NDS), Disordered and Nonstrained case (DNS) and Disordered and strained (DS) case.

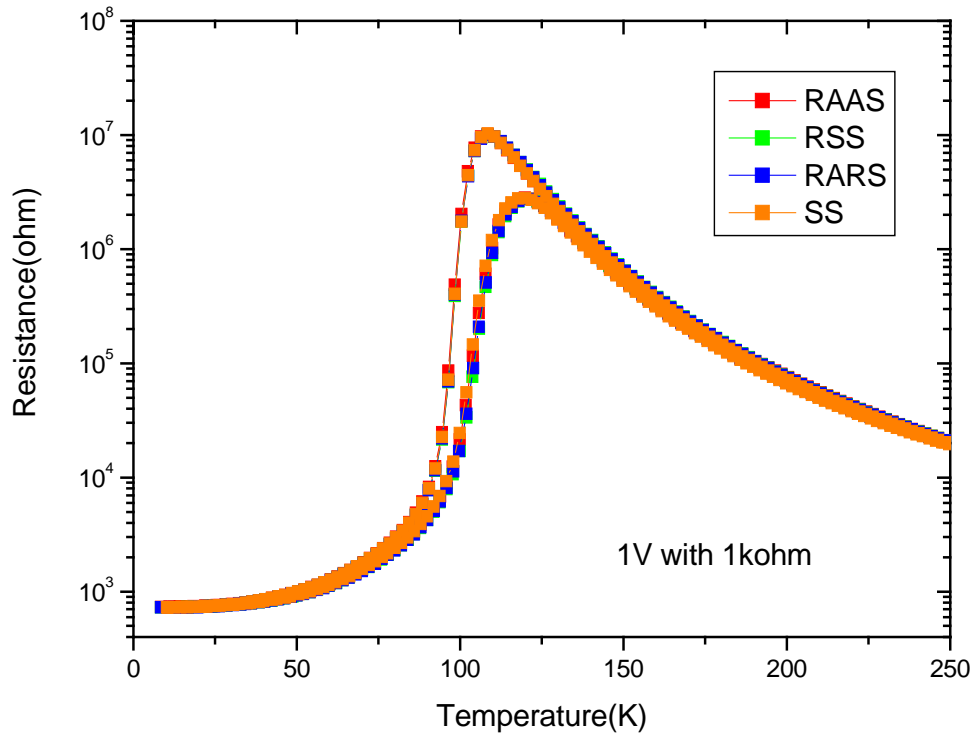


Figure 6-4: Comparison of R vs. T right after applying strain (RAAS), after the strain has settled (SS), right after releasing the strain (RARS) and after releasing the strain and settling (RSS) for the disordered $(La_{0.6}Pr_{0.4})_{0.67}Ca_{0.33}MnO_3$ thin films on NGO.

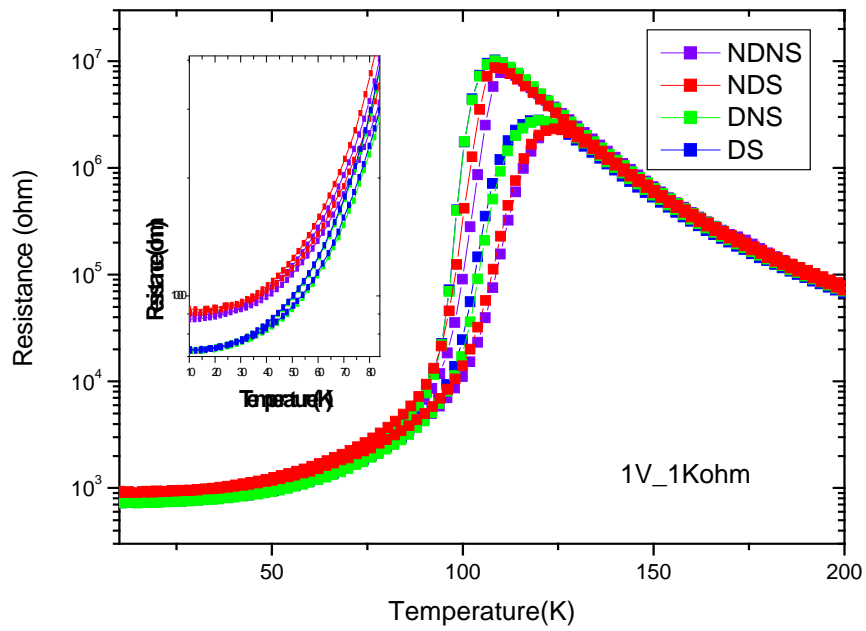


Figure 6-5: Resistance obtained by a voltage source measurement for the $(\text{La}_{0.6}\text{Pr}_{0.4})_{0.67}\text{Ca}_{0.33}\text{MnO}_3$ 30nm films on NGO. Comparison between the Nondisordered and Nonstrained case (NDNS), the Nondisordered and strained case (NDS), the Disordered and Nonstrained case (DNS) and the Disordered and strained (DS) case. Inset shows a detailed view of the low temperature range.

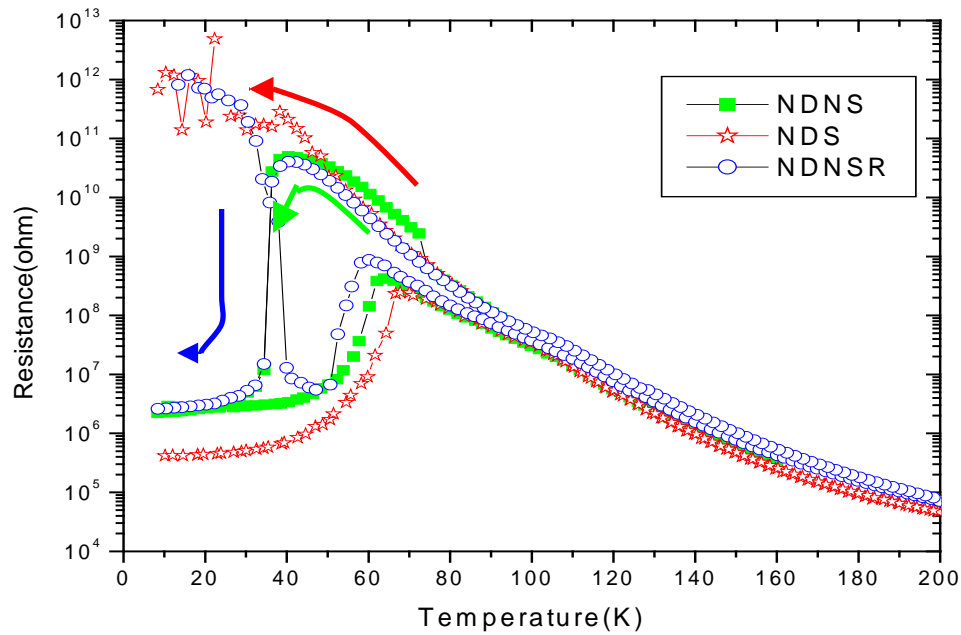


Figure 6-6: Resistance as a function of temperature obtained by voltage source measurement for the 30 nm $(\text{La}_{0.4}\text{Pr}_{0.6})_{0.67}\text{Ca}_{0.33}\text{MnO}_3$ film on NGO. Comparison between the Nondisordered and Nonstrained case (NDNS), Nondisordered and strained case (NDS), Nondisordered and nonstrained obtained after releasing the strain (NDNSR). Arrows indicate cooling run for each curves.

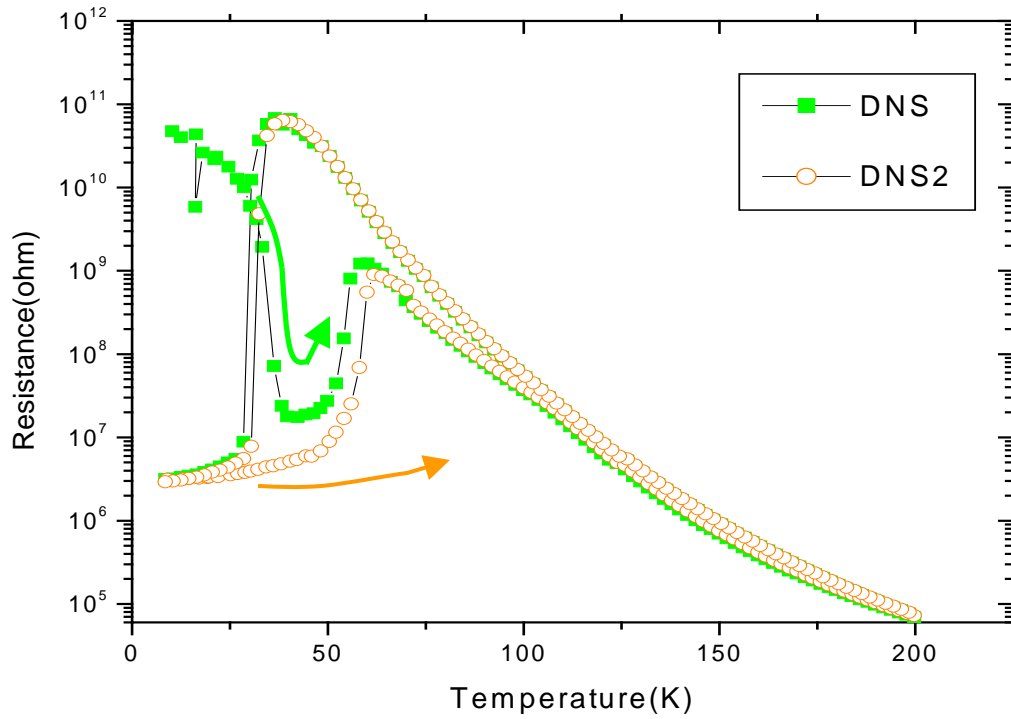


Figure 6-7: Resistance obtained by voltage source measurement for the $(La_{0.4}Pr_{0.6})_{0.67}Ca_{0.33}MnO_3$ thin films on NGO. Comparison between the Disordered and Nonstrained case in the first measurement (DNS) and the Disordered and Nonstrained case in the second measurement (DNS2). Arrows indicate warming run for each curve.

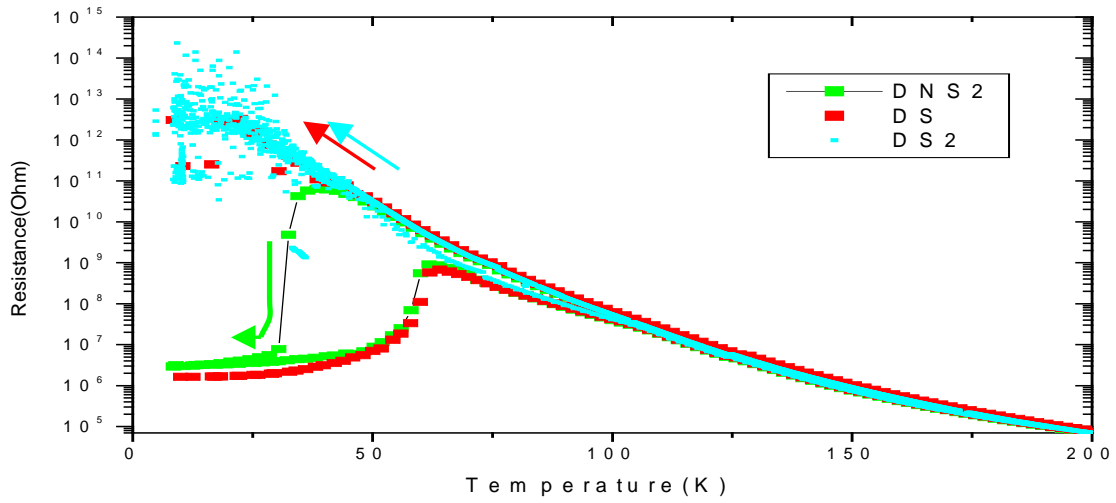


Figure 6-8: Resistance obtained by voltage source measurement for $(La_{0.4}Pr_{0.6})_{0.67}Ca_{0.33}MnO_3$ thin films on NGO. Comparison between Disordered and Nonstrained samples in the second measurement (DNS2 same as figure 6-7). Disordered strained samples in the first measurement (DS) and Disordered and strained samples in the second measurement (DS2-Disordered and strain stabilized). Arrows indicate cooling run for each curve.

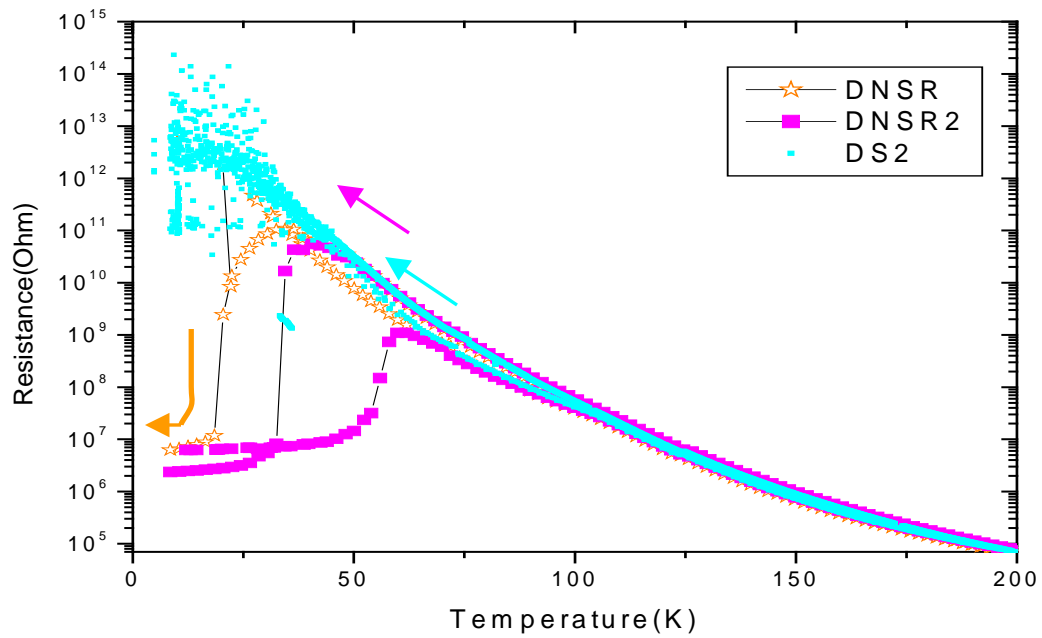
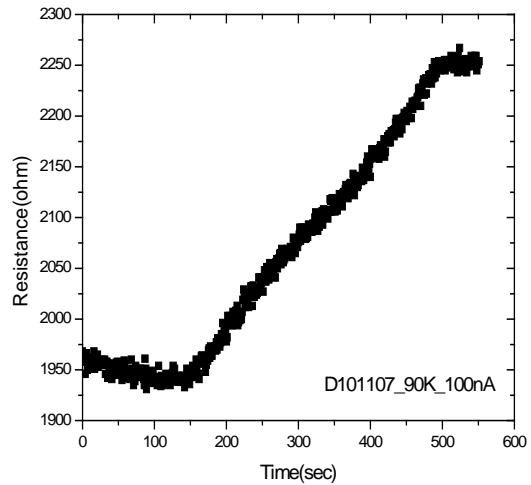
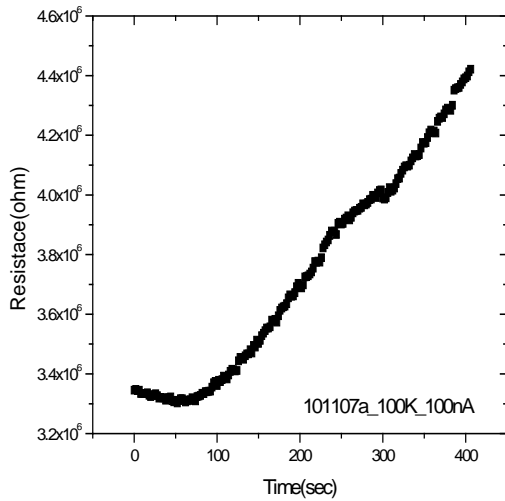


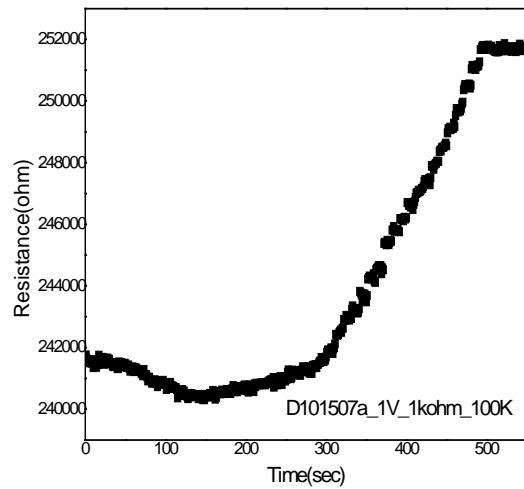
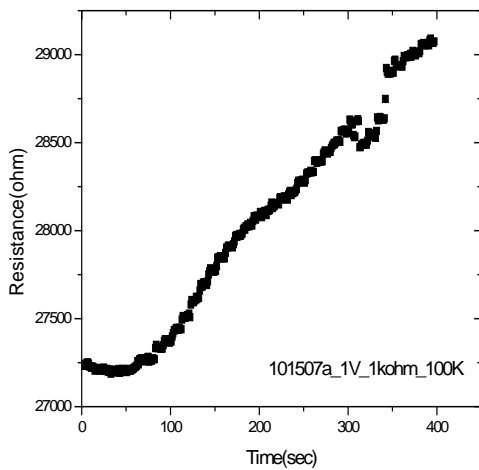
Figure 6-9: Resistance obtained by voltage source measurement for $(La_{0.4}Pr_{0.6})_{0.67}Ca_{0.33}MnO_3$ thin films on NGO. Comparison between the first measurement of the Disordered and strain stabilized case (DS2), the Disordered and Nonstrained case obtained after releasing the strain and the second measurement of the Disordered and Nonstrained case after releasing the strain (DNSR2). Arrows indicate cooling run for each curve.



A

B

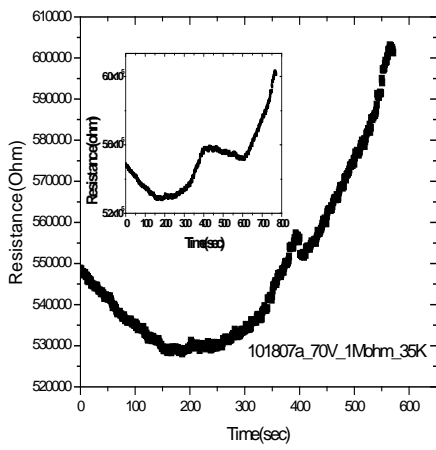
Figure 6-10: R vs. time graph while applying strain to the $(\text{La}_{0.5}\text{Pr}_{0.5})_{0.67}\text{Ca}_{0.33}\text{MnO}_3$ thin films on NGO. (a) Strain was applied to the nondisordered thin film. (b) Strain was applied to the disordered thin film.



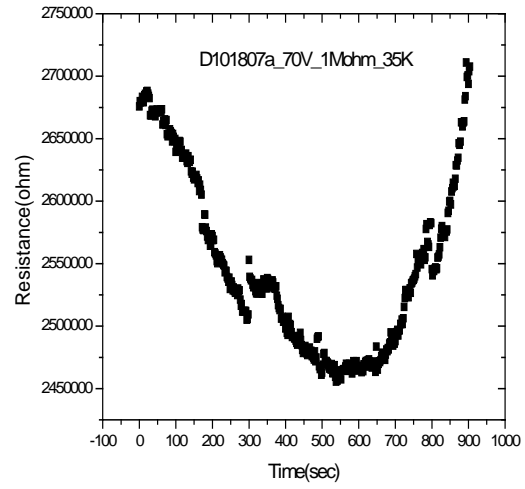
A

B

Figure 6-11: R vs. time graph while applying strain to the $(\text{La}_{0.6}\text{Pr}_{0.4})_{0.67}\text{Ca}_{0.33}\text{MnO}_3$ thin films on NGO. (a) Strain was applied to the nondisordered thin film. (b) Strain was applied to the disordered thin film.



A



B

Figure 6-12: R vs. time graph while applying strain to the $(\text{La}_{0.4}\text{Pr}_{0.6})_{0.67}\text{Ca}_{0.33}\text{MnO}_3$ thin films on NGO. (a) Strain was applied to the nondisordered thin film. (b) Strain was applied to the disordered thin film.

CHAPTER 7 SUMMARY

Electron-doped cuprates have low upper critical field values $H_{c2} \sim 10\text{T}$ at 1.5 K and hence it is possible to study their normal state at low temperatures. Such studies have been done before and evidence of a "pseudogap" was seen. However, to understand the origin of this pseudogap and which model of high- T_c superconductivity it supports, it is necessary to study the effect of high magnetic fields on this pseudogap. In this dissertation, the normal state gap of single crystal samples of the electron-doped cuprate PCCO was studied using a point contact spectroscopy apparatus made in house. The result from this experiment suggests that preformed pairing above T_c may not be the origin of the pseudogap. Furthermore, the origin of this normal state gap, which is observed in high fields in this experiment is not the pseudogap found in hole-doped cuprates and it may be due to the electron-electron interaction at the surface of this electron doped high T_c superconducting material.

The other type of transition metal oxide, which was studied during the course of this dissertation work, was phase-separated manganites. Several new features of these materials were observed including a giant positive magnetoresistance, which was observed in ultra thin films of the holed doped multi phase manganite $(\text{La}_{0.5}\text{Pr}_{0.5})_{0.67}\text{Ca}_{0.33}\text{MnO}_3$. Unlike the fabricated magnetic tunnel junction devices, this magnetoresistance (MR) effect has its maximum value close to the insulator to metal transition temperature and reduces with decreasing temperature. To find out the mechanism leading to this positive MR, the effect of three orientations of the magnetic field on the $(\text{La}_{0.5}\text{Pr}_{0.5})_{0.67}\text{Ca}_{0.33}\text{MnO}_3$ thin films were studied: 1) perpendicular to the plane of the film, 2) parallel to the plane of the film and applied current, 3) parallel to the plane of the film but perpendicular to the applied current. All directions showed distinctive positive magnetoresistance behavior. The effect of the field orientation suggests that spin dependent

scattering between misaligned magnetic domains induced by changes in the direction of the sweeping field is the origin of this LFMR. The possibility that this positive MR is related to the tunneling magnetoresistance due to the spin conservation of the tunneling process across the insulating regions separating the ferromagnetic metallic regions was also suggested. The voltage dependence of the MR and the fact that the field value for this PMR is close to the coercive field, measured in another film of the same composition, support this mechanism. It is possible that this LFMR is due to the spin glass like behavior in manganites at low temperatures.

Characteristics of these phase separated manganite thin films under the application of an electric field in the perpendicular direction were also studied. For this experiment partially etched 26.5nm $(\text{La}_{0.4}\text{Pr}_{0.6})_{0.67}\text{Ca}_{0.33}\text{MnO}_3$ films on top of 60nm $\text{La}_{0.67}\text{Ca}_{0.33}\text{MnO}_3$ (LCMO) films on an insulating substrate NdGaO_3 (NGO) substrates using pulsed laser deposition (PLD) were prepared. The LCMO film is metallic below 250 K and is used as the bottom electrode to apply the voltage perpendicular to the plane of the $(\text{La}_{0.4}\text{Pr}_{0.6})_{0.67}\text{Ca}_{0.33}\text{MnO}_3$ film and gold contacts acted as the other electrodes. From measurements of the DC transport properties, the nonlinear conductance due to the phase separated nature of $(\text{La}_{0.4}\text{Pr}_{0.6})_{0.67}\text{Ca}_{0.33}\text{MnO}_3$ was observed and their origin due to magnetic phase separation is further suggested by the removal of this nonlinearity by applying a magnetic field and a reduced critical current (or static electric field). In comparison with transport measurements in the parallel direction, the insulator to metal transition in the out-of-plane direction in the temperature region of fluid phase separation was observed. The complex impedance was also measured to study the dielectric properties of $(\text{La}_{0.4}\text{Pr}_{0.6})_{0.67}\text{Ca}_{0.33}\text{MnO}_3$.

Finally, the extrinsic disorder and biaxial external tensile strain effect on the three different compositions of LPCMO thin films on NGO substrates was studied. For all of those samples,

extrinsic disorder reduced the insulator to metal transition temperature. It was suggested that increasing the structural disorder induced a decrease in the hopping rate between localized states, which are already present in the material due to the intrinsic disorder and/or the persisting insulating phase during the insulator to metal phase transition resulting from an enhancement of the charge ordered phase, which can happen in materials with coexisting phases. However the discrepancies which exist between films in which disorder has been introduced intrinsically, by growing films with a composition $(\text{La}_{0.5}\text{Pr}_{0.5})_{0.67}\text{Ca}_{0.33}\text{MnO}_3$ instead of the less disordered $(\text{La}_{0.6}\text{Pr}_{0.4})_{0.67}\text{Ca}_{0.33}\text{MnO}_3$ films, and films in which disorder has been introduced extrinsically, by ion bombardment of $(\text{La}_{0.6}\text{Pr}_{0.4})_{0.67}\text{Ca}_{0.33}\text{MnO}_3$, shows that the effect of externally applied disorder is distinct from the effect of intrinsic disorder. Other than the $(\text{La}_{0.6}\text{Pr}_{0.4})_{0.67}\text{Ca}_{0.33}\text{MnO}_3$ samples in which disorder was applied externally, all samples showed a reduction of the insulator-to metal temperature (or the transition could not be observed) under the effect of strain. The origin of this mechanism was explained by a reduction of the in-plane hopping due to the applied tensile strain. The $(\text{La}_{0.4}\text{Pr}_{0.6})_{0.67}\text{Ca}_{0.33}\text{MnO}_3$ sample, which is the most intrinsically disordered compound among the three samples, due to the highest Pr concentration, showed the most sensitivity to changes in strain and disorder. The metallic phase could be completely suppressed down to the lowest measured temperatures by applying strain and we could also remove the insulator to metal phase transition for this sample by the application of external disorder. An enhanced resistivity upturn in the low temperature region for samples with externally applied disorder was observed using low current measurements. This indicates that this upturn is related to the carrier localization induced by disorder. Strain settlement experiments for $(\text{La}_{0.4}\text{Pr}_{0.6})_{0.67}\text{Ca}_{0.33}\text{MnO}_3$ suggests that the metal-insulator phase transition observed on warming runs is similar to the fluid phase separated state as observed in the cooling

run. This experiment suggests that in thin films, ionic size (intrinsic) disorder does not play a significant role in pinning the phase boundaries in the FPS state due to the substrate-induced strain. However, below the insulator to metal transition temperature, a glass like static phase separated state will be induced by this ionic size disorder [51]. Hence, our results shows that the FPS state is formed due to long range strain interactions while the static phase separated state is formed due to the pinning of phase boundaries by quenched (intrinsic and extrinsic) disorder.

LIST OF REFERENCES

1. P. Fournier, P. Mohanty, E. Maiser, S. Darzens, T. Venkatesan, C. J. Lobb, G. Czjzek, R. A. Webb, and R. L. Greene, *Phys. Rev. Lett.* **81**, 4720 (1998)
2. G. S. Boebinger, Yoichi Ando, A. Passner, T. Kimura, M. Okuya, J. Shimoyama, K. Kishio, K. Tamasaku, N. Ichikawa, and S. Uchida, *Phys. Rev. Lett.* **77**, 5417 (1996)
3. L. Alff, Y. Krockenberger, B. Welter, M. Schonecke, R. Gross, D. Manske, and M. Naito, *Nature (London)* **422**, 698 (2003)
4. P. Anderson, *Science* **235**, 196 (1987)
5. G. Kotliar and Liu J, *Phys. Rev. B* **38**, 5142 (1988)
6. N. Nagaosa and P. A. Lee, *Phys. Rev. B* **45**, 966 (1992)
7. A. Kampf and J. R. Schrieffer: *Phys. Rev. B* **41**, 6399 (1990)
8. T. Dahm and L. Tewordt, *Phys. Rev. B* **52**, 1297 (1995)
9. D. Pines, *Z. Phys. B* **103**, 129 (1997)
10. A. V. Chubukov, D. Pines and B. P. Stojkovi'c, *J. Phys. Condens Matter* **8**, 10017 (1996)
11. V. J. Emery, S. A. Kivelson and O. Zachar, *Phys. Rev. B* **56**, 6120 (1997)
12. A. Leggett, in *Modern Trends in the Theory of Condensed Matter*, edited by A. Bekalsky and J. Przyspawa, Springer, Berlin, p.13 (1980)
13. P. Nozières and S. Schmitt-Rink, *J. Low Temp. Phys.* **59**, 195 (1985)
14. Q. Chen, J. Stajic, A. Tan and K. Levin cond-mat/0404274 (2004)
15. R. Laughlin, cond-mat/0209269 (2002)
16. Y. Yanase and K. Yamada, *Journal of the Physical Society of Japan* Vol. **68**, 2999 (1999)
17. V. J. Emery and S. A. Kivelson, *Nature (London)* **374**, 434 (1995)
18. V. J. Emery and S. A. Kivelson, *Phys. Rev. Lett.* **74**, 3253 (1995)
19. S. Sachdev, *Science* **288**, 475 (2000)
20. G. Deutscher, *Rev. Mod. Phys.* **77**, 109 (2005)
21. C. Castellani, C. di Castro and M. Grilli, *Z. Phys. B, Condens. Matter* **103**, 137 (1997)

22. A. Perali, C. Castellani, C. di Castro, M. Grilli, E. Piegari and A.A. Varlamov, Phys. Rev. B **62**, R9295 (2000)
23. A. J. Millis and H. Monien, Phys. Rev. Lett. **70** 2810 (1993)
24. B. L. Altshuler, L. B. Ioffe and A. J. Millis, Phys. Rev. B **53**, 415(1996)
25. K. Gorny, Phys. Rev. Lett. **82**, 177 (1997)
26. T. Timusk and B. Statt, Rep. Prog. Phys. **62**, 61 (1999)
27. V. M. Krasnov, Phys. Rev. B **86**, 2657 (2001)
28. Y. Kao, Phys. Rev. B **64**, 140505 (R)
29. H. K. Nguyen and S. Chakravarty, Phys. Rev. B **65**, 180519R (2002)
30. P. Pieri, Phys. Rev. Lett. **89**, 127003 (2002)
31. N. P. Armitage, D. H. Lu, C. Kim, A. Damascelli, K.M. Shen, F. Ronning, D. L. Feng, P. Bogdanov, Z.-X. Shen, Y. Onose, Y. Taguchi, Y. Tokura, P. K. Mang, N. Kaneko, and M. Greven, Phys. Rev. Lett. **87**, 147003 (2001)
32. B. Kyung, V. Hankevych, A.-M. Daré, and A.-M. S. Tremblay, Phys. Rev. Lett. **93**, 147004 (2004)
33. T. Kawakami, T. Shibauchi, Y. Terao, M. Suzuki, and L. Krusin-Elbaum, Phys. Rev. Lett. **95**, 017001 (2005)
34. S. Kleefisch, B. Welter, A. Marx, L. Alff, R. Gross, and M. Naito, Phys. Rev. B **63**, 100507 (2001)
35. A. Biswas, P. Fournier, V. N. Smolyaninova, R. C. Budhani, J. S. Higgins, and R. L. Greene, Phys. Rev. B **64**, 104519 (2001)
36. M. M. Qazilbash, A. Biswas, Y. Dagan, R. A. Ott and R. L. Greene, Phys. Rev. B **68**, 024502 (2003)
37. K. Tanaka, W. S. Lee, D. H. Lu, A. Fujimori, T. Fujii, Risdiana, I. Terasaki, D. J. Scalapino, T. P. Devereaux, Z. Hussain, Z. -X. Shen, Science **314**, 1910 (2006)
38. Y. Dagan, M. M. Qazilbash, and R. L. Greene, Phys. Rev. Lett. **94**, 187003 (2005)
39. H. Srikanth and A. K. Raychaudhuri, Phys. Rev. B **46**, 14713 (1992)
40. A. Biswas, P. Fournier, M. M. Qazilbash, V. N. Smolyaninova, Hamza Balci, and R. L. Greene, Phys. Rev. Lett. **88**, 207004 (2002)
41. G. E. Blonder, M. Tinkham, and T. M. Klapwijk, Phys. Rev. B **25**, 4515 (1982)

42. S.Chakravarty, R. B. Laughlin, D. K. Morr , C. Nayak, cond-mat/0005443 (2000)
43. K. Miyano, T. Tanaka, Y. Tomioka and Y. Tokura, Phys. Rev. Lett. **78**, 4257 (1997)
44. V. Kiryukhin, D. Casa, J. P. Hill, B. Keimer, A. Vigliante, Y. Tomioka and Y. Tokura, Nature **386**, 813 (1997)
45. R.M. Kusters, D. A. Singleton, D. A. Keen, R. McGreevy and W. Hayes, Physica B **155**, 362 (1989)
46. K. Chabara, T. Ohno, M. Kasai and Y. Kozono, Appl. Phys. Lett. **63**, 1990 (1993)
47. R. von Helmolt, J. Wocker, B. Holzapfel, M. Schultz and K. Samwer, Phys. Rev. Lett. **71**, 2331 (1993)
48. S. Jin, T. H. Tiefel, M. McCormack, R. A. Fastnacht, R. Ramesh and L. H. Chen, Science **264**, 413 (1994)
49. Y. Tokura, A. Urushibara, Y. Moritomo, T. Arima, A. Asamitsu, G. Kido and N. Furukawa, J. Phys. Soc. Japan **63**, 3931(1994)
50. A. Asamitsu, Y. Tomioka, H. Kuwahar and Y. Tokura, Nature **388**, 50 (1997)
51. T. Dhakal, J. Tosado, and A. Biswas, Phys. Rev. B **75**, 92404 (2007)
52. A. Asamitsu, Y. Moritomo, Y. Tomioka, T. Arima and Y. Tokura, Nature **373**, 407 (1995)
53. C. Zener, Phys. Rev. **82**, 403 (1951)
54. P. W. Anderson and H. Hasegawa, Phys. Rev. **100**, 67 (1955)
55. P-G. De Gennes, Phys. Rev. **118**, 141 (1960)
56. E. Dagotto, Science **309**, 257 (2005)
57. J. Burgy et al., Phys. Rev. Lett. **87**, 277202 (2001)
58. J. Burgy, A. Moreo, E. Dagotto, Phys. Rev. Lett. **92**, 097202 (2004)
59. S. Yunoki et al., Phys. Rev. Lett. **80**, 845 (1998)
60. S. Satpathy Zoran, S. Popovic' and Filip R. Vukajlovic , J. Appl. Phys. **79**, 4555 (1996)
61. H. Y. Hwang, S-W. Cheong, P. G. Radaelli, M. Marezio, and B. Batlogg, Phys. Rev. Lett. **75**, 914 (1995)
62. Y. Tokura, *Colossal Magnetoresistive Oxides*, Gordon and Breach Science Publishers, Singapore (2000)

63. A. J. Millis, P. B. Littlewood, and B. I. Shraiman, *Phys. Rev. Lett.* **74**, 5144 (1995)
64. D. Louca, T. Egami, E. L. Brosha, H. Röder, and A. R. Bishop, *Phys. Rev. B* **56**, R8475 (1997)
65. S. Mori, C. H. Chen, and S-W. Cheong, *Nature (London)* **392**, 473 (1998)
66. Y. Tomioka, A. Asamitsu, H. Kuwahara, Y. Moritomo, and Y. Tokura, *Phys. Rev. B* **53**, R1689 (1996)
67. S. Mori, C. H. Chen, and S-W. Cheong, *Phys. Rev. Lett.* **81**, 3972 (1998)
68. S. Zhou, J. Xu, S. Li, W. Yang, J. Zou, G. Zhao, H. Li, Y. Hang, J. R. Cheng and Y. Zhang, *Phys. Stat. Sol. (a)*, **201**, No. 5, 990 (2004)
69. M. Lide, R. Martinez and J. P. Attfield, *Phys. Rev. B* **54**, R15622 (1996)
70. S. Mercone, C. A. Perroni, V. Cataudella, C. Adamo, M. Angeloni, C. Aruta, I G. De Filippis, F. Miletto, A. Oropallo, P. Perna, A. Yu. Petrov, U. Scotti di Uccio, and L. Maritato, *Phys. Rev. B* **71**, 064415 (2005)
71. Motome and N. Furukawa, *Phys. Rev. B* **71**, 014446 (2005)
72. S. Jin, T.H. Tiefel, M. McCormack, H.M. O'Bryan, L.H. Chen, R. Ramesh, and D. Schurig, *Appl. Phys. Lett.* **67**, 557 (1995)
73. W. Prellier, A. Biswas, M. Rajeswari, T. Venkatesan, and R.L. Greene, *Appl. Phys. Lett.* **75**, 397 (1999)
74. F.S. Razavi, G. Gross, H.-U. Habermeier, O. Lebedev, S. Amelinckx, G. Van Tendeloo, and A. Vigliante, *Appl. Phys. Lett.* **76**, 155 (2000)
75. C. Kwon, M.C. Robson, K.-C. Kim, J.Y. Gu, S.E. Lofland, S.M. Bhogat, Z. Trajanovic, M. Rajeswari, T. Venkatesan, A.R. Kratz, R.D. Gomez, and R. Ramesh, *J. Magn. Magn. Mater.* **172**, 229 (1997)
76. T. Walter, K. Dorr, K.-H. Muller, D. Eckert, K. Nenkov, M. Hecker, M. Lehmann, and L. Schultz, *J. Magn. Magn. Mater.* **222**, 175 (2000)
77. W. Prellier, M. Rajeswari, T. Venkatesan, and R.L. Greene, *Appl. Phys. Lett.* **75**, 1446 (1999)
78. C. A. Perroni, V. Cataudella, G. De Filippis, G. Iadonisi, V. Marigliano Ramaglia, and F. Ventriglia, *Phys. Rev. B* **68**, 224424 (2003)
79. J. Klein, J.B. Philipp, G. Carbone, A. Vigliante, L. Alff, and R. Gross, *Phys. Rev. B* **66**, 052414 (2002)

80. American Magnetics Inc., Job 10764 manual for 9Tesla Superconducting Magnet system, American Magnetics Inc. (2003)
81. S. T. Hannahs, LabVIEW 1.0, NHMFL program (2002)
82. S. H. Yun, A. Biswas, B. Liang and R.L. Greene, NHMFL report **13**, 14 (2006)
83. Ch. Renner, B. Revaz, J.-Y. Genoud, K. Kadowaki, and \hat{A} . Fischer, Phys. Rev. Lett. **80**, 149 (1998)
84. Y. Wang, Lu Li, and N. P. Ong, Phys. Rev. B **73**, 024510 (2006)
85. Y. Onose, Y. Taguchi, K. Ishizaka, and Y. Tokura, Phys. Rev. Lett. **87**, 217001 (2001)
86. T. Kawakami, T. Shibauchi, Y. Terao, and M. Suzuki, Phys. Rev. B **74**, 144520 (2006)
87. K. K. Gomes, A. N. Pasupathy, A. Pushp, S. Ono, Y. Ando, and A. Yazdani, Nature (London) **447**, 569 (2007)
88. S. H. Pan, E. W. Hudson, K. M. Lang, H. Eisaki, S. Uchida and J. C. Davis, Nature **403**, 746 (2000)
89. P. W. Anderson and N. P. Ong, cond-mat/0405518 (2004)
90. L. Shan, Y. Huang, H. Gao, Y. Wang, S. L. Li, P. C. Dai, F. Zhou, J. W. Xiong, W. X. Ti, and H. H. Wen, Phys. Rev. B **72**, 144506 (2005)
91. Y. Imry and Z. Ovadyahu, Phys. Rev. Lett. **49**, 841 (1982)
92. \hat{A} . Fischer, M. Kugler, I. Maggio-Aprile, C. Berthod, and C. Renner, Rev. Mod. Phys. **79**, 353 (2007)
93. J. W. Loram, J. L. Tallon, and W. Y. Liang, Phys. Rev. B **69**, 060502 (2004)
94. A.K. Raychaudhuri, K.P. Rajeev, H. Srikanth, and N. Gayathri, Phys. Rev. B **51**, 7421 (1995)
95. M. Viret, M. Drouet, J. Nassar, J. P. Contour, C. Fermon and A. Fert, Europhys. Lett. **39**, 545 (1997)
96. N. D. Mathur, G. Burnell, S. P. Isaac, T. J. Jackson, B.-S. Teo, J. L. MacManus-Driscoll, L. F. Cohen, J. E. Evetts and M. G. Blamire, Nature (London) **388**, 266 (1997)
97. X.W.Li, A. Gupta, X. Gang and G. O. Gong, Appl. Phys. Lett. **71**, 1124 (1997)
98. H. -Yi. Zhai, J. X. Ma, D. T. Gillaspie, X. G. Zhang, T. Z. Ward, E. W. Plummer, and J. Shen, Phys. Rev. Lett. **97**, 167201 (2006)

99. Z. Lu, Y. Zhou, Y. Du, R. Moate, D. Wilton, G. Pan, Y. Chen and Z. Cui, *Appl. Phys. Lett.* **88**, 142507 (2006)
100. B. Vertruyen, L. Dusoulier, J.-F. Fagnard, Ph. Vanderbemden, G. Vanhoyland, M. Ausloos, J. Delwiche, A. Rulmont and R. Cloots, *J. Magn. Magn. Mater.* **280**, 264 (2004)
101. M. Ziese and S.P. Sena, *J. Phys.: Condens. Matter* **10**, 2727 (1998)
102. J.-E. Wegrowe, A. Comment, Y. Jaccard, J.-Ph. Ansermet, N. M. Dempsey, and J.-P. Nozières, *Phys. Rev. B* **61**, 12216 (2000)
103. Th. G. Rijks, R. Coehoorn, M. J. de Jong, and W. J. de Jonge, *Phys. Rev. B* **51**, 283 (1995)
104. C. M. Varma, *Phys. Rev. Lett.* **83**, 3538 (1999)
105. K.-I. Kobayashi, T. Kimura, Y. Tomioka, H. Sawada, K. Terakura and Y. Tokura, *Phys. Rev. B* **59**, 11159 (1999)
106. J. M. De Teresa, M. R. Ibarra, J. García, J. Blasco, C. Ritter, P. A. Algarabel, C. Marquina and A. del Moral, *Phys. Rev. Lett.* **76**, 3392 (1996)
107. J.C. Nie, J.H. Wang and B.R. Zhao. *J. Magn. Magn. Mater.* **192**, 379 (1999)
108. L.Ghivelder and F.Parisi *Phys. Rev. B* **71**, 184425 (2005)
109. D. I. Golosov, *Phys. Rev. B* **67**, 064404 (2003)
110. J. Stankiewicz, J. Sesé, J. García, J. Blasco, and C. Rillo, *Phys. Rev. B* **61**, 11236 (2000)
111. A. Guha, A. K. Raychaudhuri, A. R. Raju, and C. N. R. Rao, *Phys. Rev. B* **62**, 5320 (2000)
112. A. Guha, N. Khare, A. Raychaudhuri, and C. N. R. Rao, *Phys. Rev. B* **62**, R11941 (2000)
113. L. Zhang, C. Israel, A. Biswas, R. L. Greene, and A. de Lozanne, *Science* **298**, 805 (2002)
114. K. S. Cole and R. H. Cole, *J. Chem. Phys.* **9**, 341(1941)
115. M. Jaime, H. T. Hardner, M. B. Salamon, M. Rubinstein, P. Dorsey, and E. Emin, *Phys. Rev. Lett.* **78**, 951 (1997)
116. Y. Lyanda-Geller, S. H. Chun, M. B. Salamon, P. M. Goldbart, P. D. Han, Y. Tomioka, A. Asamitsu and Y. Tokura, *cond-mat/ 0012462* (2000)
117. C. M. Varma, *Phys. Rev. B* **54**, 7328 (1996)
118. L. Sheng, D. Y. Xing, D. N. Sheng, and C. S. Ting, *Phys. Rev. B* **56**, R7053 (1997)

119. S. Kumar and P. Majumdar, Europhys. Lett. **13**, 561 (1990)
120. S. Cox, J. Singleton, R. D. McDonald, A. Migliori and P. B. Littlewood, Nature Materials **7**, 25 (2007).
121. V. Podzorov, B. G. Kim, V. Kiryukhin, M. E. Gershenson, and S-W. Cheong, Phys. Rev. B **64**, 140406 (2001)
122. Q. Yuan, cond-mat/0112480 (2001)
123. A.J. Millis, T. Darling, and A. Migliori, J. Appl. Phys. **83**, 1588 (1998)
124. K. H. Ahn, T. Lookman and A. R. Bishop, Nature **428**, 401 (2004)
125. A. Moreo, S. Yunoki, Elbio Dagotto Science **283**, 2034 (1999)
126. R. P. Rairigh, G. Singh-Bhalla, S. Tongay, T. Dhakal, A. Biswas & A. F. Hebard, Nature Physics **3**, 551 (2007)
127. G. Singh-Bhalla, S. Selcuk, T. Dhakal, A. Biswas, A. F. Hebard, cond-mat/arXiv:0707.4411v1 (2007)
128. B. L. Al'tshuler and A. G. Aronov, JETP Lett. **37**, 175 (1983)

BIOGRAPHICAL SKETCH

I was born in SunCheon city in the southern part of Korea to parents Yun, Tae Sun and Chun, Soon Ja and stayed there until I finished my high school. When I was a young girl, one of my hobbies was watching night sky, which engraved on me the meaning of infinity with the image of incredible darkness in between shining stars, much before I learned the symbol ∞ in my math class. It puzzled me and made me enjoy my ironical existence between real world and really understandable world. At the same time, I was encouraged to be one of those: a philosopher, a psychologist or a scientist by my father who is the big fan of Immanuel Kant and G.W.F. Hegel. After I spent my young days in SunCheon, I moved to capital Seoul to do my undergraduate study in Yonsei University, the first university founded in Korea by American missionary Mr. Underwood. With a lot of agony as a young scientist, I ended up with more questions than when I started the undergraduate program in physics. After I got my bachelor's degree, I kept my academic interest in physics and proceeded to study in graduate school at the same university. I studied quantum field theory focusing on the vortex solution of the Maxwell-Chern- Simons gauge theory with the support of the Brain Korea 21 project. In the year 2002, I started my PhD in physics at the University of Florida with an Alumni fellowship. Since I joined the Biswas Group in 2004, I have studied transition metal oxides, electron-doped high T_c superconductor (HTSC) and manganites up to today. I designed a probe for the Point Contact Spectroscopy (PCS) and have made samples of manganites including nano-structured multi-layered one. The observation of the existence of normal state gap at the 31T for the electron doped HTSC $\text{Pr}_{1-x}\text{Ce}_x\text{CuO}_4$ leads me to the open possibility for the new interpretation about the normal state gap found in surface property related measurement. The study of characteristics of manganites such as giant positive magnetoresistance and abnormal disorder and strain effect was achieved and open new ways of research with the methods used for those experiment. I am

married to Aaron Gray since 2005 and keeping that state happily up to this moment and now I am studying Cooper pair with my baby due in April.